Advances in Understanding Subduction Zone Processes

Jennifer Shannon Gorce

Dissertation submitted to the faculty of Virginia Tech in partial fulfillment of the requirements for the degree of

Doctor of Philosophy

In

Geosciences

Mark J. Caddick
Ethan F. Baxter
Richard D. Law
Robert J. Bodnar

May 3rd, 2018
Blacksburg, VA

Keywords: Metamorphism, subduction, thermodynamics, geochronology, fluids, blueschist, eclogite

Advances in Understanding Subduction Zone Processes

Jennifer Shannon Gorce

ABSTRACT

Subduction zones are an important 'recycling center' at which material from the exterior of the Earth is transported to Earth's interior. The processes that occur along subduction zones have important implications for elemental cycles, geodynamics, and material mass transport. The cold, dense subducting lithosphere experiences prograde metamorphism as it transitions from blueschist to eclogite facies resulting in the breakdown of volatile-bearing minerals and producing anhydrous minerals and a free fluid phase. Previous works attempting to understand the evolution of subducted lithologies have provided a firm foundation in which to apply field work, computational thermodynamic modeling, and geochronological techniques in order to better constraint the Pressure-Temperature-time (*P-T-t*) paths and dehydration of subducted lithologies.

This dissertation; 1.) Explores novel approaches to modeling and predicting fluid/rock interactions during deep (>60km) subduction, and 2.) Questions what the calculated *P-T-t* path from eclogite lithologies reveals about early exhumation of subducted terrains. The second chapter focuses on how externally-derived hydrous fluids can decarbonate subducted basalt, liberate carbon and transfer it to the overlying mantle wedge, where it can be incorporated into melt that forms volcanic arcs. Here, the thermodynamic response to the infiltration of external fluids assuming open system, pervasive fluid flow, is quantified. It was determined that while hotter subduction zones have more favorable *P-T* conditions in which to facilitate decarbonation than colder subduction, the extent of decarbonation is largely dependent on the availability of fluid from the dehydration of underlying serpentine. The third chapter constrains the *P-T-t* paths of subducted lithologies from Syros, Greece using a combination of thermodynamic modeling, $^{147}Sm/^{144}Nd$ garnet geochronology, and quartz-in-garnet geobarometry. This provides insight into early exhumation of subducted lithologies, and allows for the exploration of assumptions made in thermodynamic modeling and in quartz-in-garnet geobarometry. Results suggest that garnet grew over a 4.31my period from 45.71±0.98Ma to 41.4±1.7Ma, during initial exhumation from maximum subducted depths. Calculated exhumation rates are a relatively rapid, 0.4–1.7 cm/yr. Because field relationships on Syros suggest the width of the subduction channel along the slab/mantle interface is not adequate to facilitate buoyancy-driven ascension of metabasic blocks, initiation of southward retreat of the Hellenic Subduction Zone and subsequent slab rollback is proposed to have played an important role in the exhumation of subducted lithologies. The final chapter investigates the compositional controls on the *P-T* conditions at which dehydration due to the breakdown of hydrous minerals occur during subduction (blueschist/eclogite boundary), and the implications they have on the rheology, seismicity, and densification of the down going slab. Total Alkali Silica (TAS) diagrams reveal that eclogites are more alkali rich, implying that initial alteration of the seafloor controls the mineral evolution of subducted basalt in many cases.

Advances in Understanding Subduction Zone Processes

Jennifer Shannon Gorce

GENERAL AUDIENCE ABSTRACT

Subduction zones are an important ‘recycling center’ at which material from the exterior of the Earth is transported to Earth’s interior. The processes that occur along subduction zones have important implications for elemental cycles, geodynamics, and material mass transport. The cold, dense rock that gets heated and deeply buried (high pressure metamorphism) releases fluid as water-bearing minerals breakdown. Previous works attempting to understand the history of subducted rocks have provided a firm foundation in which to apply field work, modeling, and dating techniques in order to better constraint the depths and temperatures a rock experienced, and over what time interval metamorphism and subsequent fluid loss occurred.

This dissertation; 1.) Explores novel approaches in modeling and predicting fluid/rock interactions during deep (>60km) subduction, and 2.) Asks what does the calculated Pressure-Temperature-time (*P-T-t*) path from eclogite lithologies reveal about early exhumation of subducted terrains. The second chapter focuses how water-rich fluids can infiltrate a subducted rock and liberate carbon, which migrates upwards and can be incorporated into melt that forms volcanic arcs. It was determined that while the potential to release more carbon is higher in hotter subduction zones, the extent of decarbonation is largely dependent on the availability of fluid from the dehydration of the water bearing mineral., serpentine. The third chapter constrains the *P-T-t* paths of subducted lithologies from Syros, Greece using a combination of techniques, which not only provides insight into the return of subducted rocks back to the surface, but allows for the exploration of assumptions made in various analytical methodologies. Results suggest that garnet grew over a span from 45.71±0.98Ma to 41.4±1.7Ma, as the rock moved at a rate of 0.4–1.7 cm/yr to travel approximately 18km back to the surface, which suggests that a large-scale tectonic mechanism is needed to facilitate the rock’s return journey. The final chapter investigates the compositional controls on the *P-T* conditions in which the breakdown of hydrous minerals, and subsequent fluid loss, occur during subduction (blueschist/eclogite boundary), and the implication they have on the physical properties and behavior of the subducting rock. Chemical data reveal that subducted rocks that dehydrate earlier are more enrich in K and Na, implying that initial alteration of the seafloor controls the mineral evolution of subducted basalt.

DEDICATION

This dissertation is dedicated to my family, whose natural curiosity and quirkiness taught me to reach beyond the stars, and whose steadfast support has given me the courage to hang out there for a while.

ACKNOWLEDGEMENTS

This work would not be possible if it were not for the support, generosity and kindness of the incredible people that I have had the pleasure and privilege of knowing throughout the course of my doctorate. I apologize for anyone I neglect to mention. First and foremost, I would like to thank my advisor Mark J. Caddick, for not only serving as an advisor, but as an intellectual guide, mentor, and as a pillar of stability and reason on the days when I felt overwhelmed. Thank you for giving me the knowledge, skills, and the passion that has molded me into a geoscientist of which I can feel proud. I would also like to thank Besim Dragovic, whose mentorship has been fundamental to completion of this dissertation. Besim, thank you for teaching me the ways of Sm/Nd garnet geochronology, for always having your door open, a willingness to talk about subduction zones and Doctor Who, and for always offering an open and sympathetic ear.

I thank my other committee members, Ethan F. Baxter, Bob J. Bodnar, and Rick D. Law for your insights and guidance over the years. In particular, Ethan thank you for your time and dedication to a fantastic field experience on Syros, Greece, and for providing fulfilling research experiences over the summer months at Boston College's Geochronology and TIMS facilities. A special thanks to John Schumacher as well, for his guidance in the field. Rick Law and Bob Bodnar also deserve recognition for not only playing a role in my doctoral studies, but also serving as teachers and mentors to my undergraduate self. Rick's structural geology course and Bob's senior seminar course provided me with a solid foundation of critical thinking and science communication skills that have proven to be invaluable in graduate school and will continue to guide me in my geoscience journey.

I thank the Metamorphic Process research group at Virginia Tech, both past and present members, in no particular order: Kirkland Broadwell, Victor Guevera, Kristie Dorfler, Allie Nagurney, Calvin Mako, Lisa Whalen, Hanna Brooks, Kristen McCall, Emma Tulsky, Bob Tracy, Matt Petroff, Esther Schwarzenbach, Christiana Hoff, and TJ Kenny. Many of you served and continue to serve as mentors to me, while others are peers, and to a few, I have had the privilege of considering you my mentees. All have provided me with stimulating intellectual conversation, insightful observations regarding my work, and constructive criticism. You have inspired me to stay curious, always ask why, and persevere in the face of academic adversity. Without you, I would not be the caliber of scientist that I am, and I consider you all to be part of my 'geo-family'.

Last, I would like to thank my other friends in geosciences, Adam Angel, Kannikha Kolandaivelu, Sara Ulrich, Ty Whalen, Aly Hoeher, Yury Klyukin, Rui Serra Maia, Jamie Kendall, Evan Ramos, and Mike Tappa, who have given me scientific perspective and fond memories. I would also like to thank the wonder friends that I have made in the Blacksburg community. Some of you have miraculously stuck with me for eight years, and have stood beside me through some strange, fantastic, and awesome adventures.

ATTRIBUTIONS

Chapter 2, "Thermodynamic constraints on carbonate breakdown and carbon volatile emission during subduction," will be submitted to *Earth and Planetary Science Letters* for publication. JS Gorce was responsible for computational modeling, summarizing and interpreting data from the literature, and drafting all figures and writing the manuscript. MJ Caddick assisted in developing the multistage, thermodynamic modeling methodology, interpreting results, structuring text, and clarifying figures. RJ Bodnar provided stimulus and guidance for calcite solubility calculations.

Chapter 3, "Insights into early exhumation of the Cycladic Blueschist Unit using thermodynamic modeling, inclusion barometry, and $^{147}Sm/^{144}Nd$ geochronology," will be submitted to *Earth and Planetary Science Letters* for publication. JS Gorce was responsible for final thermobarometric calculations, acquiring geochronology and inclusion barometry data, drafting all figures and writing the manuscript. B Dragovic, M Tappa, EB Baxter and J Kendall provided guidance, knowledge, and insight into the process of $^{147}Sm/^{144}Nd$ garnet geochronology. B Dragovic also contributed significantly to the interpretation of multiple data sets, including geochronology, inclusion-host barometry, and petrography. MJ Caddick was responsible for assisting in thermobarometric calculations, petrographic and tectonic interpretation as well as helped clarify the text structure and figures. RJ Bodnar assisted with Raman spectroscopy analyses used in host-inclusion geobarometry. A special thanks to John Schumacher for his guidance during field work.

Chapter 4, "Compositional effects on the *P-T* conditions of the blueschist/eclogite boundary," may be submitted to *Chemical Geology* for publication. JS Gorce was responsible for summarizing and interpreting data from the literature, thermodynamic calculations, drafting all figures and writing the manuscript. B Dragovic provided intellectual guidance, discussion, and interpretation of results. MJ Caddick assisted in discussion and interpretation.

Table of Contents

List of Figures

List of Tables

Chapter 1: Introduction

1.1. Introduction

Subduction zones are important because the process of subducting cold, dense, oceanic lithosphere into the hot, dry, ultramafic mantle drives important geologic processes such as elemental recycling of H_2O and CO_2, partly controls the behavior and rheology of the Earth's interior, and leads to metamorphic mineral reactions. Many of these processes have important implications for societal hazards, such as the evolution of volcanic island arcs and deep earthquake seismicity. Thus, there is a great need to understand the fundamental processes occurring along these convergent margins, which has spurred tremendous advances in subduction zone studies in the past 20 years, as summarized by Bebout, (2018).

One of the most well studied High Pressure/Low Temperature (HP-LT) subduction terranes is the Cycladic Blueschist Unit (CBU), which is spectacularly well preserved on the island of Syros, Greece. It is the type locality for glaucophane (Hausmann, 1845), the Na-amphibole responsible for giving blueschists their color, and has served as a natural laboratory for subduction zone studies for decades. Parts of Syros are interpreted to preserve the interface of the slab/mantle interface (Bonneau et al., 1984; Dixon and Ridley, 1987; Trotet et al., 2001; Breeding et al., 2004) because metabasites that have reached blueschist and eclogite facies conditions are juxtaposed and sitting in a matrix of serpentine in the field (Dixon, 1976; Lister and Raouzaios, 1996; Trotet et al., 2001b; Keiter et al., 2004; Schumacher et al., 2008; Ring et al., 2010; Phillippon et al., 2013).

Metamorphic studies on Syros began when workers in the mid 1970's and 1980 used well preserved deformational fabrics (e.g. Ridley, 1982; Ridley, 1984) to construct the tectonic evolution of the CBU on Syros. In the past couple of decades, the volume and breadth of studies conducted on Syros has exploded to include complex studies in geochronology, geothermobarometry, geochemistry, and structural geology. For example, workers have integrated deformation fabrics in white mica generations found in CBU lithologies and Ar/Ar geochronology studies to understand the timing and mechanisms of deformation and exhumation of high pressure lithologies (Mal.,uski et. al., 1987; Forster and Lister, 2004; Pulzer et al., 2005; Brocker et. al., 2013; Lister and Forster, 2016). Other geochronometers such as U-Pb in zircon (Broecker and Enders, 1999; Tomaschek et al., 2003; and Lu-Hf in garnet (Lagos et. al., 2007) complement metamorphic *P-T* constraints (e. g. Trotet et. al., 2001) because they allow us to constrain the rates of tectonic processes. Furthermore, additional studies that focus on the nature of fluids in

subduction, such as their generation, movement, and composition (Marschall et. al., 2006; Ague, 2007; Miller et. al., 2009; Marschall et. al., 2009; Ague and Nicolescu, 2014; Kleine, 2014), have contributed immensely to our understanding of metasomatic processes, elemental recycling, and dehydration of the down going slab.

The metamorphic, geochemical, and deformational evidence preserved in the rock record of the CBU on Syros, Greece has provided metamorphic petrologists with valuable insights into phenomena such as slab metamorphism, volatile release, mantle wedge dynamics, metasomatism, and exhumation of high pressure terrains. The chapters in this work seek to build upon this knowledge by examining subduction zones through the lens of metamorphic petrology by integrating field work, computational thermodynamic modeling and geochronological techniques to understand 1.) Exhumation of high pressure terrains, 2.) The cycling of fluid during subduction, 3.) Compositional influences on the dehydration and subsequent densification of subducting oceanic.

In Chapter 2, *Thermodynamic constraints on carbonate breakdown and carbon volatile emission during subduction* we investigate the generation of volatile C from subducting slabs due to the addition of H_2O-rich fluids that drive dissolution of carbonate rich lithologies. We use thermodynamic modeling to explore the feasibility decarbonation by questioning 1.) At subarc conditions, how capable are externally-derived H_2O-rich fluids of driving dissolution of carbonate minerals within the altered basaltic cap of the subducting lithosphere? 2.) Does the breakdown of serpentine at subarc conditions yield the hydrous fluids required for this interaction with carbonate-bearing lithologies? To answer these questions, we calculate equilibrium mineral assemblages and fluid compositions (assuming a simple H_2O–CO_2 binary) for typical lithologies experiencing a range of subduction zone geotherms, exploring the addition of fluids at various stages. We conclude that while hotter subduction systems have *P-T* conditions that are more favorable to the dissolution of carbonate, the availability of external fluid pays an important role in balancing the global carbon budget and the depth of deserpentinization reactions strongly controls the availability of fluids for slab decarbonation.

In Chapter 3, *Insights into early exhumation of the Cycladic Blueschist Unit using thermodynamic modeling, inclusion barometry, and $^{147}Sm/^{144}Nd$ geochronology* we use garnet-bearing lithologies from Syros to constrain the *P-T-t* history of subducted lithologies and explore the assumptions made in thermodynamic modeling and inclusion-host geobarometry. Our results

from thermodynamic modeling and Sm/Nd geochronology suggest that garnet grew during initial exhumation of the CBU and exhumation rates calculated from these data imply that the CBU was exhumed relatively quickly (0.4-1.7 cm/yr). Because field relationships on Syros suggest the width of the subduction channel is not adequate to facilitate buoyancy-driven ascension of metabasic and metagabbroic blocks we propose that the initiation of southward retreat of the Hellenic Subduction Zone and subsequent slab rollback plays an important role in the exhumation of subducted lithologies. We also compare the results of quartz-in-garnet geobarometry with thermodynamic modeling and find that quartz-in-garnet geobarometry predicts isobaric garnet growth, while thermodynamic modeling predicts that garnet grew during exhumation. We propose that the proximity of neighboring inclusions, especially in the core of garnet, results in an underestimate of entrapment pressure. Taking equations from Zhang (1998) we calculate the magnitude of this underestimation and apply a correction to inclusion pressures based on their proximity to other inclusions. The application of this correction results in entrapment pressure estimates that agreed with thermodynamic modeling.

In Chapter 4, *Compositional effects on the P-T conditions of the blueschist/eclogite boundary*, we investigate how bulk rock composition acts as an important control on the *P-T* conditions of the blueschist/eclogite transition. We examine the chemical differences in blueschist and eclogite lithologies found on Syros, Greece, because eclogite and blueschist can be found juxtaposed to each other, implying that they experienced the same *P-T* conditions and thus composition is the more important control on whether lithologies record blueschist metamorphism and some lithologies record eclogite metamorphism. Total Alkali Silica (TAS) diagrams reveal that there is a systematic chemical difference between blueschist and eclogites on Syros, Greece; eclogites have higher alkali contents with respect to their silica contents in comparison to blueschists. While this is still a work in progress, we tentatively suggest that chemical heterogeneities acquired during initial seafloor alteration of the basaltic protolith play an important role in the absolute *P-T* conditions of the blueschist eclogite boundary.

1.2. References

Ague, J., J., 2007, 'Models of permeability contrasts in subduction zone mélange: Implications for gradients in fluid fluxes, Syros and Tinos Islands, Greece', Chemical Geology, v. 239, i. 3, p. 217-227, doi: 10.1016/j.chemgeo.2006.08.012

Ague, J., and Nicolescu, S., 2014, Carbon dioxide released from subduction zones by fluid-mediated reactions: Nature Geoscience, v. 7, no. 5, p. 355–360, doi: 10.1038/ngeo2143.

Bebout, G. E., 2018, Twenty years of subduction zone science: Subduction top to bottom 2 (ST2B-2); GSA Today, v. 28, p. 4-10, doi: 10.1130/GSATG354A.1.

Bonneau, M., 1984, Correlation of the Hellenide nappes in the south-east Aegean and their tectonic reconstruction: Geological Society, London, Special Publications, v. 17, no. 1, p. 517–527, doi: 10.1144/GSL.SP.1984.017.01.38.

Breeding, C., Ague, J., and Bröcker, M., 2004, Fluid–metasedimentary rock interactions in subduction-zone mélange: Implications for the chemical composition of arc magmas: Geology, v. 32, no. 12, p. 1041–1044, doi: 10.1130/G20877.1.

Bröcker, M., Baldwin, S., and Arkudas, R., 2013, The geological significance of40Ar/39Ar and Rb-Sr white mica ages from Syros and Sifnos, Greece: a record of continuous (re)crystallization during exhumation?: Journal of Metamorphic Geology, v. 31, no. 6, p. 629646, doi: 10.1111/jmg.12037.

Broecker, M., and Enders, M., 1999, U–Pb zircon geochronology of unusual eclogite-facies rocks from Syros and Tinos (Cyclades, Greece), Geology Magazine, v. 136, i. 2, p. 111-118, doi

Dixon, J. E., Feenstra, A, Jansen, J., Kreulen, R, Ridley, J, Salemink, J, and Schuiling, RD, 1987, Excursion Guide to the Field Trip on Seriphos, Syros, and Naxos: , Chemical Transport in Metasomatic Processes, p. 467–518.

Dixon, J. E., Ridley, J. R., 1987. Syros. In Chemical transport in metasomatic processes (ed. H. C. Helgeson), pp. 489–501. Dordrecht: Reidel.

Forster, M. A., Lister, G. S., 2004, The interpretation of 40Ar/39Ar apparent age spectra produced by mixing: application of the method of asymptotes and limits. Journal of Structural Geology v. 26, i. 2, p. 287–305

Hausmann J. F. L., 184, Beiträge zur Oryktographie von Syra, Journal für Praktische Chemie, p. 238–241

Keiter, M., Piepjohn, K., Ballhaus, C., Lagos, M., and Bode, M., 2004, Structural development of high-pressure metamorphic rocks on Syros island (Cyclades, Greece): Journal of Structural Geology, v. 26, no. 8, p. 14331445, doi: 10.1016/j.jsg.2003.11.027.Kleine, 2014

Lagos, M., Scherer, E. E., Tomaschek, F., Münker, C., Keiter, M., Berndt, J., and Ballhaus, C., 2007, High precision Lu–Hf geochronology of Eocene eclogite-facies rocks from Syros, Cyclades, Greece, Chem. Geol., 243(1–2), 16–35, doi:10.1016/j.chemgeo.2007.04.008.

Lister, G., and Forster, M., 2016, White mica 40Ar/39Ar age spectra and the timing of multiple episodes of high-pressure metamorphic mineral growth in the Cycladic eclogite-blueschist belt,

Syros, Aegean Sea, Greece: Journal of Metamorphic Geology, v. 34, no. 5, p. 401-421, doi: 10.1111/jmg.12178.

Lister, G. S., and Raouzaios, A., 1996, The tectonic significance of a porphyroblastic blueschist facies overprint during Alpine orogenesis: Sifnos, Aegean Sea, Greece: Journal of Structural Geology, v. 18, no. 12, p. 1417-1435, doi: 10.1016/S0191-8141(96)00072-7

Maluski, H., Bonneau, M., and Kienast, J. R., 1987, Dating the metamorphic events in the Cycladic area; 39 Ar/40 Ar data from metamorphic rocks of the Island of Syros (Greece): Bulletin de la Société géologique de France, v. 3, no. 5, p. 833-842, doi: 10.2113/gssgfbull.III.5.833.

Marschall, H., Ludwig, T., Altherr, R., Kalt, A., and Tonarini, S., 2006, Syros Metasomatic Tourmaline: Evidence for Very High-δ11B Fluids in Subduction Zones: Journal of Petrology, v. 47, no. 10, p. 1915–1942, doi: 10.1093/petrology/egl031.

Marschall, H., Altherr, R., Gméling, K., and Kasztovszky, Z., 2009, Lithium, boron and chlorine as tracers for metasomatism in high-pressure metamorphic rocks: a case study from Syros (Greece): Mineralogy and Petrology, v. 95, no. 3-4, p. 291–302, doi: 10.1007/s00710-008-0032-3.

Miller, D., Marschall, H., and Schumacher, J., 2009, Metasomatic formation and petrology of blueschist-facies hybrid rocks from Syros (Greece): Implications for reactions at the slab–mantle interface: Lithos, v. 107, no. 1-2, p. 53–67, doi: 10.1016/j.lithos.2008.07.015.

Philippon, Gueydan, Pitra, and Brun, J., 2013, Preservation of subduction-related prograde deformation in lawsonite pseudomorph-bearing rocks: Journal of Metamorphic Geology, v. 31, no. 5, p. 571–583, doi: 10.1111/jmg.12035.

Putlitz, Cosca, M. A., and Schumacher, J. C., 2005, Prograde mica 40Ar/39Ar growth ages recorded in high pressure rocks (Syros, Cyclades, Greece): Chemical Geology, v. 214, no. 1-2, p. 79–98, doi: 10.1016/j.chemgeo.2004.08.056.

Ridley, J., 1982, Arcuate lineation trends in a deep level, ductile thrust belt, syros, Greece, Tectonophysics, v. 88, i. 3–4, p. 347-360, doi; 10.1016/0040-1951(82)90246-3.

Ridley J., 1984, The significant of deformation associated with blueschist facies metamorphism on the Aegean Island of Syros, Geological Society, London, Special Publications, v. 17, i. 1, p. 545-550, doi: 10.1144/GSL.SP.1984.017.01.41

Ring, U., Glodny, J., Will, T., and Thomson, S., 2010, The Hellenic Subduction System: High-Pressure Metamorphism, Exhumation, Normal Faulting, and Large-Scale Extension: Earth and Planetary Sciences, v. 38, no. 1, p. 45–76, doi: 10.1146/annurev.earth.050708.170910.

Schumacher, J., Brady, J., Cheney, J., and Tonnsen, R., 2008, Glaucophane-bearing Marbles on Syros, Greece: Journal of Petrology, v. 49, no. 9, p. 1667–1686, doi: 10.1093/petrology/egn042.

Tomaschek, F., Kennedy, A., K., Villa, I., M., Lagos, M., Ballhaus, C., 2003, Zircons from Syros, Cyclades, Greece--Recrystallization and Mobilization of Zircon During High-Pressure Metamorphism', Journal of Petrology, v. 44, no. 11, p. 1977-2002, doi; 10.1093/petrology/egg067

Trotet, F., Jolivet, L., and Vidal., O., 2001, Tectono-metamorphic evolution of Syros and Sifnos islands (Cyclades, Greece): Tectonophysics, v. 338, no. 2, p. 179–206, doi: 10.1016/S0040-1951(01)00138-X.

Trotet, F., Vidal., O., and Jolivet, L., 2001, Exhumation of Syros and Sifnos metamorphic rocks (Cyclades, Greece). New constraints on the *P*-*T* paths: European Journal of Mineralogy, v. 13, no. 5, p. 901920, doi: 10.1127/0935-1221/2001/0013-0901.

Zhang, Y., 1998, Mechanical and phase equilibria in inclusion–host systems: Earth and Planetary Science Letters, v. 157, no. 3-4, p. 209-222, doi: 10.1016/S0012-821X(98)00036-3

Chapter 2

Thermodynamic Constraints on Carbonate Breakdown and Carbon Volatility during Subduction

Jennifer Gorce[1], Mark Caddick[1], R. J. Bodnar[1]

Department of Geosciences, Virginia Tech, Blacksburg, Virginia, 24061, USA

To be submitted to Earth and Planetary Science Letters

2.1 ABSTRACT

High pressure breakdown of carbonate minerals is frequently cited as an important mechanism that leads to carbon release from subducted rocks. Previous estimates of carbon input into the atmosphere via subduction related arc volcanism, calculated through the use of helium and carbon isotopes, have suggested that up to 85% of the 0.3–5.6x10^{12} moles of carbon that is released per year at volcanic arcs originates from the subducting slab. However, experimental data and thermodynamic models generally predict that the stability of carbonate minerals in the subducting slab extends to mantle depths greater than arc-generating magma depths of about 150 km, implying that breakdown of carbonate phases may not contribute a sufficient amount of C to match expectations.

To account for this discrepancy, previous workers have suggested that the generation of volatile C from subducting slabs is driven by the addition of H_2O-rich fluids that promote dissolution of carbonate-rich lithologies. Here, we use thermodynamic modeling to explore the feasibility of H_2O-mediated decarbonation phenomenon by addressing the following questions: 1) are externally-derived H_2O-rich fluids capable of driving dissolution of carbonate minerals within the altered basaltic cap of the subducting lithosphere at subarc conditions? 2.) Is the source of the hydrous fluids associated with breakdown of serpentine at subarc conditions? In our thermodynamic model we calculate equilibrium mineral assemblages and fluid compositions (assuming a simple H_2O–CO_2 binary) for typical lithologies, assuming a range of subduction zone geotherms, and explore the implications of addition of fluids at various stages.

Results suggest that *P-T* conditions of hotter subduction systems are more favorable to the dissolution of carbonate. The availability of external fluid plays an important role in balancing the global carbon budget, and the depth at which deserpentinization reactions occur strongly controls the availability of fluids for slab decarbonation. These results correlate with C fluxes measured at volcanic arcs, where colder subduction zones produced higher C fluxes.

Keywords: Subduction, fluids, carbon, volatiles

2.2 INTRODUCTION

The global carbon cycle describes the movement and storage of carbon on earth as an interconnected series of fluxes between reservoirs. Our understanding of the global carbon cycle has changed dramatically in recent years as new data become available, especially as our understanding of subduction processes has improved. Historically, the study of the carbon cycle focused mainly on surficial and biological processes, but evidence such as the presence of diamonds in kimberlites suggested early on that the deep earth is likely a major reservoir in the global carbon cycle (Gold, 1973). Carbon and helium isotope studies in the late 1980's and early 1990's (e.g. Marty and Jambon, 1987; Sano and Marty, 1995) correlated the emissions of carbon from volcanic arcs with the subducting lithosphere, implying that carbon could be recycled into

the deep earth and returned to the surface via subduction and volcanic processes. Subduction zones represent the only place on earth where material from the earth's surface is returned to the deep mantle, and thus understanding the processes at convergent boundaries is critical to our understanding of the global carbon cycle.

Reported carbon fluxes based on helium and carbon isotope studies (Marty and Jambon, 1987; Sano and Marty, 1995; Sano and Williams, 1996; Hilton et al., 2002) range from 0.3–3.1 × 10^{12} moles of CO_2/yr. In general, isotope data indicate that the carbon released at volcanic arcs is dominated by a component sourced from the subducting slab (rather than from the mantle or sediment cap), ranging from 53-84% and averaging 73% of volcanic carbon emissions (Marty and Jambon, 1987; Hilton et al., 2002; Sano and Williams, 1996). A recent study (Mason et al., 2017) compiled global δC^{13} and He^3 that suggests that assimilation of crustal carbon during island arc formation contributes significantly to the CO_2 budget at volcanic arcs, and older, more mature continental arcs have isotopic compositions that are in better agreement with crustal values. The implication is that carbon sequestered in the deeper portion of the subducted lithosphere is returned to the deep earth while carbon sequestered in the more shallow parts of the crust of the overlying slab is released to the surface via arc magmatism.

Thermodynamic models and experimental data predict that carbonated minerals should be stable well beyond the depth at which arc magmas are generated (subarc environment), and should, therefore, be returned to the deep mantle (Kerrick and Connolly, 1998&2001; Isshiki et al., 2004; Brenker et al., 2007; Poli et al., 2009; Baxter and Caddick, 2013). Experimental studies (Yaxley and Green, 1994; Molina and Poli, 2000) to determine the stability of carbon-bearing phases in the deep earth revealed that phases like dolomite (Mg-Ca carbonate) and magnesite (Mg-endmember carbonate) are stable above 1.8 GPa and between 665-730°C; well within the eclogite facies field. Canil and Scarfe (1990) reported that carbonates could be stable up to depths of 350 km, well beyond subarc depths. Additional studies (e.g. Kraft et al., 1991; Biellmann et al., 1993; Isshiki et al., 2003) suggest that carbonates remain stable at pressures corresponding with the base of the upper mantle (20 GPa) and the top of the lower mantle (115 GPa). Studies of Ultra-High Pressure (UHP) terranes (Zhang et al., 2002; Brenker et al., 2007) have reported carbonate inclusions in UHP phases such as diamond.

Numerical models that utilize thermodynamic phase equilibria are generally in agreement with experimental studies. Kerrick and Connolly (1998) explored dehydration of the subducting

slab and quantified decarbonation during prograde metamorphism of subducted ophicarbonates. Their results showed that while dehydration reactions in metasediments are discontinuous, water loss largely occurs below volcanic arcs, at ~550-650°C and 100-150 km depth, while decarbonation of metabasalts and ophicarbonates requires higher temperatures at those same depths (only 1.5% carbonate loss at 2.8-4 GPa and 700-900°C). Later studies explored the effect of bulk rock composition and subduction geotherm on H_2O and carbon liberation (Kerrick and Connolly, 2001a; Kerrick and Connolly, 2001b), and concluded that both sediments and altered basalts undergoing cold subduction experience little to no devolatilization, while those undergoing warmer subduction experience dehydration but not decarbonation, and those undergoing hot subduction experience dehydration and very little (1.5% loss) decarbonation.

To resolve the discrepancy between measured and modeled carbon fluxes, several workers have proposed that externally-derived hydrated fluids can decarbonate subducted basalt, liberate carbon, and transfer it into the overlying mantle wedge, where it can be incorporated into melt that forms volcanic arc magmas (i.e. Kerrick and Connolly, 2001a; 2001b, Connolly, 2005; Gorman et al., 2006; Ague and Nicolescu, 2014; Kelemen and Manning, 2015). Gorman et al., (2006) modeled closed and open system behavior for different fluid flow regimes during subduction and recognized that carbon liberation requires open system behavior whereby fluids can leave the subducting slab, rise buoyantly, and infiltrate overlying lithologies. Their numerical model predicts a global CO_2 flux of $0.35–3.12 \times 10^{12}$ moles of CO_2/yr. This amount is similar to estimates based on outgassing measurements (Sano and Williams, 1996; Marty et al., 1989; Williams et al., 1992; Allard, 1992; Varekamp et al., 1992; Marty and Tolstikhin 1998). As high a_{H2O} fluids interact with fluid-undersaturated, carbonated lithologies, carbonate minerals dissolve as the system episodically deviates from equilibrium. Here, we examine how infiltration of external fluids affects phase equilibria, assuming open system, pervasive fluid flow. It should be noted that this study ignores the consequences of slab melting and the incorporation of carbon into slab-derived melts which also ascend to the surface and get incorporated into volcanic arcs (e.g. Dasgupta et al., 2004; Dasgupta and Hirschmann, 2010)

Hydration of the overlying mantle wedge, melt production and subsequent volcanic arc activity, and decarbonation of carbon-bearing lithologies, all require availability of H_2O-rich fluids at approximately subarc pressure-temperature (*P*-*T*) conditions. The breakdown of serpentine to olivine and orthopyroxene produces ~13 wt% H_2O and is frequently cited as the primary source

of fluid in the subarc of the subduction zone (e.g. Ulmer and Trommsdorf, 1995; Schmidt and Poli, 1998). At subarc depths, dehydration of serpentine is thought to produce hydrous fluids in sufficient quantities to decarbonate the overlying altered basalt (Kerrick and Connolly, 1998). This interpretation is consistent with predictions that altered basaltic and sedimentary lithologies dehydrate at forearc depths in most cases (Schmidt and Poli, 1998; Kerrick and Connolly, 2001a&b; Dragovic et al., 2015). However, constraints on the extent of decarbonation produced by addition of serpentine-derived fluids into crustal lithologies in the subducting slab are currently scarce.

This study seeks to expand on previous studies (e.g. Kerrick and Connolly, 2001a&b; Gorman et al., 2006) by quantifying the amount and composition of fluid required to facilitate carbonate mineral breakdown and subsequent carbon liberation during open system fluid/rock interactions. We use equilibrium thermodynamic and solubility models to estimate the amount of fluid that is likely to be liberated during deserpentinization, within a range of plausible subduction zone thermal structures, and examine the ability of the hydrous fluid to drive dissolution of carbonate minerals in overlying lithologies. We focus specifically on reactions at approximate subarc depths, with the intention of exploring the processes that liberate carbon that is eventually emitted from volcanic arcs.

2.3 MATERIALS AND METHODS

To understand the interaction between subducted basaltic lithologies and external aqueous fluids, we use a multistage thermodynamic modeling approach. First, we calculate stable mineral assemblages along a subduction geotherm (Figure 2.1A), considering devolatilization induced evolution of the composition of a typical hydrated and carbonated basalt (Cottrell and Kelley, 2011) subducted to a depth directly below the volcanic arc (subarc), as constrained by Syracuse et al., (2010). We then take this calculated composition of the rock at the subarc and calculate how mineral phase equilibria change in response to the infiltration of an H_2O-CO_2 fluid (Figure 2.1B) Finally, we explore whether aqueous fluids are sufficiently available at appropriate subarc conditions to facilitate this by examining the metamorphic evolution of underlying ultramafic lithologies and the *P-T* conditions in which they devolatilize (Figure 2.1C).

2.3.1 Mineral phase equilibria along subduction geotherms

We have calculated phase equilibria for a hydrated mid-ocean ridge basalt (Table 2.1; Cottrell and Kelley, 2011) along three possible endmember subduction geotherms. Top-of-slab geotherm *P-T* paths (Figure 2.2), chosen to represent hot (Cascadia), medium temperature (Nicaragua), and cold (Honshu) subduction, were constructed by Syracuse et al., (2010) and modified by van Keken et al., (2011). Other approaches suggest significantly different and generally hotter geotherms (i.e Gerya et al., 2002; Peacock, 2003; Penniston-Dorland et al., 2015) however, the Syracuse et al., (2010) results represent reasonable endmember geotherms that can be used to characterize broad trends across a suite of different subduction zones temperatures. Our work provides minimum constraints on amounts of carbon liberated because studies such as Kerrick and Connolly (1998, 2001a, 2001b) suggest that hotter subduction geotherms would enhance decarbonation and the promote liberation of carbon from the subducting slab. Fluids in equilibrium with the hydrated MORB are assumed to be an H_2O-CO_2 binary, with properties determined by a Compensated Redlich-Kwong (CORK) equation of state (Holland and Powell, 1991).

Stable phases in a hydrated MORB (Cottrell and Kelley, 2010) are calculated at one degree Celsius increments along a given subduction *P-T* path using a free energy minimization method implemented in the modeling software Perple_X, (i.e. Connolly, 2005). Thermodynamic data are taken from Holland and Powell (1998) with the various mineral solution models considered given in Table 2.2. Any fluid or garnet produced during prograde metamorphism of the subducting slab is removed from the effective bulk rock composition and is unavailable for subsequent calculations (see Baxter and Caddick, 2013 for details). We fractionate fluid and garnet from the system because we assume that fluid is a mobile phase that leaves the system as soon as it is formed, and garnet typically displays strong zoning patterns, implying that elements remain sequestered in the garnet during later periods of metamorphism and are not re-introduced into the system. The results of these calculations (Figure 2.3) allow us to predict the mineralogical evolution of subducted lithologies. (Dragovic et al., 2012; Baxter and Caddick, 2013).

We use the above calculations to predict the anhydrous bulk rock composition and the extent of dehydration at the geometrically constrained subarc *P-T* conditions in Syracuse et al., (2010) for Honshu (cold geotherm), Nicaragua (medium geotherm), and Cascadia (hot geotherm).

2.3.2 Calculating the thermodynamic response to infiltrating external fluids

To explore variations in the equilibrium mineral assemblage of metabasalts in response to the infiltration of H_2O-CO_2 fluids at subarc *P-T* conditions, we start with the calculated bulk rock composition of hydrated MORB at subarc *P-T* conditions for Honshu, Nicaragua and Cascadia (see section 1.2.1) and examine changes in mineralogy associated with addition of H_2O and/or CO_2 to the system (Figure 4a-c). Calculations use the same thermodynamic data as in section 2.3.1 When compared to the results from section 2.3.1, results from the fluid-mediated reactions yield the amount of carbonate stabilized or lost per cubic meter of subducted hydrated MORB as externally-derived fluids of various H_2O:CO_2 ratios are added at the *P-T* condition inferred for the top of slab at sub-arc depths. The calculation only considers the mineralogical response to equilibration at a new bulk-rock composition, with the amount of carbonate dissolved into the fluids calculated separately, as described below. Thus, a primary response to addition of a hydrous fluid involves stabilization of increasing amounts of garnet and clinopyroxene that sequester some portion of the Ca, Mg and Fe that would otherwise be incorporated into carbonate, leading to a net loss of mineralogically-bound carbon. Assuming that carbonate mineral breakdown is directly proportional to C release (1 mole of C per 1 mole of [Ca–Mg–Fe]CO_3), we can, therefore, quantify the amount of C liberated per mole of fluid added to a unit volume or mass of rock, and can quantify the composition of the fluid associated with carbonate mineral breakdown (Figure 2.4d).

2.3.3 Estimates of the amount of calcite that dissolves into aqueous fluids at subarc conditions

Calculations described in section 2.2 considered simple H_2O-CO_2 binary fluids that do not permit dissolution of other species into the fluid. Here, we determine the relative contribution of calcite solubility in internally derived fluids versus incorporation CO_2 into aqueous, externally derived fluids on carbon liberation during subduction. Using equations from Newton and Manning (2002), we simply calculate the solubility of $CaCO_3$ in pure H_2O as a function of pressure and temperature for cold(Honshu), medium(Nicaragua), and hot(Cascadia) subduction paths. We take the results from the hydrated basalt (Figure 2.2) and calculate the amount of fluid release at any *P-T* point during subduction. Assuming that this fluid is pure H_2O, we determine the amount of $CaCO_3$ dissolved in fluid produced at each *P-T* point along a given geotherm. The amount of dissolved $CaCO_3$ is subtracted from the total carbonate mineral content of the rock and the difference is plotted as a function of pressure and temperature (Figure 2.5).

2.3.4 Constraining the *P-T* conditions of fluid liberation from serpentine breakdown

Assuming broadly upward-flow within the slab, fluids should migrate from underlying lithologies into basaltic rocks in the upper part of the slab as described in section 2.3.2. The largest fluid flux at subarc conditions is likely to be associated with dehydration reactions in ultra-mafic rocks, depending on exact *P-T* conditions and the extent of pre-subduction serpentinization (e.g. Hacker 2008; Rüpke, 2004; Schmidt and Poli, 1998&2003). We thus calculate the *P-T* conditions of serpentine breakdown at various locations within the slab to determine the conditions whereby fluids generated by subarc deserpentinization can interact with overlying mafic lithologies. The evolution of ultra-mafic lithologies is constrained by the evolving mineral assemblages along *P-T* trajectories for rocks located between 1 and 20 km orthogonally below the upper surface of the slab (Syracuse et al., 2010; van Keken et al., 2011). In all cases, we approximate the input rock composition as a simplified hydrated harzburgite (Miyashiro et al., 1969) (Table 2.1), assuming that the evolved fluids are pure H_2O. Stable assemblages are determined using the same methods and thermodynamic data as described above for the hydrated MORB (see table 2.2), and fluids produced at each *P-T* point along the geotherm are removed from the effective bulk rock composition and excluded from subsequent calculations. The evolution of the mineral assemblage is tracked, with *P-T* paths for all positions within the slab showing loss of antigorite over a narrow *P-T* window. The depth of the deserpentinization event varies substantially as a function of the thermal profile at various positions within each slab, and is plotted relative to the depth of the sub-arc slab top in figure 2.6.

2.4 RESULTS

2.4.1 Mineral evolution of subducted hydrated MORB

A summary of mineral assemblages calculated for the basaltic lithology is shown in figure 2.3. Cold subduction (e.g. Honshu) results in blueschist facies hydrous minerals such as glaucophane and lawsonite being stable from ~0.5-2.6 GPa. Beyond 2.6 GPa, glaucophane and lawsonite breakdown to form garnet, pyroxene, quartz, and kyanite. Approximately 10 vol % carbonate remains stable at all depths. Approximately 1.5 vol % white mica is also stable throughout, consistent with the idea that subducted basaltic and sedimentary crust carries water into the deep

earth (Hacker 2008). At subarc conditions (3.01 GPa and 705°C) a hydrated MORB is expected to contain <1 mol % H_2O and about 4-5 mol% CO_2 and to be in equilibrium with a fluid with a composition X_{H2O}=0.99.

Zeolite minerals are expected to breakdown earlier than in the Honshu case during medium temperature subduction (Nicaragua). The transition from blueschist to eclogite mineral facies is predicted to occur at slightly shallower depths, again coincident with the initiation of garnet, pyroxene and kyanite stability and an associated pulse of dehydration (Baxter & Caddick, 2013). A more striking difference between Nicaragua and Honshu occurs at approximate subarc conditions, where the abundance of garnet and quartz increase at the expense of pyroxene and kyanite in the Nicaraguan subarc (5.33 GPa and 876°C) but not in Honshu. At Nicaraguan subarc conditions (5.33 GPa and 876°C), a hydrated MORB is expected to contain <1 mol % H_2O and about 5-6 mol% CO_2 and be in equilibrium with a fluid with a composition X_{H2O}=0.97.

Unlike cold and medium temperature subduction geotherms, during hot subduction (Cascadia) lawsonite is not stable during blueschist metamorphism (Peacock, 1993; Peacock et al., 2003). Instead, epidote and amphibole coexist to approximately 2.3 GPa, where they break down to form kyanite, omphacite, garnet, and quartz. Garnet begins to grow at a pressure that is 1.0 GPa lower (approximately 30 km shallower) than in both Honshu and Nicaragua and the blueschist/eclogite boundary is more gradual., The breakdown of amphibole and growth of pyroxene and kyanite occur over a 0.3-0.4 GPa interval., At Cascadian subarc conditions (2.87 GPa and 912°C) subducted hydrated MORB is predicted to contain <1 mol% H_2O and 4-5 mol% CO_2 and be in equilibrium with a fluid with a composition X_{H2O}=0.94.

In each of the examples, the estimated amount of carbonate lost is small over the considered pressure range, implying only minor carbon devolatilization that is consistent with previous findings (Yaxley and Green, 1994; Kerrick and Connolly, 1998 &2001ab; Molina and Poli, 2000; Isshiki et al., 2004; Brenker et al., 2007; Poli et al., 2009; Baxter and Caddick, 2013).

2.4.2 Fluid/rock interactions at subarc *P-T* conditions

Figure 2.4 shows the manner in which thermodynamically stable, subarc mineral assemblages evolve in the presence of externally derived H_2O-CO_2 fluids, contoured for the difference in the abundance of carbonate per cubic meter of rock relative to the result for the progressively devolatilized MORB at subarc conditions (i.e. Figures 3a-c at subarc conditions). The variation in

the amount of carbonate is expressed as Δcarb, with contours for Δcarb = 0 implying an input fluid composition that is in equilibrium with the primary lithology and therefore driving little mineralogical change. Carbonate minerals are expected to precipitate when Δcarb > 0, driven by an increased system CO_2 content. The abundance of carbonate minerals decreased when Δcarb < 0, driven primarily by an increase in the abundance of hydrous phases and resultant decrease in the availability of Ca, Mg and Fe. The slope of the contour representing Δcarb = 0 is steeper for hotter subduction geotherms such as Cascadia, implying that addition of smaller quantities of lower X_{H2O} fluids is capable of driving equilibria away from carbonate stability. For cooler slab top geotherms, relatively large inputs of high X_{H2O} fluids results in the breakdown of little carbonate in the absence of dissolution considerations (described below).

The composition and amount of externally derived fluid added to the hydrated MORB have also been estimated (Figure 2.4d). When superimposed on plots of Δcarb, the amount and composition of the fluid needed to liberate a certain amount of carbon per unit volume of rock may be estimated. For example, addition of 0.0145 kg (1.05×10^{-5} m^3) of an H_2O-fluid to 1 m^3 of hydrated basalt (~ 3481 kg of rock) at 5.23 GPa and 876°C (the subarc of the Nicaragua example) results in loss of approximately 3.22 kg of carbonate minerals. This equates to the liberation of approximately 17.48 moles of C (0.21 kg of C) per cubic meter of hydrated MORB.

In cold subduction zones, loss of carbonates only occurs within a narrow window of fluid compositional space, generally requiring fluids with $X_{H2O} > 0.97$. In the medium temperature example, fluids with a minimum value of $X_{H2O} > 0.95$ are required to dissolve carbonates. In the hot, Cascadia example, loss of carbonate only occurs when $X_{H2O} > 0.75$. These results imply that hotter subduction zones are more favorable for carbonate breakdown, in agreement with previous work by Kerrick and Connolly (2001), where higher volatile fluxes were produced from basalt subducted along hotter geotherms.

2.4.3 Calcite solubility in H_2O along subduction *P-T* paths

Figure 2.5A-C shows the mass off calcite per $1m^3$ hydrated MORB that is stable along cold (A), medium temperature (B), and hot (C) subduction geotherms. Dashed lines represent the amount of calcite (kg calcite/m^3 of rock) if only CO_2 dissolves into the fluid at each *P-T* point along a geotherm. Grey lines represent the amount of calcite (kg of calcite/m^3) if we assume that calcite dissolution occurs during the production of internally derived fluids. There is little difference

between the two curves, and differences are only observed later along the subduction path, implying that carbonate dissolution is not occurring during the early stages of subduction. Cooler subduction is predicted to stabilize more calcite compared to hot subduction. Figure 2.5D-F shows the total change in the amount of calcite if internally derived fluids promote carbonate dissolution. In cold subduction the maximum amount of calcite dissolved per m^3 of MORB is approximately 4 kg. In medium subduction geotherm environments, the maximum amount of calcite dissolved per m^3 of MORB is 3 kg. In hot subduction geotherms, the maximum amount of calcite dissolved per m^3 of MORB is approximately 2.5 kg.

We interpret the portions of the subduction path shown in Figure 5 where the slope = 0 (i. e. in Δ kg carbonate/m^3 of rock is constant) to represent *P-T* conditions along the subduction path where the dissolution of calcite does not occur. In contrast, areas where the slope > 0 are interpreted to be *P-T* conditions along the subduction path where dissolution of calcite from internally produced fluids could be important because dissolution results in a larger change in the mass of carbonate per unit of rock than do changes in the mineral assemblage based on thermodynamic equilibrium. In Honshu, the region in which the mass of calcite per unit volume of rock changes significantly occurs over the range from 2.3-2.9 GPa, in Nicaragua the change occurs from 2.4-2.8 GPa, and in Cascadia, the change occurs from 1.3-2.8 GPa. For each geotherm, a slope > 0 coincides with the breakdown of amphibole and subsequent growth of omphacite. This implies that the liberation of H_2O from the amphibole breakdown reaction is the source of internal fluid that leads to calcite dissolution, and that calcite dissolution is most significant at the blueschist/eclogite transition. It should be noted that a loss of 2.5-4 kg of calcite /m^3 of rock, as calculated above, exceeds the amount of calcite breakdown needed to produce C fluxes (0.5-0.7 kg of calcite/m^3 of rock) reported by Jarrard et al., (2003).

However, the blueschist/eclogite transition (Figure 2.5, vertical black dashed line) consistently occurs at depths shallower more shallow than the subarc depth calculated by Syracuse et al., (2010) (Figure 2.5, vertical grey dashed line), implying that while dissolution promotes significant decarbonation (25-40 moles of C per m^3 of rock), the carbon liberated via calcite dissolution by internally derived fluids occurs at 0.5-3.0 GPa (approximately 15-90 km), before the top of the slab reaches subarc depths. Assuming that any fluid produced rises buoyantly, carbon liberated from fluids produced by amphibole breakdown in this case will not interact with subarc melts. At the subarc, the subducted basalt would be essentially dry, and would not produce

sufficient amounts of fluid to promote dissolution of calcite. Thus, carbon liberation must be driven by the introduction of externally derived fluid infiltrating the rock at subarc conditions, where the source is most likely serpentine breakdown in underlying lithologies.

2.4.4 Modeling serpentine breakdown in subducted oceanic lithosphere

The depth of deserpentinization, and thus availability of fluid, is largely controlled by the orthogonal distance of serpentine lithologies to the top of the subducting slab because the geotherms of the interior of the subducting slab are colder than top of the slab geotherms, and breakdown of serpentine is largely an isothermal reaction (Marty and Tolskikhin, 1998; Schmidt and Poli, 1997; Ulmer and Trommsdorff, 1991; Hacker et al., 2003; Rupke et al., 2012). We have estimated differences in the depth at which fluids are available for hot, medium, and cold temperature subduction (Figure 2.6). If at any point the depth of serpentine breakdown is greater than the depth to the top of the slab at the subarc (geometrically constrained in Syracuse et al., 2010), it was assumed that liberated H_2O rises buoyantly and infiltrates the overlying carbon-bearing lithologies, releasing C into arc magmas. If at any point the depth of deserpenitinization was shallower than the geometrically constrained subarc depth (dashed line in Figure 2.6), then it was assumed that fluid produced at those depths did not interact with carbon-bearing lithologies at the subarc. If at any point the depth of deserpenitinization was deeper than the subarc depth (dark grey regions in Figure 2.6), it was assumed that liberated H_2O rises buoyantly and infiltrates the overlying carbon-bearing lithologies, passing this C into arc magmas. Our results predict that for cold subduction, fluids generated 3km from the slab surface and deeper will interact with basaltic lithologies under the subarc while for medium temperature subduction geotherms, fluid generated 9-18 km from the slab surface will infiltrate the subarc basalt. This implies that colder subduction zones such as Honshu, have a larger region of the subduction slab that can contribute external fluids to facilitate carbon liberation than medium temperature subduction zones such as Nicaragua. In contrast, for hot temperature geotherms such as Cascadia, dehydration of the hydrated harzburgite occurs before subarc depths, implying that fluid is not available to facilitate the release of carbon.

2.5 DISCUSSION

2.5.1 Driving mechanisms of carbonate mineral breakdown: Departure from equilibrium

The extent of decarbonation of hydrated MORB along different subduction geotherms is influenced by fluid-rock interactions. The mineral assemblage present during subduction will influence the X_{CO2} content of the equilibrium fluid (Molina and Poli, 2000), with the mineral assemblage governing fluid/rock interactions in Cascadia being different from that in Honshu. For example, previous studies (Yaxley and Green, 1994; Molina and Poli, 2000) concluded that decarbonation of basaltic crust only occurs in hot, shallow geologic environments. The extended presence of hydrous phases such as amphibole and lawsonite in colder subduction environments is important because these minerals buffer the H_2O and result in an increase in X_{H2O} of the fluid in equilibrium with the subducted basalt. Therefore, at subarc conditions in a hot geotherm a basalt will be in equilibrium with a higher X_{CO2} fluid than a similar rock at subarc conditions in a cold geotherm. When a rock is infiltrated by an H_2O rich fluid, a hotter rock will be dehydrated to a greater extent than a cooler rock, and thus will be further from equilibrium in the presence if H_2O rich fluids. This creates a greater chemical potential gradient in which to drive mineral phase equilibria reactions, such as the breakdown of carbonate bearing lithologies in hotter subduction forearcs. Results from this study (Figure 2.4) illustrate these principles and are in agreement with previous works (Molina and Poli, 2000; Connolly, 2005).

2.5.2 Constraints on maximum CO_2 fluxes and implications for fluid availability during subduction

Modeling of fluid/rock interactions at subarc conditions along hot, medium, and cold temperature subduction geotherms demonstrates that a greater mass of external fluid with a higher X_{H2O} results in the breakdown of a greater mass of carbonate minerals per unit of rock (Fig 2.4). In cold subduction, a maximum of approximately 7 wt % of the total carbonate minerals per m^3 of basalt (23 kg of carbonate/m^3 of rock) will break down at subarc conditions by distributing CO_2 into the fluid. This liberates CaO and MgO that stabilizes additional garnet and clinopyroxene, which requires additional breakdown of coesite and kyanite. A similar phenomenon has been observed in eclogitc veins in Tianshan, China (John et al., 2008).

In medium temperature subduction a maximum of 9 wt % of carbonate minerals (38 kg of carbonate/m^3 of rock) is lost, fluid/rock interactions similar to those in the cold subduction example are observed. In hot subduction, a maximum of 196 kg of carbonate/m3 of rock (54 wt% loss) breaks down. These results can now be applied to subducting systems to predict the CO_2 flux along the Cascadia, Nicaragua, and Honshu subduction zones and compare these data with published results (Table 2.3).

To calculate the average volume of rock passing through the subarc per year, we assume an average thickness of the subducted basalt of 7 km and take the length and convergence rate of Cascadia, Nicaragua, and Hoshu subduction zones from Jarrard et al., (2003). Then, we multiply the value we obtained for carbonate mineral breakdown by the volume flux to estimate the total amount of carbonate breakdown per year in a given subduction zone. Results are discussed below.

Our calculations (Table 2.3) show that adding 10 moles (about 18g) of H_2O to 1 m^3 of basalt at subarc conditions produces CO_2 fluxes that are 1-2 orders of magnitude higher than other workers have estimated (Jarrard et al., 2003; Fischer et al., 2007), implying that the availability of fluid is much less than 10 moles of H_2O per 1 m^3 of rock in subduction zones, or external fluids that interact with the subducted basalt are not pure H_2O fluids. Previously published values for carbon fluxes (10^{11}g/yr/km) can be achieved by breaking down 0.5-0.7 kg of carbonate minerals per m^3 of basalt, which would require 0.1-0.3 moles of fluid per m^3 of basalt. It should be noted that <1% of carbonate present per m^3 of rock needs to breakdown at the subarc in order to produce the fluxes measured at volcanic arcs, assuming that all CO_2 produced is passed directly into arc magmas.

Subduction zone fluids are chemically much more complex than pure H_2O, and the addition of as little as 2% CO_2 can substantially alter mineral phase equilibria (Molina and Poli, 2000; Yaxley and Green, 1998). However, Manning (2004) argues that H_2O is the dominate species in subduction zone fluids, and thus its behavior governs fluid behavior in these systems. Connolly (2005) modeled CO_2 solubility along a subduction geotherm and found that while maximum CO_2 solubility occurred around subarc conditions, X_{CO2} did not exceed 0.01, and Kelemen and Manning (2015) predict carbon concentrations on the order of 1000-2000 ppm in the fluid phase. Based on the results of this study (Figure 4), carbonate mineral breakdown occurs in the presence of external fluids when $X_{H2O} > 0.95$ in cold subduction, $X_{H2O} > 0.94$ in medium temperature subduction, and $X_{H2O} > 0.75$ in hot subduction, which is in good agreement with fluid compositions measured at

volcanic fumaroles ($0.96<X_{H2O}<1$) (Fischer, 2007). Thus, it is reasonable to assume that subduction-related fluids are dominated by H_2O.

Another way to produce lower CO_2 fluxes at volcanic arcs is to reduce the amount of external fluid available to infiltrate the rock. If we assume that the external fluid is pure H_2O, then we can calculate the minimum amount of H_2O needed to produce CO_2 fluxes comparable to those reported by Jarrard et al., (2003). In cold subduction, 0.65 kg of carbonate/m^3 of basalt must break down to liberate the amount of CO_2 measured across the Honshu volcanic arc ($2.17x10^{11}$ g of C/yr/km), which can be accomplished by adding 0.3 moles of H_2O/m^3 of basalt. In medium temperature subduction, 0.2 moles of H_2O/m^3 of basalt must be added in order to breakdown 0.53 kg of carbon/m^3 of basalt to liberate the $2.54x10^{11}$ g of C/yr/km of arc length for Nicaragua estimated by Jarrard et al., (2003). In hot subduction, the addition of <0.1 moles of H_2O /m^3 of basalt will facilitate the breakdown of 0.70 kg of carbon/m^3 of basalt, yielding a C flux similar to that measured along the Cascadia volcanic arc ($7.73x10^{10}$ g of C/yr/km). These small masses of fluid are reasonable if pervasive fluid flow along grain boundaries is the primary method of fluid transport in the subducting slab (Manning, 2004). However, these values can locally underestimate the amount of free, external fluid at the subarc if fluid transport is dominated by channelized fluid flow, where fluid/rock ratios are high near fluid channels, as suggested by many workers (e.g. Peacock, 1987; Zack and John, 2007; John et al., 2012). It is most likely that a combination of fluid composition and fluid availability play roles in controlling the extent of decarbonation of the subducting slab. We explore the relative contributions of both phenomena over a range of subduction thermal regimes below.

2.5.3 Assessing the contributions of fluid availability vs. *P-T* conditions on subarc C liberation

Thermodynamic modeling of serpentine dehydration within the subducting lithosphere (Figure 2.6) suggests that the availability of fluid plays an important role in the liberation of carbon at volcanic arcs. For example, our models for deserpenitinization along a Cascadian-like subduction path (hot subduction) suggest that the slab will fully dehydrate in the forearc (Figure 2.6), suggesting that CO_2 liberation at the subarc is driven by small amounts of externally derived H_2O-rich fluid infiltrating basaltic lithologies. In contrast, in cold subduction such as at Honshu, a fluid is continuously available to break down carbonates (Figure 2.6).

To understand the extent to which *P-T* conditions and fluid availability influence carbon liberation on a global scale, we examine CO_2 and H_2O fluxes from a range of volcanic arcs (22 volcanic arcs) reported in Jarrard et al., (2003) and compare the magnitude of those fluxes with the general thermal regime of the subduction zone (Figure 2.7). Fluxes were reported in moles per year and normalized per kilometer of along-strike subduction zone length.

The thermal parameter (φ) is used to describe the overall thermal regime of a subduction zone (Kirby et al., 1996; Syracuse et al., 2010). The thermal parameter is based on slab age, descent rate, and the sine of the slab dip. Syracuse et al., (2010) used this value to help constrain top of slab temperatures in models to predict the thermal structure of subduction zones based on decoupling mechanisms between the overriding and down-going slab. A higher value of φ implies that the subduction zone is colder (ex. φHonshu = 60.4) while a lower value implies that subduction is hotter (ex. φ Cascadia = 1).

If both criteria, *P-T* conditions and fluid availability, contribute equally to the breakdown of carbonate minerals, then results from this study suggest (see sections 2.4.2 and 2.4.4) that CO_2 fluxes should display a bell-shaped distribution over a range of thermal parameters, where the ideal combination of fluid availability, pressure, and temperature yield the highest CO_2 fluxes that can be found in medium temperature subduction. However, we see a linear trend between φ and CO_2 flux (Figure 7), implying that the availability of externally derived fluid plays a more important role in carbonate breakdown than thermodynamically favorable *P-T* conditions in specific subduction zones. This interpretation is consistent with observations made by Gorman et al., (2006), who concluded based on results of numerical modeling that enhanced decarbonation occurs when open system, pervasive fluid flow infiltrates in the subducting slab. The greater the mass of fluid flowing through the rock, the greater the potential for fluid/rock interactions and, thus, higher degrees of slab decarbonation. This trend is most strongly reflected in the fluxes reported by Jarrard et al., (2003) that suggest that the coldest subduction zones, such as Honshu and Tonga, release an order of magnitude more CO_2/yr/km than hot subduction zones like Cascadia and Mexico. According to our models (Figure 2.4) we would expect colder subduction to produce volcanic arcs with lower C fluxes and yet they produce the highest C fluxes across a global spectrum.

2.6 CONCLUSIONS

In closed system behavior in the absence of fluids, experimental and thermodynamic studies predict that carbonate minerals remain stable during subduction, and thus transport carbon into the deep earth. These studies are contrary to observations, which imply that a substantial amount of carbonate breaks down at subarc depths to account for carbon fluxes along volcanic arcs. Open system behavior, or the infiltration of subducted lithologies by H_2O-rich fluids has been shown to explain differences between experimental., thermodynamic and measured data (Connolly, 2005; Gorman et al., 2006). Here, we have quantified the amount and composition of fluid needed to facilitate carbonate mineral breakdown in basaltic lithologies at subarc conditions for a range of subduction thermal regimes. It was determined that the subducting slab need not be completely decarbonated to produce observed C fluxes, and that infiltration of 0.1-0.3 moles of pure H_2O into 1 m^3 rock will liberate sufficient carbon (<1 wt % loss of carbonate per m^3 of rock) to match global estimates.

While hotter subduction zones have *P-T* conditions that are more favorable for decarbonation compared to colder subduction, the extent of decarbonation is largely dependent on the availability of fluid from the dehydration of serpentine. Thus, more carbon is liberated in colder subduction per km of slab per year because fluid is continuously available to react with subducting basalt. Along hotter subduction geotherms, the majority of the fluid generated from the breakdown of serpentine is lost before subarc conditions are reached.

2.7 REFERENCES

Auzanneau, E., Schmidt, M., Vielzeuf, D., and Connolly, J., 2009, Titanium in phengite: a geobarometer for high temperature eclogites: Contributions to Mineralogy and Petrology, v. 159, no. 1, p. 1–24, doi: 10.1007/s00410-009-0412-7.

Ague, J., and Nicolescu, S., 2014, Carbon dioxide released from subduction zones by fluid-mediated reactions: Nature Geoscience, v. 7, no. 5, p. 355–360, doi: 10.1038/ngeo2143.

Allard, P., Global emissions of helium-3 by subaerial volcanism. *Geophysical Research Letters* (1992). doi:10.1029/92GL00974

Baxter, E., and Caddick, M., 2013, Garnet growth as a proxy for progressive subduction zone dehydration: Geology, v. 41, no. 6, p. 643646, doi: 10.1130/G34004.1.

Bebout. G. E., 1991, Field-based evidence for devolatilization in subduction zones: implications for arc magmatism: Science. V.251 p. 413-6, doi: 10.1126/science.251.4992.413

Biellmann, C., Gillet, P., and Peyronneau, J., 1993, Experimental evidence for carbonate stability in the Earth's lower mantle: Earth and Planetary Science Letters, v. 118, no. 1-4, p. 31-41, doi: 10.1016/0012-821X(93)90157-5

Brenker, F., Vollmer, C., Vincze, L., Vekemans, B., Szymanski, A., Janssens, K., Szaloki, I., Nasdala, L., Joswig, W., and Kaminsky, F., 2007, Carbonates from the lower part of transition zone or even the lower mantle: Earth and Planetary Science Letters, v. 260, no. 1-2, p. 1–9, doi: 10.1016/j.epsl.2007.02.038.

Canil, D., and Scarfe, C. M., 1990, Phase relations in peridotite+ CO2 systems to 12 GPa: implications for the origin of kimberlite and carbonate stability in the Earth's upper mantle: Journal of Geophysical Research: Solid Earth, v. 95, no. B10, p. 15805-16, doi: 10.1029/JB095iB10p15805.

Coggon, R., and Holland, T., 2002, Mixing properties of phengitic micas and revised garnet-phengite thermobarometers: Journal of Metamorphic Geology, v. 20, no. 7, p. 683–696, doi: 10.1046/j.1525-1314.2002.00395.x.

Connolly, J. A. D., 2005, Computation of phase equilibria by linear programming: A tool for geodynamic modeling and its application to subduction zone decarbonation: Earth and Planetary Science Letters, v. 236, no. 1-2, doi: 10.1016/j.epsl.2005.04.033.

Cottrell, E., and Kelley, K., 2011, The oxidation state of Fe in MORB glasses and the oxygen fugacity of the upper mantle: Earth and Planetary Science Letters, v. 305, no. 3-4, p. 270–282, doi: 10.1016/j.epsl.2011.03.014.

Dasgupta, R., Hirschmann, M.M., Withers, A.C., 2004, Deep global cycling of carbon constrained by the solidus of anhydrous, carbonated eclogite under upper mantle conditions: Earth and Planetary Science Letters, v. 227, no. 1-2, p. 73-85, doi: 10.1016/j.epsl.2004.08.004

Dasgupta, R., Hirschmann, M.M., 2010, The deep carbon cycle and melting in Earth's interior: Earth and Planetary Science Letters, v. 298, no. 1-2, p. 1-13, doi: 10.1016/j.epsl.2010.06.039

Diener, J., Powell, R., and White, R., 2008, Quantitative phase petrology of cordierite–orthoamphibole gneisses and related rocks: Journal of Metamorphic Geology, v. 26, no. 8, p. 795–814, doi: 10.1111/j.1525-1314.2008.00791.x.

Diener, and Powell, 2012, Revised activity–composition models for clinopyroxene and amphibole: Journal of Metamorphic Geology, v. 30, no. 2, p. 131–142, doi: 10.1111/j.1525-1314.2011.00959.x.

Diener, J., Powell, R., White, R., and Holland, T., 2007, A new thermodynamic model for clino- and orthoamphiboles in the system Na2O–CaO–FeO–MgO–Al2O3–SiO2–H2O–O: Journal of Metamorphic Geology, v. 25, no. 6, p. 631–656, doi: 10.1111/j.1525-1314.2007.00720.x.

Dragovic, B., Baxter, E., and Caddick, M., 2015, Pulsed dehydration and garnet growth during subduction revealed by zoned garnet geochronology and thermodynamic modeling, Sifnos, Greece: Earth and Planetary Science Letters, v. 413, p. 111–122, doi: 10.1016/j.epsl.2014.12.024.

Fischer, T., 2008, Fluxes of volatiles (H2O, CO2, N2, Cl, F) from arc volcanoes: Geochemical Journal., v. 42, no. 1, p. 21–38, doi: 10.2343/geochemj.42.21.

Fuhrman, M. L., and Lindsley, D. H., 1988, Ternary-feldspar modeling and thermometry: American Mineralogist,

Gorman, P. J., and Kerrick, D. M., 2006, Modeling open system metamorphic decarbonation of subducting slabs: Geochemistry, Geophysics, Geosystems, v. 7, no. 4, p., doi: 10.1029/2005GC001125.

Green, E., Holland, T., and Powell, R., 2007, An order-disorder model for omphacitic pyroxenes in the system jadeite-diopside-hedenbergite-acmite, with applications to eclogitic rocks: American Mineralogist, v. 92, no. 7, p. 1181–1189, doi: 10.2138/am.2007.2401.

Hilton, D. R., Fischer, T. P. & Marty, B., 2002, Noble gases and volatile recycling at subduction zones. Reviews in mineralogy and geochemistry, v. 47**,** p. 319–370, doi: 10.2138/rmg.2002.47.9

Holland, T., and Powell, R., 1991, A Compensated-Redlich-Kwong (CORK) equation for volumes and fugacities of CO2 and H2O in the range 1 bar to 50 kbar and 100–1600 C: Contributions to Mineralogy and Petrology, v. 109, no. 2, p. 265-273, doi: 10.1007/BF00306484.

Holland, T., and Powell, R., 1998, An internally consistent thermodynamic data set for phases of petrological interest: Journal of Metamorphic Geology, v. 16, no. 3, p. 309–343, doi: 10.1111/j.1525-1314.1998.00140.x.

Isshiki, M., Irifune, T., Hirose, K., Ono, S., Ohishi, Y., Watanuki, T., Nishibori, E., Takata, M., and Sakata, M., 2004, Stability of magnesite and its high-pressure form in the lowermost mantle.: Nature, v. 427, no. 6969, p. 60–3, doi: 10.1038/nature02181.

Jarrard, R., 2003, Subduction fluxes of water, carbon dioxide, chlorine, and potassium: Geochemistry, Geophysics, Geosystems, v. 4, no. 5, p. n/a–n/a, doi: 10.1029/2002GC000392.

Kelemen, P., and Manning, C., 2015, Reevaluating carbon fluxes in subduction zones, what goes down, mostly comes up.: Proceedings of the National Academy of Sciences of the United States of America, v. 112, no. 30, p. 3997–4006, doi: 10.1073/pnas.1507889112

Kerrick, D. M, and Connolly, J., 1998, Subduction of ophicarbonates and recycling of CO2 and H2O: Geology, v. 26, no. 4, p. 375-378, doi: 10.1130/0091-7613(1998)026<0375:SOOARO>2.3.CO;2.

Kerrick, D., and Connolly, J., 2001, Metamorphic devolatilization of subducted marine sediments and the transport of volatiles into the Earth's mantle: Nature, v. 411, no. 6835, p. 293–296, doi: 10.1038/35077056.

Kerrick, D.M., and Connolly, J.A.D., 2001, Metamorphic devolatilization of subducted oceanic metabasalts: implications for seismicity, arc magmatism and volatile recycling: Earth and Planetary Science Letters, v. 189, no. 1-2, p. 19–29, doi: 10.1016/S0012-821X(01)00347-8

Kraft, S, Knittle, E, and Williams, Q, 1991, Carbonate stability in the Earth's mantle: a vibrational spectroscopic study of aragonite and dolomite at high pressures and temperatures: Journal of Geophysical Research: Solid Earth, v. 96, no. B11, p. 17997-18009, doi: 10.1029/91JB01749.

Manning, 2004, The chemistry of subduction-zone fluids: Earth and Planetary Science Letters, v. 223, no. 1-2, p. 1-16, doi: 10.1016/j.epsl.2004.04.030.

Marty, B., and Jambon, A., 1987, C3 He in volatile fluxes from the solid Earth: implications for carbon geodynamics. Earth and Planetary Science Letters, v. 83, no. 1-4, p. 16-26, doi:10.1016/0012-821X(87)90047-1

Marty, B., Jambon, A., Sano, Y., 1989, Helium isotopes and CO_2 in volcanic gases of Japan, v. 76, no. 1-2, p. 25-40, Chemical Geology, doi: 10.1016/0009-2541(89)90125-3

Massonne and Willner, 2008, Phase relations and dehydration behaviour of psammopelite and mid-ocean ridge basalt at very-low-grade to low-grade metamorphic conditions: European Journal of Mineralogy, v. 20, no. 5, p. 867-869, doi: 10.1127/0935-1221/2008/0020-1871

Mason, E., Edmonds, M., Turchyn, A. V., 2017, Remobilization of crustal carbon may dominate volcanic arc emissions: Science, v. 357, no. 6348, p. 290-294, doi: 10.1126/science.aan5049.

Miyashiro, A., Shido, F., and Ewing, M., 1969, Composition and origin of serpentinites from the Mid-Atlantic Ridge near 24^o and 30^o North Latitude: Contributions to Mineralogy and Petrology, v. 23, no. 2, p. 117–127, doi: 10.1007/BF00375173.

Molina, J. F., and Poli, S., 2000, Carbonate stability and fluid composition in subducted oceanic crust: an experimental study on H 2 O–CO 2-bearing basalts: Earth and Planetary Science Letters, v. 176, no. 3-4, p. 295-310, doi: 10.1016/S0012-821X(00)00021-2

Peacock, S., 1993, The importance of blueschist→ eclogite dehydration reactions in subducting oceanic crust: Geological Society of America Bulletin, v. 105, no. 5, p. 684-694, doi: 10.1130/0016-7606(1993)105<0684:TIOBED>2.3.CO;2.

Peacock, S., 2003, Thermal structure and metamorphic evolution of subducting slabs: Inside the subduction factory, p. 7-22, doi: 10.1029/138GM02.

Rüpke, L., Morgan, J., Hort, M., and Connolly, J., 2002, Are the regional variations in Central American arc lavas due to differing basaltic versus peridotitic slab sources of fluids?: Geology, v. 30, no. 11, p. 1035, doi: 10.1130/0091-7613(2002)030<1035:ATRVIC>2.0.CO;2.

Rüpke, L., Morgan, J., Hort, M., and Connolly, J., 2004, Serpentine and the subduction zone water cycle: Earth and Planetary Science Letters, v. 223, no. 1-2, doi: 10.1016/j.epsl.2004.04.018.

Sano, Y., and Marty, B., 1995, Origin of carbon in fumarolic gas from island arcs: Chemical Geology, v. 119, no, 1-4, p. 265-274, doi: 10.1016/0009-2541(94)00097-R

Sano, Y., and Williams, S. N., 1996, Fluxes of mantle and subducted carbon along convergent plate boundaries. Geophysical Research Letters, v. 23, no. 20, p. 2749-2752, doi:10.1029/96GL02260

Scambelluri, M., and Philippot, P., 2000, Deep fluids in subduction zones: Lithos, v. 55, no. 1-4, doi: 10.1016/S0024-4937(00)00046-3.

Schmidt, M., and Poli, S., 1998, Experimentally based water budgets for dehydrating slabs and consequences for arc magma generation: Earth and Planetary Science Letters, v. 163, no. 1-4, p. 361–379, doi: 10.1016/S0012-821X(98)00142-3

Smye, A., Greenwood, L., and Holland, T., 2010, Garnet–chloritoid–kyanite assemblages: eclogite facies indicators of subduction constraints in orogenic belts: Journal of Metamorphic Geology, v. 28, no. 7, p. 753–768, doi: 10.1111/j.1525-1314.2010.00889.x.

Syracuse, E., van Keken, P., and Abers, G., 2010, The global range of subduction zone thermal models: Physics of the Earth and Planetary Interiors, v. 183, no. 1-2, p. 73–90, doi: 10.1016/j.pepi.2010.02.004

Tolstikhin, I. N., and Marty, B., 1998, The evolution of terrestrial volatiles: a view from helium, neon, argon and nitrogen isotope modelling: Chemical Geology, v. 147, no. 1-2, p. 27-52, doi: 10.1016/S0009-2541(97)00170-8

Ulmer, P., and Trommsdorff, V., 1995, Serpentine stability to mantle depths and subduction-related magmatism: Science, v. 268, no. 5212, p. 858-861, doi: 10.1126/science.268.5212.858

van Keken, Hacker, B. R., Syracuse, E. M., Abers, G. A., 2011, Subduction factory: 4. Depth-dpendent flux of H_2O from subducting slabs worldwide, Journal of Geophysical Research: Solid Earth, v. 116, no. B1, doi: 10.1029/2010JB007922

Varekamp, J. C., Kreulen, R., Poorter, R., 1992, Carbon sources in arc volcanism, with implications for the carbon cycle: Terra Nova, v. 4, no. 3, p. 363-373, doi:10.1111/j.1365-3121.1992.tb00825.

Wallace, P. J., 2005, Volatiles in subduction zone magmas: concentrations and fluxes based on melt inclusion and volcanic gas data: Journal of Volcanology and Geothermal Research, v. 140, no. 1-3, p. 217-240, doi: 10.1016/j.jvolgeores.2004.07.023

Williams, S. N., Schaefer, S. J., Calvache, V., 1992, Global carbon dioxide emission to the atmosphere by volcanoes; Geochimic et Cosmochimica Acta, v. 56, no. 4, p. 1765-1770, doi: 10.1016/0016-7037(92)90243-C

White, R., Pomroy, N., and Powell, R., 2005, An in situ metatexite–diatexite transition in upper amphibolite facies rocks from Broken Hill, Australia: Journal of Metamorphic Geology, v. 23, no. 7, p. 579–602, doi: 10.1111/j.1525-1314.2005.00597.x.

White, R., Powell, R., and Clarke, G., 2002, The interpretation of reaction textures in Fe-rich metapelitic granulites of the Musgrave Block, central Australia: constraints from mineral equilibria calculations in the system K2O–FeO–MgO–Al2O3–SiO2–H2O–TiO2–Fe2O3: Journal of Metamorphic Geology, v. 20, no. 1, p. 41–55, doi: 10.1046/j.0263-4929.2001.00349.x.

Yaxley, G. M., and Green, D. H., 1994, Experimental demonstration of refractory carbonate-bearing eclogite and siliceous melt in the subduction regime: Earth and Planetary Science Letters, v. 128, no. 3, p. 313–325, doi: 10.1016/0012-821X(94)90153-8.

Zhang, L., Ellis, D., Williams, S., and Jiang, W., 2002, Ultra-high pressure metamorphism in western Tianshan, China: Part II. Evidence from magnesite in eclogite: American Mineralogist, v. 87, no. 7, p. 861–866, doi: 10.2138/am-2002-0708.

2.8 FIGURES

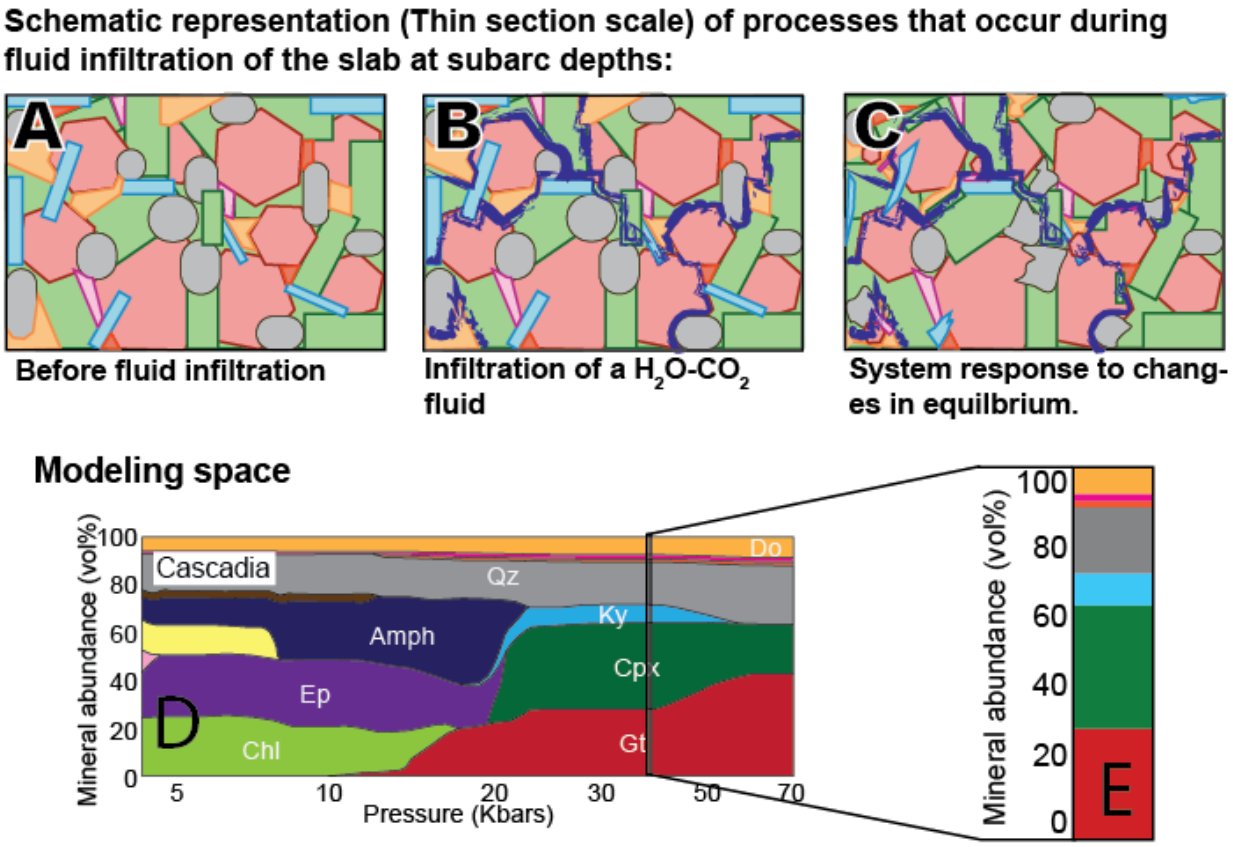

Figure 2.1: Schematic representation (Thin section scale) of processes that occur during fluid infiltration of the slab at subarc depths with (A) the predicted mineralogy of a hydrated basalt at subarc depths, (B) Infiltration of H_2O-CO_2 fluids, and (C) the system response to changes in equilibrium. Panels D and E illustrate how thermodynamic models predict how hydrated MORB evolves mineralogically during subduction (D), which is used in subsequent calculations (See figure 2.4)

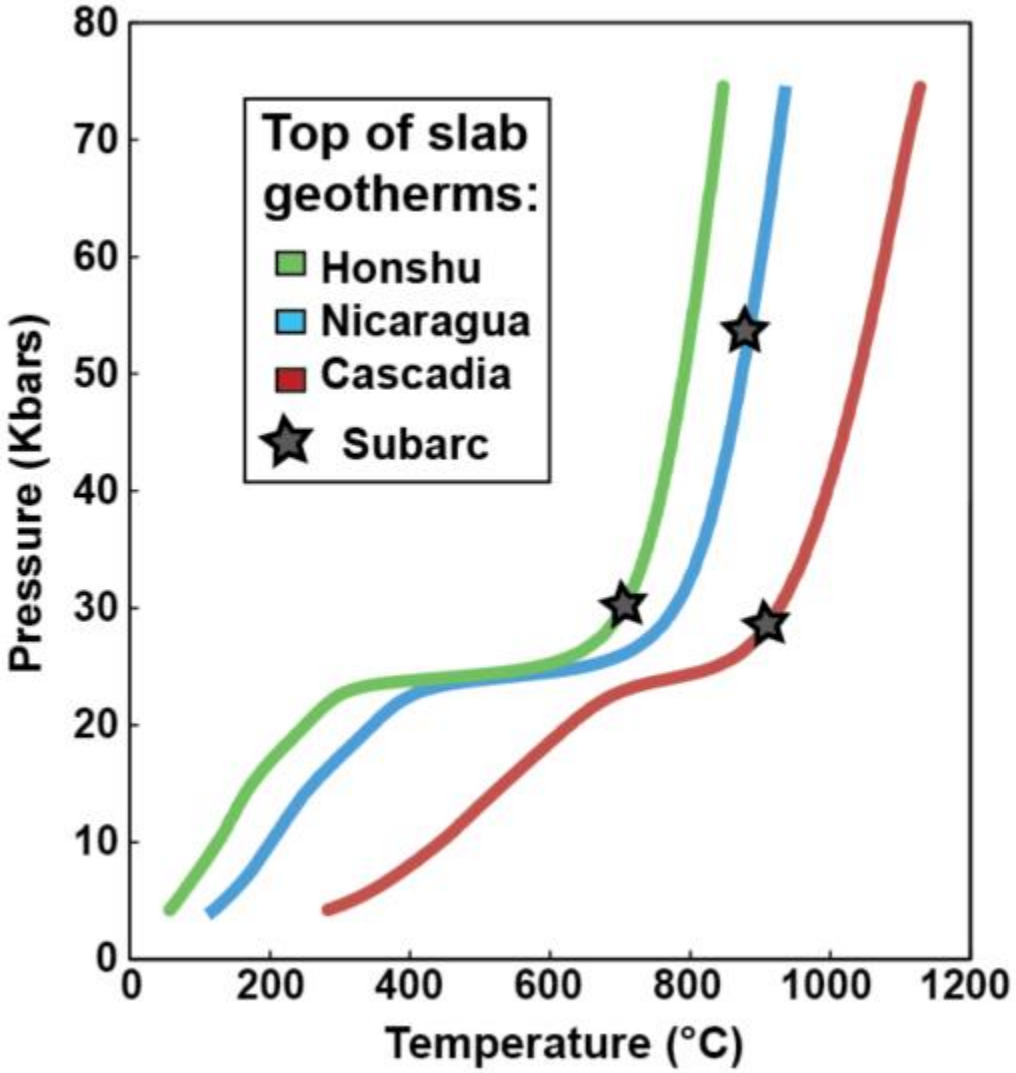

Figure 2.2: Subduction zone pressure-temperature (*P*-*T*) paths represent top-of-slab geotherms for end member subduction zones; Honshu (cold temperature), Nicaragua (medium temperature), and Cascadia (hot temperature). Paths calculated by Syracuse et al., (2010) and modified by van Kecken et al., (2011). The grey stars represent the *P*-*T* conditions directly below the subarc (geometrically constrained by Syracuse et al., 2010) at the top of the subducting slab.

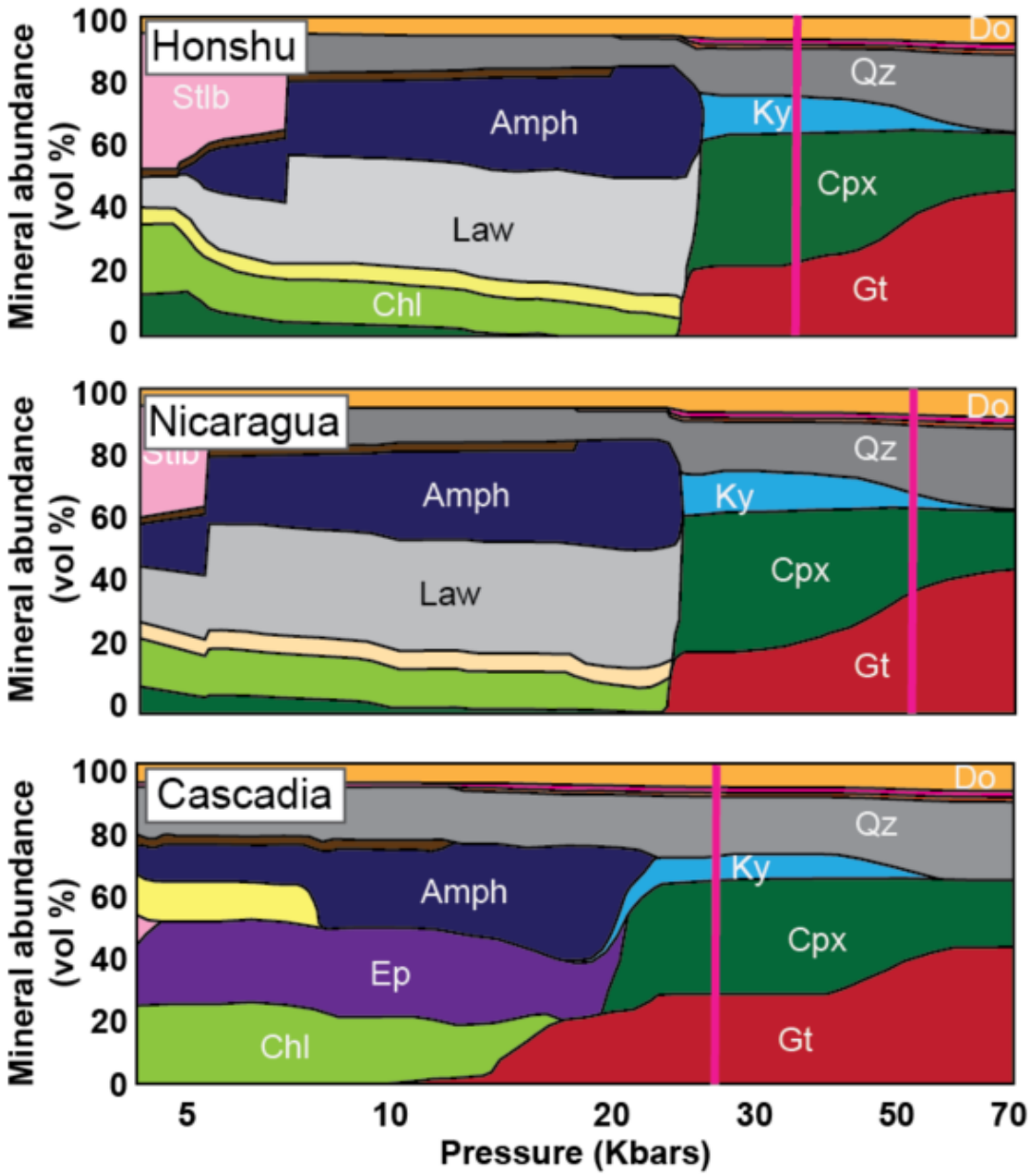

Figure 2.3: Stable mineral phases and their relative proportions (vol %) for a hydrated MORB along a cold (Honshu), medium temperature (Nicaragua), and hot (Cascadia) subduction geotherm. The pink, vertical line represents the *P-T* conditions of the top of the subducting slab below the subarc.

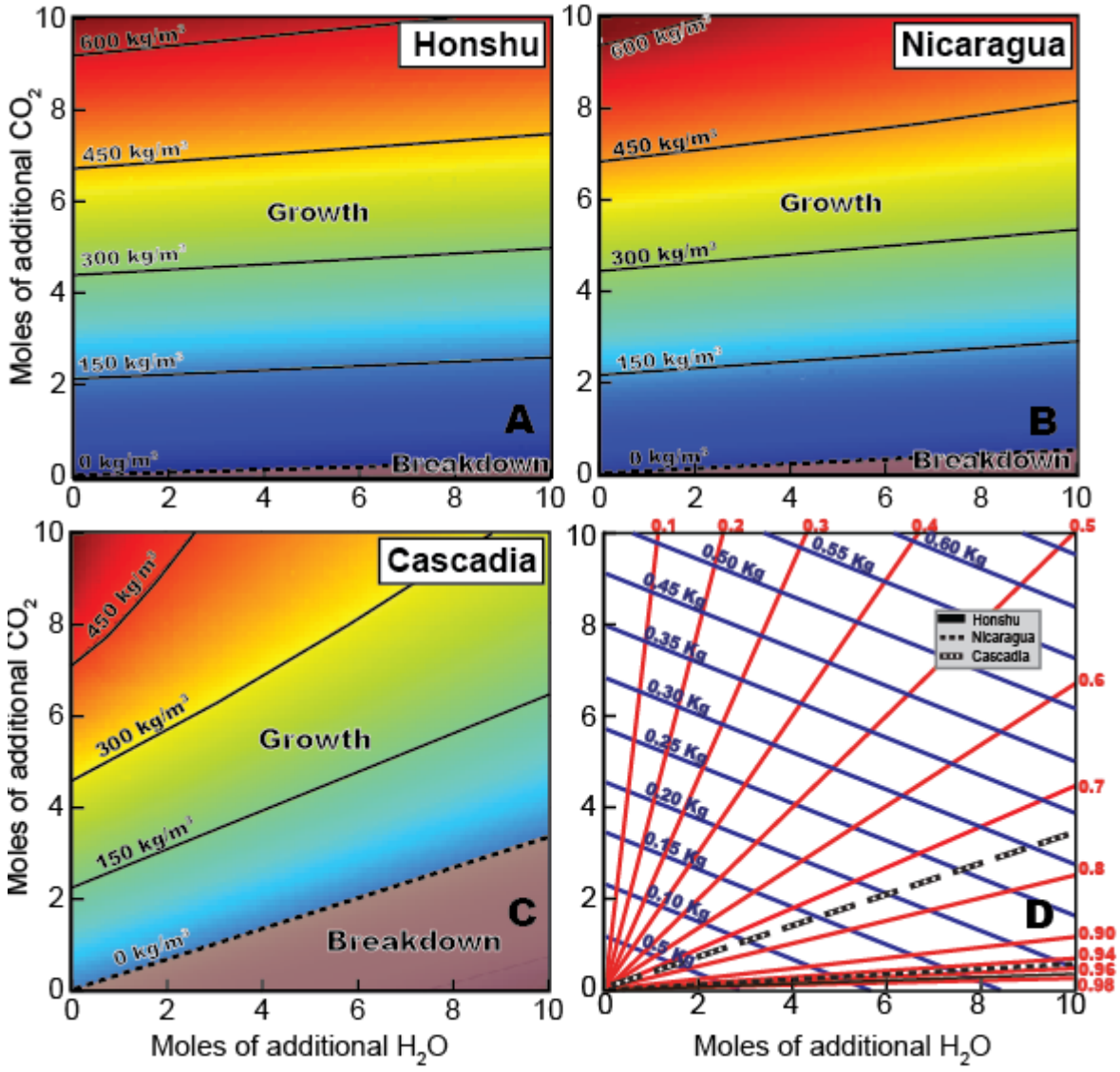

Figure 2.4: System response to external H_2O-CO_2 fluids at the subarc depths for three endmember subduction geotherms: (A) cold (Honshu), (B) medium temperature (Nicaragua), and (C) hot (Cascadia). Contours predict the Δkg of carbonate minerals/1 m^3 of hydrated MORB with respect to the dehydrated MORB composition calculated from figure 2.3. The black, dashed line represents where Δkg of carbonate minerals = 0. Above this line, carbonate minerals grow and below this line, carbonate minerals breakdown. Panel D superimposes contours of fluid composition (Red) and fluid amount (Blue) to predict the composition and amount of fluid needed to decrease the amount of carbonate minerals present in basalt at subarc depths.

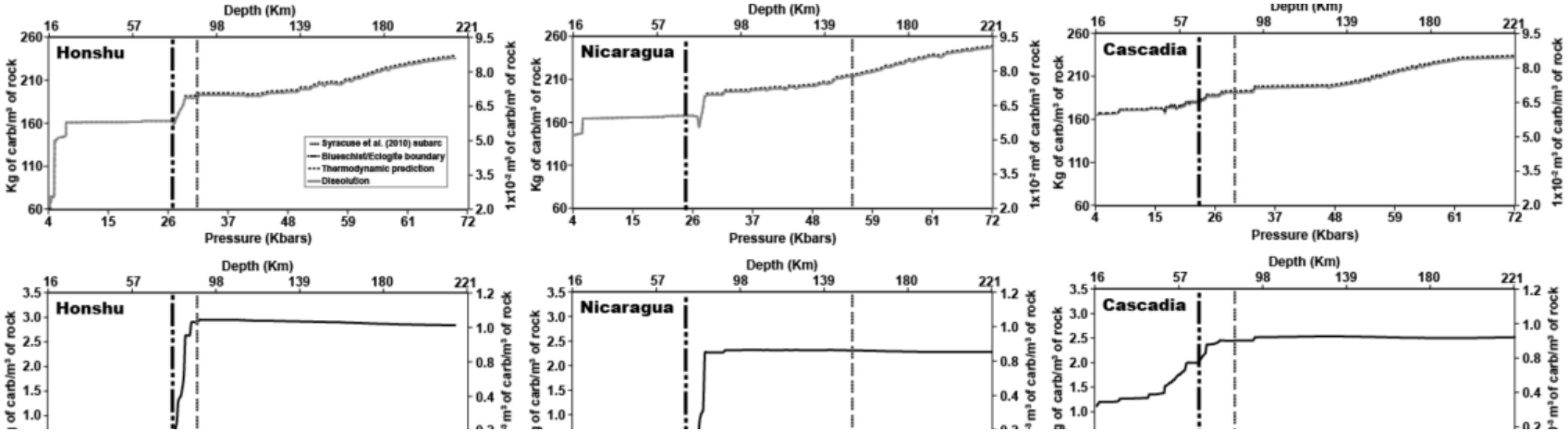

Figure 2.5: Top row: Kg of calcite predicted to be stable in $1m^3$ of subducted, hydrated basalt along cold (Honshu), medium temperature (Nicaragua), and hot (Cascadia) subduction geotherms. Black dashed lines represent Kg calcite/m^3 assuming thermodynamic phase equilibrium. Grey lines represent Kg of calcite/m^3 if we assume that calcite dissolution occurs during the production of internally derived fluids. Bottom row: Maximum amount of kg of calcite/m^3 dissolved into internal fluids, determined by calculating the difference in the amount kg of calcite/m^3 when assuming thermodynamic equilibrium versus the amount of kg of calcite/m^3 when assuming that internal fluids facilitate calcite dissolution. For all figures, the vertical black dashed line represents *P-T* conditions in which blueschist transitions to eclogite. The vertical grey dashed line represents the *P-T* conditions of the top of the slab at the subarc, as calculated by Syracuse et al., (2010).

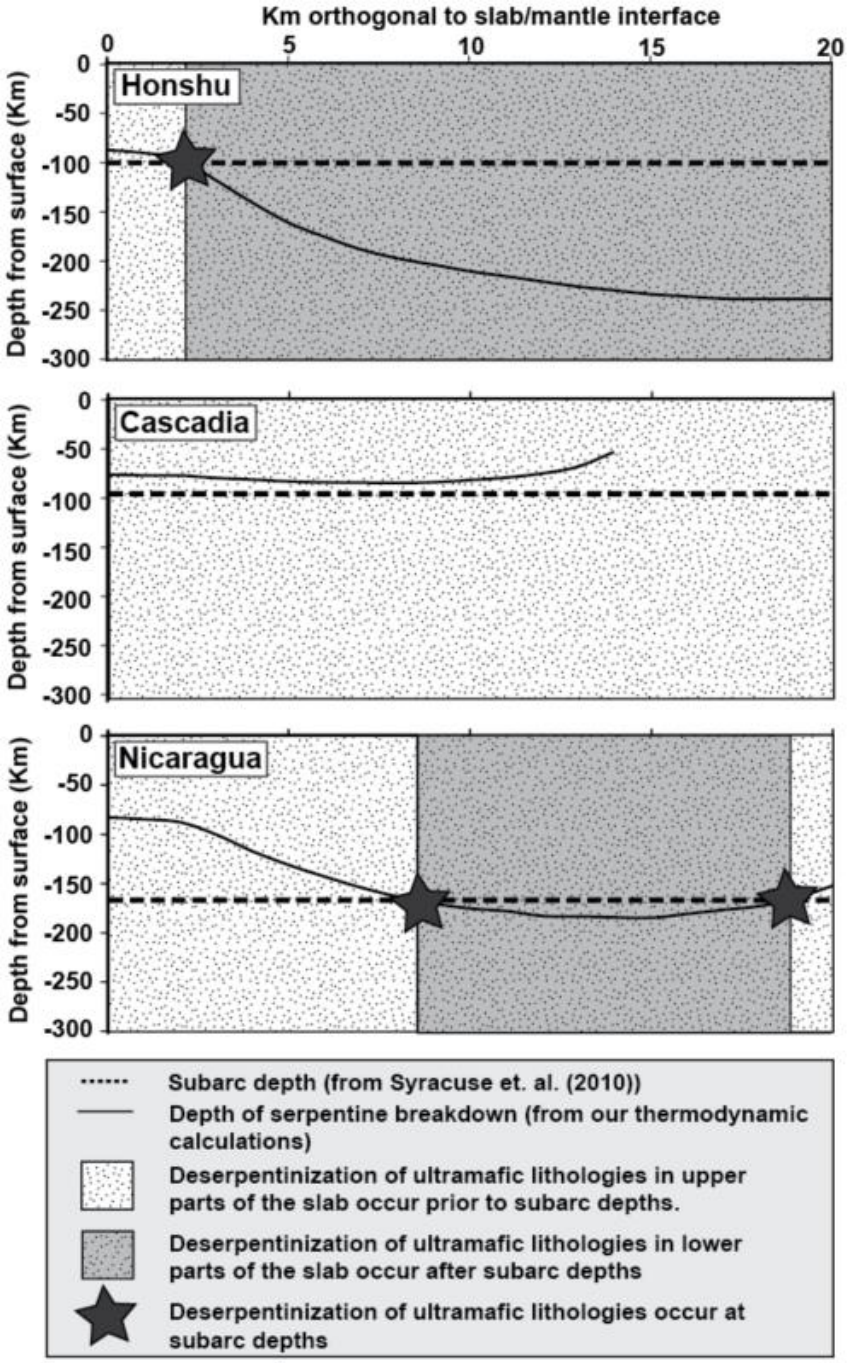

Figure 2.6: Depth of serpentine breakdown as a function of orthogonal distance from the top of the down going slab (solid line) for hot (Cascadia), medium temperature (Nicaragua), and cold (Honshu) subduction zones. The subarc depth as determined by Syracuse et al., (2010) is super imposed on the depth of serpentine breakdown (dashed line). The dark grey boxes represents the range of in-slab depths in which fluid produced by serpentine breakdown can rise and interacted with overlying basaltic lithologies.

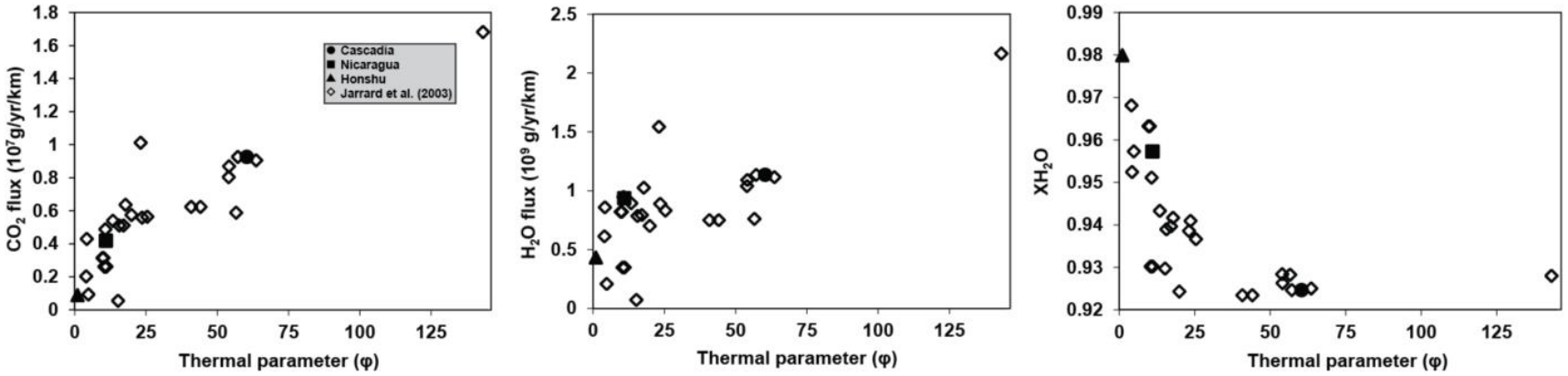

Figure 2.7: Volatile fluxes taken from Jarrard et al., (2003) plotted as a function of the thermal parameter calculated in Syracuse et al., (2010). Left: CO_2 flux as a function of thermal parameter. Middle: H_2O flux as a function of thermal parameter. Right: Fluid composition as a function of thermal parameter. In general, colder subduction systems produces more H_2O and CO_2 per km of subduction zone. We suggest that this is because there is more fluid available in colder subduction due to the serpentine breakdown reaction being extended to greater depths.

2.9 TABLES

Component	Hydrated MORB	Hydrated Harzburgite
SiO_2	50.51	40.68
TiO_2	1.39	
Al_2O_3	15.7	2.86
MnO	0.16	
MgO	7.94	33.2
CaO	11.58	2.05
FeO	7.946	3.43
Fe_2O_3	1.682	4.69
Na_2O	1.39	
K_2O	0.16	
H_2O	15	10.88
CO_2	2.8	

Table 2.1: Bulk rock composition used in thermodynamic modeling.

Mineral	Solution model	Source
Cpx	Omph(GHP2)	Green et al (2007), Diener & Powell's (2011)
Opx	Opx(HP)	Holland and Powell (1998)
Epidote	Ep(HP)	Holland and Powell (1998)
Garnet	Gt(WPPH)	White et al (2005)
feldspar	feldspar	fuhrman (1988)
Chlorite	Chl(HP)	Holland and Powell (1998)
Chloritoid	Ctd(HP)	Holland and Powell (1998)
Titanite	Sp(WPC)	White et al (2002)
Olivine	O(HP)	Holland and Powell (1998)
Antigorite	Atg(PN)	Padrón-Navarta et al (2013)
Brucite	B	
Amphibole	cAmph(DP2)	Deiner et al (2011)
Ilmenite	IlGkPy	
Mica	Mica(CHA)	Coggon & Holland (2002), Auzanneau et at (2010)
Biotite	Bio(HP)	Holland and Powell (1998)
Carbonate	M(HP), oCcM(HP)	Holland and Powell (1998)
Fluid	F	Holland and Powell (1991)

Table 2.2: Mineral solution models used in thermodynamic modeling.

Subduction zone	Arc length (km)	Convergence velocity (km/Ma)	Slab descent velocity (km/Ma)	Km^3 of rock/yr	Maximum Δkm carb/m^3	Maximum CO_2 flux 10^9 g/yr/km	CO_2 flux (10^9 g/yr/km)*	Δkg carb/m^3 needed
Honshu	1061	82.7	46.3	0.70	23	7745	217	0.65
Nicaragua	1506	71.1	62.8	1.00	38	18141	254	0.53
Cascadia	990	30.0	14.2	0.23	196	21473	77.3	0.7

*Values taken from Jarrard et. al. (2003)

Table 2.3: Parameters used to calculate extent of decarbonation required to match measured global values.

Chapter 3

Insights into Early Exhumation of the Cycladic Blueschist Unit Using Thermodynamic Modeling, Inclusion Barometry, and $^{147}Sm/^{144}Nd$ Geochronology

Jennifer Gorce[1], Mark Caddick[1], Ethan Baxter[2], Besim Dragovic[1], Robert Bodnar[1]

1. Department of Geoscience, Virginia Tech, Blacksburg, Virginia, 24060, USA

2. Department of Earth and Environmental Science, Boston College, Chestnut Hill, MA, 02467

This article will be submitted to Earth and Planetary Science Letters for publication

3.1 ABSTRACT:

Well constrained Pressure-Temperature-time (*P-T-t*) paths provide us with valuable insight into subduction zone processes such elemental cycles and mass transport of materials. We focus on a sample from Syros, Greece which preserves high pressure metamorphic mineral assemblages in the Cycladic Blueschist Unit, thus preserving information regarding the slab/mantle interface and exhumation of subducted terrains.

Garnet crystals that exhibit oscillatory chemical zoning are appropriate for thermodynamic modeling, $^{147}Sm/^{144}Nd$ garnet geochronology, and quartz-in-garnet geobarometry, allowing us to constrain the *P-T-t* history of Syros. Garnet grew over a period of 4.31±2.68My, from 45.71±0.98Ma to 41.4±1.7Ma. Thermodynamic modeling suggests that garnet grew from 485˚C and 2.2 GPa to 530˚C and 2.0 GPa, followed by a second stage of growth at 2.1 GPa and 560˚C, to 1.6 GPa and 500^{o}C. These results yield exhumation rates of 0.4-1.7 cm/yr, which we interpret to mean that the Cycladic Blueschist Unit experienced eclogite and blueschist facies metamorphism during synorogenic exhumation due to slab rollback during formation of the Hellenides.

We also compare the results of quartz-in-garnet geobarometry with thermodynamic modeling. Quartz-in-garnet geobarometry suggests that garnet grew isobarically over the 4.31My time interval which is in disagreement with thermodynamic modeling. To address the discrepancy between methodologies, we explore equilibrium assumptions made in thermodynamic modeling and assumptions made regarding the mechanical properties of host and inclusion phases in quartz-in-garnet geobarometry. We observe that the proximity of inclusions to each other can result in an underestimate of entrapment pressure that, in some cases, can be corrected for, yielding pressures that are in better agreement with thermodynamic modeling. We propose that the two datasets complement each other well if we take into careful consideration the assumptions associate with each method.

Key Words: Subduction, Exhumation, barometry, thermodynamics

3.2 INTRODUCTION

Subduction zones are the only geological environment in which material from the Earth's exterior is transported into the deep earth, and thus the processes that occur along subduction zones have important implications for large-scale geologic processes like elemental cycles and mass transport of materials as well as subduction zone geodynamics. Understanding subduction zone tectonics is critical to our understanding of phenomena such as slab metamorphism, volatile release, mantle wedge dynamics, metasomatism, and exhumation of high pressure terrains.

As rocks are buried and heated, prograde dehydration reactions result in the densification of the down going slab and leads to the formation of eclogite (Peacock, 1993). Eclogite has a density greater than that of the surrounding upper mantle, providing a proposed driving mechanism for slab-pull (Spence, 1987, Schellart, 2004). This material can reach the base of the lower mantle

and is postulated to be the source of continental geochemical signatures seen in hotspot volcanism (Torsvik et al., 2008, Zhao 2004). The negative buoyancy of eclogite implies that subduction is a one way process, and yet High Pressure/Low Temperature (HP/LT) metamorphic terrains are found worldwide and the mechanism for their exhumation is hotly discussed in the geological community.

A common method for determining exhumation mechanisms is the construction of Pressure-Temperature-time (*P-T-t*) paths. Path geometry coupled with heating, burial, and exhumation rates can be diagnostic of different tectonic mechanisms (e. g. Maruyama et al., 1996). In the past decade, techniques for determining the *P-T-t* histories of metamorphic rocks have become increasingly sophisticated and include a wide range of mineral barometers, thermometers and chronometers. This study constructs a *P-T-t* path on a single sample by integrates modern geothermobarometry and geochronology techniques in order to better constrain the metamorphic and tectonic evolution of the Cycladic Blueschist Unit.

Geothermobarometry of subduction zone rocks can be determined via several methodologies. Numerous studies (e.g. Trotet et al., 2001; Dragovic et al., 2012; Dragovic et al., 2015) conduct forward modeling by combine thermodynamic modeling with quantitative microprobe analyses of metamorphic assemblages to calculate the pressure and temperature at which the measured composition of a solid solution mineral phase is the most stable (lowest Gibbs free energy)(Connolly, 2005). Another method utilizes the contrasting mechanical properties of minerals in inclusion-host pairs to determine entrapment pressures. Lastly, petrologists use inverse modeling to infer *P-T* conditions by using the pressure and/or temperature dependent partitioning of elements between mineral phases to construct Pressure-Temperature histories. In this study, we examine the results of thermodynamic models and quartz-in-garnet barometry, address the merits and pitfalls of both techniques, and attempt to reconcile the datasets.

Chronometers used in the study of subduction metamorphism include $^{40}Ar/^{39}Ar$ in white mica (e.g. Grimmer et al., 2003; Putlitz et al., 2005; etc), $^{238}U/^{206}Pb$ zircon (Chiu et al., 2013), $^{176}Lu/^{176}Hf$ in garnet (Lagos et al., 2003), and $^{147}Sm/^{144}Nd$ in garnet (Dragovic et al., 2012; Dragovic et al., 2015). For each chronometer, we must consider closure temperature, degree of isotopic fractionation, and precision of the analytical technique used to measure isotope ratios because these factors affect the precision of the resultant age. For the purpose of this study, we use $^{147}Sm/^{144}Nd$ garnet geochronology because it offers high precision results (<1 My errors), has a

closure temperature well above the average blueschist/eclogite facies (about 750˚C, dependent on metamorphic duration) and distribution of Samarium through garnet crystals is often relatively homogenous (e.g. Baxter et al., 2013) which allows us to unndertake detailed, zoned geochronology on a single crystal and yield a rate of growth, which can be linked to processes such as exhumation.

This paper focuses on a sample from the southwestern part of the island that contains chemically zoned garnet crystals that are appropriate for thermodynamic modeling, $^{147}Sm/^{144}Nd$ garnet geochronology, and quartz-in-garnet geobarometry, not only allowing us to constrain the *P-T-t* history of Syros, but examine how different methodologies for determining *P-T-t* paths complement each other.

3.3 GEOLOGIC SETTING

3.3.1 The Hellenic Subduction Zone

The modern Hellenic subduction zone is located in the Aegean Sea south of Crete and results from the subduction of the African plate beneath the Aegean plate (Figure 3.1a). The resulting orogenic belt, the Hellenides is comprised of several distinctive tectonic subunits that were progressively subducted 145–50 Ma (Lips et al., 1999, Sherlock et al., 1999, Mposkos & Kostopoulos 2001, Krohe & Mposkos 2002, Ring & Layer 2003, von Quadt et al., 2005). Most workers agree that at least three oceanic domains were subducted over the course of 80 Mya: The Vardar-Izmir Oceanic Unit, the Pindos Oceanic Unit, and East Mediterranean Ocean.

In this study we examine a sample from the Pindos Oceanic Unit, which is a heterogeneous domain of continental and oceanic sequences, including the Selcuk Melange in the upper part of the unit and the Cycladic Blueschist Unit (CBU) in the lower part (Okrusch & Brocker 1990). The CBU is interpreted to be the most deeply exhumed part of the Hellenides, reaching eclogite facies conditions and is comprised of carboniferous schists and orthogneisses as well as carboniferous marbles, metapelites, and metavolcanics (Durr et al., 1978; Ring and Layer 2003; Ring et al., 2010). Well preserved remnants of the CBU can be found on the island of Syros (Figure 3.1) and the study of the CBU provides insights into deep (>60km) subduction zone processes. On Syros, Greece, the CBU is interpreted to be a series of stacked tectonic nappes, with higher metamorphic grade material being thrust onto lower grade material (Trotet et al., 2001).

3.3.2 Metamorphic Overview of the Cycladic Blueschist Unit

Most lithologies on Syros experienced prograde dehydration and were variably rehydrated during exhumation, with previous work yielding a range of pressures (1.7-2.1GPa) and temperatures (500-550˚C) for peak metamorphism (e.g. Dixon 1976; Lister and Raouzaios 1996, Trotet et al., 2001b, Keiter et al., 2004, Schumacher et al., 2008, Ring et al., 2010, Phillipon et al., 2013). The protolith age of the original oceanic crust is constrained by U-Pb zircon geochronology at 80-75 Ma by Keay (1998) and Lu-Hf zircon geochronology at 80±12.4-13.8Ma (Tomaschek et al., 2003). Trace element contents suggest that the protolith was a ferrogabbroic or a strongly differentiated basalt that crystallized in a small scale magma chamber (Brockers and Enders 2001).

3.4 SAMPLE DESCRIPTION

14HSY-35E is a garnet-bearing quartz mica schist. Phases include quartz, mica, amphibole, garnet, clinopyroxene, carbonate, epidote, and titanite. Quartz exists as inclusions in garnet, in the primary matrix, and as recrystallized quartz in pressure shadows around garnet Quartz in the matrix contains small (approximately 10um) inclusion of clinopyroxene. Mica can be divided into two distinct populations. 1.) Small, anhedral phengite that defines a foliation fabric that we interpret to grow during prograde metamorphism. 2.) Larger, euhedral paragonite grains that overgrow the primary foliation that we interpret to grow at the same time as glaucophane. Large (4-5mm length) needles of glaucophane overgrow the primary foliation fabric but define a lineation that is sub-parallel to the original foliation.

Glaucophane contains inclusions of quartz and epidote and shows evidence for brittle deformation (Figure 3.2). Garnet crystals (5-7mm) preserve two phases of growth that are recorded texturally and compositionally. The cores of the garnets are heavily included in quartz, rutile, and epidote while the rims are nearly free of inclusions. Microprobe transects were taken across individual garnets and compositional profiles for the mole fraction almandine, spessartine, grossular, and pyrope were constructed (Figure 3.2).The boundary between the inclusion rich cores and inclusion free rims is further demarcated by a step-wise uptake in spessartine content. Omphacite exists as small (10-15um) inclusions in quartz and garnet Calcite is post-metamorphic and overgrows glaucophane needles.

3.5 METHODS

Mineral compositions were acquired via microprobe analysis using a Camera SX-50 microprobe with the beam set at 20nA and an acceleration voltage of 15kV. See Table 3.1 for average mineral composition of each phase.

3.5.1 *P-T* modeling

Isochemical phase diagrams (Figure 3.3) were constructed using X-Ray Fluorescence (XRF) bulk rock data to calculate equilibrium pressure-temperature (*P-T*) conditions of garnet growth and thus predicted peak *P-T* conditions of metamorphism. XRF bulk rock analyses (Table 3.2) were done at Franklin and Marshall College by Stan Mertzman and associates. Fe^{3+}/Fe^{2+} was determined via titration. A combination of point counting and mineral analyses via electron microprobe yield similar bulk rock chemistries to that of XRF(Table 3.2).

The composition of garnet is sensitive to pressure and temperature (Hollister, 1966), and thus the mole fraction of major cations (Fe, Ca, Mg, Mn) and can be used to constrain the *P-T* conditions of garnet growth (e.g. Gaidies et al., 2008; Tirone and Ganguly, 2010; Dragovic et al., 2012; Qian and Wei, 2016) which can be used as a proxy for dehydration during subduction (Baxter and Caddick, 2013) and peak metamorphism. By using a Gibbs free energy minimization approach (e.g. Connolly, 2005), we calculate the predicted composition of garnet over a range of *P-T* conditions for a given a bulk rock composition. The intersection of lines of equal composition (isopleths) for the measured X_{Mn}, X_{Mg}, X_{Ca}, and X_{Fe} in garnet represent the *P-T* condition in which garnet is in thermodynamic equilibrium with the bulk rock composition.

Phase equilibria calculations used the Holland and Powell (1998) data set and the thermodynamic modeling software package, Perple_X. Solution models for complex phases are listed in table 3.3 in appendix A. Modeling was done in the chemical system K_2O-MnO-MgO-CaO-Al_2O_3-FeO-Fe_2O_3-SiO_2-Na_2O-TiO_2. The sample is assumed to be saturated by an H_2O-CO_2 fluid, whose behavior is described by a Compensated Redlich-Kwong (CORK) equation of state (Holland and Powell, 1991).

As garnet grows, it sequesters elements which are no longer available to the system causing the reactive bulk rock composition to change as garnet grows. To account for this phenomenon, the volumetric contribution of pre-existing garnet was removed from the bulk rock composition

(reactive bulk rock composition) before generating isopleths. (See Baxter and Caddick (2013) for additional details). We construct four phase diagrams that are associated with different parts of the garnet crystal and thus different chemical domains and *P-T* conditions (Figure 3.3); 1.) The garnet core (C1), which is in equilibrium with the XRF bulk rock composition, 2.) The edge of the first period of garnet growth (R1), which is in equilibrium with a reactive bulk rock composition in which 49 vol % of garnet is remove from the XRF composition, 3.) The beginning of the second period of garnet growth (C2), which is in equilibrium with a reactive bulk rock composition in which 51 vol% of the total garnet has been removed, and 4.) The edge of the garnet crystal (R2), which is in equilibrium with a reactive bulk rock composition in which 99 vol % of the garnet has been removed. To determine the appropriate reactive bulk rock composition at each garnet growth stage, a volumetrically weighted, compositional average is calculated (using the results from microprobe analyses) for each volume of garnet removed from the XRF bulk rock composition. A summary of reactive bulk rock compositions can be found in table 3.2 and a summary of values used for garnet compositions at each point of interest can be found in table 3.4.

3.5.2 Quartz-in-Garnet Geobarometry

We use quartz-in-garnet barometry to determine the entrapment pressure of quartz during garnet overgrowth in order to test assumptions made during thermodynamic phase equilibria modeling. Because peak positions of α-quartz vary with pressure and temperature (Schmidt and Ziemann, 2000), and host minerals such as garnet are rigid enough to maintain confining pressures at standard atmospheric conditions (Enami et al., 2007) previous workers (e.g. Ashley et al., 2014; Kohn, 2014; Spear et al., 2014) have used the magnitude of change in the 464cm^{-1} Raman peak to determine confining pressures of quartz in garnet, and using Equations of State (EoS), calculate entrapment pressures.

To determine the confining pressure on quartz inclusions in garnet, we measure the shifts in quartz Raman spectra with a JY Horiba LabRam HR800 microprobe in the Department of Geosciences at Virginia Tech. Quartz inclusions from three garnets in one thick section (60um) are analyzed (Figure 3.6). Inclusions are selected based on size (10-20um), proximity to fractures, thick section surfaces and other inclusions, and distribution in garnet. The goal is to have a large sampling from garnet core to rim, in order to develop a pressure profile during garnet growth.

We determine inclusion confining pressures using methods described in Ashley et al., (2014) and Kohn (2014) (Table 3.5). However, results between Ashley et al., (2014) and Kohn (2014) overlap within uncertainty (Figure 8) so we chose to use inclusion pressures calculated via Kohn (2014) for subsequent calculations using an equation from Kohn (2014) that used data from experiments done by Schmidt and Ziemann (2000), listed below:

$$P_{inclusion}(bar) = 1118.0 \pm 7.0 \Delta\nu 464 + 0.168 \pm 0.029 (\Delta\nu 464)^3$$

The choice to use the shift in the 464cm^{-1} instead of the 206cm^{-1} peaks is because garnet spectra can overlap with the 206cm^{-1} spectra (Enami, 2012; Kohn, 2014). A summary of inclusion pressures can be found in table 3.7.

Entrapment pressures are calculated via two methodologies; 1.) The software package EosFit-Pinc (Angel et al., 2017), which is an add-on for the EosFit7 software package (Angel et al., 2014) uses a *P-V-T* Equation of State (EoS) for almandine (Milani et al., 2015) and, a *P-V-T* EoS from Angel et al., (2017) for quartz that includes the elastic softening in both alpha and beta quartz and a curved alpha-beta phase boundary to determine elastic properties. 2.) Methods describe in Ashley et al., (2014) that used EoS from the 2011 update of the Holland and Powell (1998) thermodynamic dataset.

Entrapment temperature is determined by calculating the temperature at which the measured composition of garnet is thermodynamically stable in a given bulk rock composition using the thermodynamic modeling software package, Perple_X. For the first stage of garnet growth (C1-R1) we calculate that temperature increases from 485˚C to 530˚C. We calculate that temperature decreases from 560˚C to 500˚C during the second stage of garnet growth (C2-R2).

3.5.3 ^{147}Sm/^{144}Nd Garnet Geochronology

Garnet heavily favors samarium over neodymium during growth and thus produces high parent/daughter ratios in the ^{147}Sm/^{144}Nd radiogenic system (Van Breemen and Hawkesworth 1980; Griffin and Brueckner 1980). That, coupled with garnet's ubiquity over a broad range of lithological compositions, makes ^{147}Sm/^{144}Nd garnet geochronology an ideal candidate for dating metamorphic events in many geologic environments (Baxter and Scherer, 2013). Garnet geochronology uses the isochron method, in which ^{147}Sm/^{144}Nd and ^{143}Nd/^{144}Nd isotope ratios

from garnet and another source, such as the rock matrix, are plotted along a straight line, whose slope is proportional to age (e.g. Pollington and Baxter 2010; Pollington and Baxter 2011; Dragovic et al., 2012; Dragovic et al., 2015). Because garnet is compositionally zoned, studies have dated cores and rims of garnets in order to constrain rates of growth and thus the rates of metamorphic processes (e.g. Christensen et al., 1989; Vance and O'Nions, 1990; Burton and O'Nions, 1991; Vance and Harris, 1999; Baxter et al., 2002;). In more recent studies (Pollington and Baxter, 2010; Pollington and Baxter, 2011; Dragovic et al., 2012; Dragovic et al., 2015) high-precision microsampling of garnet zones has been used to elucidate details of rapid metamorphism over deep time.

Garnets were plucked whole from a rough crush (0.5-1 cm) of bulk rock and were selected based on size (only crystals >5mm in diameter were used). Garnets were mounted on an aluminum plate and cut with a diamond microsaw to produce 2mm thick garnet wafers. Twenty-one garnet wafers were micro-drilled into core and rim domains using methods described in Pollington and Baxter (2011). Cores and rims were determined optically because the rim is noticeably paler and more orange than the core of the garnet Rims are approximately 0.5mm thick. Lines for drilling were placed about 400um from the core/rim boundary to account for the sample lost from the drill trench. All samples (cores, rim, bulk rock, matrix), were crushed to a specific size (100-200 mesh). Crushed garnet was passed through a magnetic resonator and manually hand plucked in an initial attempt at removing inclusions from the garnet.

Once crushed to a particular grain size, inclusion phases in garnet were removed using partial dissolution techniques modified from Dragovic et al., (2015). Several fine powders from garnet were also treated to preferentially remove inclusion phases. All samples, including treated and untreated garnet crushes and powders, as well as rock powders, were fully dissolved in solution. Samarium and Neodymium were extracted from solution using a 3-column chromatography procedure from Harvey and Baxter (2009). Three column blanks were ran in tandem with samples. All samples were treated with $^{147}Sm/^{144}Nd$ spike prior to loading the final set of columns. Analysis of Sm and Nd isotopes was done at Boston College using an IsotopX Phoenix X62 TIMS using sample preparation and data reduction methods by Harvey and Baxter (2009).

3.6 RESULTS

3.6.1 *P-T* Modeling

Figure 3.4 illustrates a *P-T-t* path over which garnet grew during subduction and exhumation of the CBU. Garnet is calculated to begin growing (C1) in the presence of glaucophane, dolomite, lawsonite, omphacite, quartz, white mica and rutile (Figure 3.4a) at approximately 485˚C and 2.2 GPa. This is consistent with inclusion assemblages observed in garnet porphyroblasts, with the exception of observed epidote, which we suggest is a product of lawsonite breakdown during decompression. Garnet is inferred to continue to grow during decompression and heating, until it reaches approximately 530˚C and 2.0 GPa (R1). At this point, glaucophane breaks down, resulting in a fluid loss of approximately 0.5 wt % H_2O, assuming that the sample was fluid saturated during garnet growth (Figure 3.5). Garnet growth ceases temporarily but begins again at approximately 2.1 GPa and 560˚C (C2) in the presence of paragonite, dolomite, omphacite, rutile, and quartz. Because the garnet rims are sparse in inclusions, we can only confirm that quartz was stable during garnet rim growth. We hypothesize that the initiation of a second phase of garnet growth is due to the reburial of 14HSY-35E (Figure 5, R1 to C2). The final rim of garnet grew at the expense of glaucophane and lawsonite during exhumation to approximately 1.6 GPa and 500˚C. We propose that the breakdown of lawsonite during decompression is the primary driver for dehydration and subsequent garnet growth during exhumation. *P-T* conditions are broadly in agreement with work done by Kendall et al., (2016) as well as fit in the range of *P-T* conditions offered by past workers (e.g. Trotet et al., 2001, Schumacher et al., 2008).

The results from thermodynamic modeling are contingent on the fact that we assume that the rock is able to reach thermodynamic equilibrium along its *P-T* path and that open-system behavior is not experienced. To test this assumption, we calculate the predicted mineral evolution at one degree Celsius increments along our constructed *P-T* path (Figure 5) for a starting bulk rock composition of 14HSY-35E. We fractionate garnet and fluid as it is produced (See Baxter and Caddick, 2013) and reintegrate garnet back into the bulk mineralogy at the end of the calculation because we assume that any fluid or garnet produced during prograde metamorphism of the subducting slab is removed from the effective bulk rock composition and is unavailable for subsequent calculations. We compare the final calculated proportions of minerals in the rock with observations across a thin section. Modeling results predict that garnet will grow from 485˚C and

2.2 GPa to 530˚C and 2.0 GPa (C1-R1) and from 2.1 GPa and 560˚C to 1.6 GPa and 500˚C (C2-R2). For most phases, model and observations are within 1-2 wt% of each other. The major discrepancies, primarily the model's over estimation of epidote and mica, the underestimation of dolomite, can be explained by textures seen in thin section (Figure 3.2). We see breakdown of epidote and late stage growth of dolomite (fig. 3.2F). We also see Na-rich mica overgrowing the primary foliation of 14HSY-35E (Figure 3.2D). While glaucophane overgrows high pressure minerals such as omphacite (Figure 3.2B), there is also evidence of dolomite growing at the expense of amphibole (Figure 3.2E), implying that this sample was exposed to carbonaceous fluids late in its history. This observation is in agree with other works (e.g Ague and Nicolescu, 2014), which quantify late stage carbonation of CBU lithologies. Given the good agreement between calculated mineral evolution and thin section observations, we suggest that our equilibrium assumptions are appropriate for 14HSY-35E. We continue to test these assumptions in section 3.6.2, with inclusion-host barometry.

3.6.2 Quartz-in-Garnet Geobarometry (QIGG)

For three selected garnet crystals, entrapment pressures range from 1.3 GPa to 1.6 GPa using methods from Ashley et al., (2014), with most analyses at approximately 1.5 GPa (Figure 3.7). When using EosFit-Pinc, entrapment pressures range from 0.7-2.1 GPa with most analyses between 1.7 GPa and 1.9 GPa. Despite the wider spread in the data when using EosFit-Pinc, both data reduction methodologies predict isobaric garnet growth, as there is no systematic difference between the entrapment pressures calculated from garnet core to rim. A compilation of entrapment pressures from both techniques and entrapment temperatures is included in table 3.7.

Results differ between EosFit-Pinc and Ashley et al., (2014) for several reasons. The most obvious and striking are the EoS models used for the host and inclusion phases in both calculations. Angel et al., (2017) uses a more complex EoS for quartz which takes into account elastic relaxation and a curved alpha-beta quartz transition. EosFit-Pinc results are also more sensitive to entrapment temperature conditions, which could explain the wider spread in entrapment pressures.

3.6.3 $^{147}Sm/^{144}Nd$ Garnet Geochronology

Ages calculated for garnet core and rim are 45.71±0.98Ma with an MSWD = 1.8 and 41.4±1.7Ma (MSWD =1.4), respectively (Figure 3.8). The magnitude and precision of Nd concentration,

$^{147}Sm/^{144}Nd$ value, and $^{143}Nd/^{144}Nd$ value is influenced by our ability to clean the garnet of HREE bearing inclusion phases during partial dissolution, accidental incorporation of matrix material during cleaning and separation, and sample size and subsequent signal intensity during TIMs analysis. In general., samples that were cleaned using traditional partial dissolution techniques (See appendix A) had lower $^{147}Sm/^{144}Nd$ values that were partially dissolved by alternating small quantities of HF with HNO_3 over 8-12hrs(See Table 3.9) We attribute this to the fact that the use of excess HF and the use of elbow stills during evaporation of $HClO_4$ caused the re-precipitation of SiO_2 onto the crushed sample, effectively shielding it from additional acid washes.

The 7-point isochron (Figure 3.8) generated for the garnet core population includes $^{147}Sm/^{144}Nd$ and $^{143}Nd/^{144}Nd$ values from the bulk rock, several garnet core crushes, and several garnet core fine powders. The isochron generated for the age of the garnet rim population of is a 5-point isocron consisting of $^{147}Sm/^{144}Nd$ and $^{143}Nd/^{144}Nd$ values from the bulk rock matrix (reactive bulk rock composition), garnet rim crushes, and garnet rim fine powders. One point was dismissed from the rim age isochron because the $^{143}Nd/^{144}Nd$ value was more consistent with that of the matrix and bulk rock, implying that material from those domains contaminated that particular sample. For both the core and rim ages, low MSWD (1.8 and 1.4) values imply that it is garnet porphyblasts began growing at the same time and that the practice of amalgamating core and rim populations was appropriate. The first period of garnet growth from the second period of garnet growth is separated by 4.31My, from 45.71±0.98Ma to 41.4±1.7Ma (Figure 3.8). While we cannot constrain whether these growth events happened rapidly (>1my as in Dragovic et al., 2012) or gradually, we propose that the four million year timescale does not support instantaneous mineral growth caused by a buildup of free energy in the system due to overstepping.

3.7 DISCUSSION

3.7.1 Assessing methodologies

3.7.1a Garnet overstepping

Studies (Spear et al., 2014; Spear, 2017; Wolfe et al., 2017) argue that thermodynamic modeling is an inappropriate way in which to determine *P-T* conditions of metamorphic rocks because the assumption of equilibrium being reached during metamorphism is rarely, if ever, attained.

Evidence for disequilibrium can be seen in the compositional zoning of garnet (Carlson et al., 2015) and the fact that there are several reported cases (e.g Dragovic et al., 2012; Hoschek, 2013; Wolfe et al., 2018) in which garnet is predicted to nucleate beyond the *P-T* conditions of the garnet isograd. Most workers (e.g. Spear et al., 2014; Carlson et al., 2015; Spear, 2017; Wolfe et al., 2018) would argue that overstepping is a necessity for garnet growth because the reaction affinity (macroscopic driving force of a reaction) for garnet nucleation is relatively high and thus requires a buildup of energy to overcome kinetic barriers (Carlson et al., 2015; Spear and Patterson, 2017).

Given the above evidence, some studies (e.g. Spear, 2017; Wolfe et al., 2017) might interpret our results from quartz-in-garnet barometry as evidence for isostatic garnet growth, in which the rate of garnet growth is very fast (hundreds of years) and is a function of building up the required energy needed for nucleation during *P-T* overstepping and thus growing the crystal all at once. We propose that given the timescales of garnet growth determined by $^{147}Sm/^{144}Nd$ garnet geochronology (~4Ma), episodic garnet growth is unlikely and thus we need to examine the assumptions of quartz-in-garnet-barometry in more detail.

3.7.1b Assumptions of quartz-in-garnet geobarometry

The success of inclusion-host barometry relies on the assumption that the host phase behaves rigidly, and both inclusion and host phase will relax elastically during decompression. Below, we examine these assumptions in the context of quartz and garnet geobarometry in more detail and the implications if these assumptions do not hold true.

To behave as a rigid body, the host must have a high shear modulus and act as an infinite medium (Zhang, 1998; Enami et al., 2007; Kohn, 2014; Ashley et al., 2014). Though garnet has a high shear modulus, the assumption that it acts as an infinite medium does not always hold true, especially when garnet crystals are heavily included (Figure 3.7). We apply equations from Zhang (1998), and see that the residual pressure of the inclusion decreases substantially if there is less than three times the inclusion radius' length around the inclusion.

Inclusion pressure, for a simple elastic case modified from equation 21 in Zhang, (1998):

$$P_{inc} = \left\{\left[\frac{1}{K_h} - \frac{3}{4G_h}\right] + (1-x)[P_{in,0}\left(\frac{1}{K_i} - \frac{1}{K_h}\right) + (\gamma_i - \gamma_h)]\right\} \times [\frac{1-x}{K_i} + \frac{3}{G_h} + \frac{x}{K_h}]^{-1} \quad (1)$$

Where K_h and K_i are the bulk moduli of the host and inclusion phase, respectively, G_h is the shear modulus of the host, $P_{in,0}$ is the original entrapment pressure in bars, γ_i and γ_h are the product of the thermal expansivity (α) and $\Delta T(K)$ for the inclusion and host phase, respectively and x is the ratio of inclusion volume to host volume (volumetric ratio). We use this equation to see how the residual pressure of the inclusion changes as a function the volumetric ratio (Figure 3.9).

Thermodynamic properties for quartz and almandine garnet were calculated using the program Frendly, which is part of the thermodynamic software package, Perple_X, using thermodynamic data and Equations of State from the Holland and Powell (2011) dataset The entrapment conditions assumed for the following calculations are 500˚C and 2GPa (typical conditions for eclogites).The change in temperature is the difference between the entrapment temperature and standard atmospheric conditions (500˚- 25˚C = 475˚C).

As mentioned earlier, the host phase is considered to be an infinite medium if there is a distance of at least three times the inclusion radius in which the host phase is free of additional inclusions and/or fractures. As the volume of the quartz inclusion increases and the volume of surrounding garnet decreases, the residual pressure of the inclusion decreases, resulting in a predictable underestimation of entrapment pressure (Figure 3.9a). In this study, we measure the radius of quartz inclusions in garnet and the distance of the inclusion to the nearest object in the garnet host (e.g. another inclusion, crack, etc). We assume that the inclusion is spherical, that the volume of the host is equal to the volume of a sphere with a radius equal to the sum of the distance between inclusions and inclusion radius, minus the inclusion volume. We then calculate a volumetric ratio (x) and use Equation 1 to determine by how much the residual pressure of the inclusion is being underestimated. This value is added to the value measured via Raman spectroscopy and then re-entered into Eosfit-Pinc, to calculate entrapment pressure. A summary of original calculated entrapment pressures coupled with entrapment pressures corrected for the proportions of host to inclusion phases can be found in Figure 3.10. For garnet 2 and 3, the magnitude of the pressure correction is greatest in the core of garnets, where inclusion density is higher. Average garnet core pressures (~2.1GPa) and rim pressures (~1.7GPa) are in much better agreement with thermodynamic models, which predict that garnet grew during exhumation.

Though this trend cannot be seen in garnet 1, we see that there is a correlation between inclusion radius and correction magnitude, implying that the size of quartz inclusions influences the measured residual pressure. We also recognize that there are additional factors regarding the

stress effects that inclusions in close proximity exert on neighboring inclusions, and that a more detailed investigation to understand these effects is necessary.

Other inclusions in the garnet might also compromise the ability of garnet to behave as a rigid host. Figure 3.11 illustrates how increasing the vol % epidote (reducing garnet vol%) of the host phase affects inclusion pressure. If a garnet has inclusions of epidote, we can think of the host phase as garnet+epidote, where more epidote would lower both the bulk and shear moduli, reduce the inclusion pressure, and thus underestimate entrapment pressure. If we assume that the host can be approximated to be 95 vol% garnet, and 5 vol% epidote, then, P_{inc} is reduced from 1.19 GPa to 1.17 GPa. Though this change is insignificant, if we consider a case where the host is effectively, 50 vol% garnet and 50 vol% epidote, then P_{inc} is reduced to 1.05GPa. Here, we only consider epidote (Figure 3.11), but if a garnet contains additional inclusions with lower bulk and shear moduli, then the host has even less ability to behave as a rigid body.

Thus, it is likely that P_{inc} measured via quartz in garnet barometry is being underestimated. This could explain why other studies typically see records of isobaric garnet growth when analyzing quartz inclusions. Garnet is typically more heavily included in the core, so garnet is less able to act as an infinite medium that preserves inclusion pressure.

3.7.1c We assume that garnet and quartz will relax elastically during decompression

Quartz-in-garnet barometry assumes that both garnet and quartz relax elastically during decompression and exhumation. However, a recent study by Zhong et al., (2018) found dislocation structures in host phases around inclusions via transmission electron microscopy, and use these observations to suggest visco-elastic or elasto-plastic relaxation of the host phase yields lower entrapment pressures. They proposed that the degree of relaxation is time dependent, and thus the difference between the theoretical entrapment pressures calculated assuming pure elastic relation and the measured entrapment pressure (through an independent barometry) can be used as a chronometer for calculating exhumation rates. Exploring the validity of this chronometer is beyond the scope of this study, but it is interesting to note how our results bear similarity to one of the case studies in Zhong et al., (2018). $^{147}Sm/^{144}Nd$ garnet geochronology work done on 14HSY-35E yields approximately a 4 My growth duration (45.7Ma-41.4Ma). and thermodynamic modeling calculates that garnet grew over a range of about 9Kbars (approximately 27Km), resulting an ascent rate of around 0.21GPa/Ma, which is in close agreement with values for the Stak eclogite

reported in Zhong et al., (2018). They also point out that the maximum residual inclusion pressure should have been approximately 1GPa if their sample exhumed in less than 1 million years, but measure values were closer to 0.52GPa. Given this evidence, and the timescales in which our samples experienced decompression, we propose that plastic relation of garnet during exhumation could have occurred, thus calculations that assume only elastic relaxation underestimate residual inclusion pressures and by extension, entrapment pressures.

3.7.2 Discussion of *P*-*T*-t paths

2.7.2a. Rates of exhumation

Results from thermodynamic models (section 4.1.2) coupled with $^{147}Sm/^{144}Nd$ garnet geochronology (section 3.5.3) yield exhumation rate ranging approximately 0.4-1.7 cm/yr. The lower end of this range is comparable to modeling results of Gerya et al., (2002), assuming a moderate convergence rate of 30km/My during subduction and the develop of a planar or wedge shaped subduction channel. Field relationships on Syros imply that exhumation of the CBU occurred along a subduction channel, and that buoyancy-driven ascension of metabasic and metagabbroic blocks occurred due to the presence of serpentine in the mélange. However, Schwartz et al., (2001) demonstrate that the density contrasts between our sample, 14HSY-35E (models predict a density of approximately 3050kg/m^3) and fully serpentinized (2650kg/m^3) require a subduction channel of at least 7-15km thick, depending on the assumed decoupling velocity, to induce upward flow. Even if we were to assume a maximum density contrast of 700kg/m^3, upward flow would only occur if the subduction channel is 2-3km wide. On Syros, mélange terrains are usually less than 1 km wide. This argues that additional mechanisms of exhumation must be at work in order for the CBU to have begun its ascent approximately 45Ma.

2.7.2b Slab rollback and synorogenic exhumation of the CBU

The Hellenic Subduction Zone is rapidly retreating southwards (Schellart, 2005), a phenomenon known as ‘slab rollback” (Chase 1979, 1980; Uyeda 1982; Royden & Husson 2006) which has major implications for the geodynamic processes that govern the evolution of Aegean (e.g. Long and Silver, 2008; Ring et al., 2010). Slab roll back is thought to be important once the underlying slab has been subducted to a depth of at least 80km (Schellart, 2005). In the case of the Hellenides

along the Aegean transect, this probably began at approximately 55-50 Ma (Thomson et al., 1998a, Faccenna et al., 2003, Kounov et al., 2004) and continues today. Evidence for slab roll back can be seen in the increasing magmatic ages moving north from the modern day Hellenic subduction trench, with north-most magmatism approximated at 38-35 Ma, Cyclades magmatism approximated at 17 Ma, and present day magmatism approximated at 4-3Ma (e.g. Ring et al., 2010).

Previous studies have cited slab rollback as a way to exhume HP and UHP lithologies during subduction because it induces moderate upward flow in the subduction channel (Brun and Faccenna, 2008; Husson et al., 2009) and creates localized regions of extensional faulting, which brings deeply (>60km) subducted material to the surface, which is texturally preserved on Syros (Rosenbaum et al., 2002; Ring et al., 2003; Keiter et al., 2004 & 2011; Philippon et al., 2011). Recent works (e.g. Roche et al., 2016; Lister and Forster, 2016; Laurent et al., 2017) have combined detailed structural studies of the CBU with Ar/Ar dating in white mica, and found that initiation of slab rollback coincides with blueschist overprinting due to decompression around 45Ma, followed by a thermal excursion around 35Ma, and final exhumation occurring from 25Ma-9Ma. This has been interpreted to suggest that slab rollback initiated decoupling of the CBU at ~50Ma and blueschist metamorphism of the CBU occurred at ~45Ma during synorogenic exhumation. We propose that sample 14HSY-35E preserves the initiation of slab rollback and subsequent exhumation of the CBU as evidenced by the $^{147}Sm/^{144}Nd$ ages of garnet cores (45.71±0.98Ma) and rims (41.4±1.7Ma) that agree with Ar/Ar studies (i.e Putlitz et al., 2005; Brocker et al., 2013; Lister and Forster, 2016), and calculated *P-T* paths that predict near isothermal decompression from approximately 2.2GPa to 1.6GPa, which produces exhumation rates between 0.4-1.7cm/yr.

3.8 CONCLUSIONS

In this study, we focus on developing *P-T-t* paths for 14HSY-35E, a sample found in southeastern Syros, Greece that contains garnets that exhibit chemical zoning that suggests that garnet grew in two stages. Thermodynamic modeling calculates that garnet nucleated at 485˚C and 2.2GPa and the first stage of growth stopped at approximately 530˚C and 2.0GPa, followed by a second stage of growth at 2.2GPa and 560˚C, which ended at 1.6GPa and 500˚C. Garnet growth occurred over a 4.3 My period from 45.1Ma-41.2Ma as determined via $^{147}Sm/^{144}Nd$ garnet geochronology. Given

the age of garnet cores and the duration of garnet growth, we propose that garnet grew during synorogenic exhumation of the CBU, which is in agreement with recent publications (Roche et al., 2016).

We also compare the results of quartz-in-garnet geobarometry with thermodynamic modeling and find that quartz-in-garnet geobarometry predicts that garnet grew isobarically, while thermodynamic modeling predicts that garnet grew during exhumation. We propose that the proximity of inclusions, especially in the core of garnet, and the amount of inclusions with lower shear moduli causing garnet to not behave like a rigid, infinite host, which results in an underestimate of entrapment pressure.

To conclude, the application of modern geothermobarometry and geochronology techniques to a sample from Syros, Greece that preserves high pressure metamorphic mineral assemblages provides us valuable insight into the evolution of the Cycladic Blueschist Unit. Such knowledge gained from the study eclogite facies samples increases our understanding of subduction zone processes such as elemental cycling, mass and heat transport, and exhumation of HP/LT terrains.

3.9 REFERENCES

Angel, R., Mazzucchelli, M., and Alvaro, M., 2014, Geobarometry from host-inclusion systems: the role of elastic relaxation: American Minerologist, v. 99, p. 2146-2149,. doi: 10.2138/am-2014-5047.

Angel, R., Mazzucchelli, M., Alvaro, M., and Nestola, 2017, EosFit-Pinc: A simple GUI for host-inclusion elastic thermobarometry: American Minerologist, v. 102, p. 1957–1960, doi: 10.2138/am-2017-6190.

Ashley, K., Caddick, M., Steele-MacInnis, M., Bodnar, R., and Dragovic, B., 2014, Geothermobarometric history of subduction recorded by quartz inclusions in garnet: Geochemistry, Geophysics, Geosystems, v. 15, no. 2, p. 350–360, doi: 10.1002/2013GC005106.

Auzanneau, E., Schmidt, M., Vielzeuf, D., and Connolly, J., 2009, Titanium in phengite: a geobarometer for high temperature eclogites: Contributions to Mineralogy and Petrology, v. 159, no. 1, p. 1–24, doi: 10.1007/s00410-009-0412-7.

Baxter, E., and Caddick, M., 2013, Garnet growth as a proxy for progressive subduction zone dehydration: Geology, v. 41, no. 6, p. 643646, doi: 10.1130/G34004.1.

Baxter, E. F., and Scherer, E. E., 2013, Garnet geochronology: timekeeper of tectonometamorphic processes: Elements, v. 9, p. 433-438, doi: 10.2113/gselements.9.6.433.

Beltrando, M., Hermann, J., Lister, G., Compagnoni, R., 2007, On the evolution of orogens: pressure cycles and deformation mode switches: Earth and Planetary Science Letters, v. 256, p. 372-388, doi: 10.1016/j.epsl.2007.01.022.

Blanco-Quintero, I., García-Casco, A., and Gerya, T., 2011, Tectonic blocks in serpentinite mélange (eastern Cuba) reveal large-scale convective flow of the subduction channel: Geology, v. 39, no. 1, p. 79–82, doi: 10.1130/G31494.1.

Bonneau, M., 1984, Correlation of the Hellenide nappes in the south-east Aegean and their tectonic reconstruction: Geological Society, London, Special Publications, v. 17, no. 1, p. 517–527, doi: 10.1144/GSL.SP.1984.017.01.38.

Breeding, C., Ague, J., and Bröcker, M., 2004, Fluid–metasedimentary rock interactions in subduction-zone mélange: Implications for the chemical composition of arc magmas: Geology, v. 32, no. 12, p. 1041–1044, doi: 10.1130/G20877.1.

Breemen, V.O., and Hawkesworth, C. J,. 1980, Sm-Nd isotopic study of garnets and their metamorphic host rocks, Transactions of the Royal Society of Edinburgh: Earth Sciences, v. 71, p. 97-103, doi: 10.1017/S0263593300013535.

Bröcker, M, and Enders, M, 2001, Unusual bulk-rock compositions in eclogite-facies rocks from Syros and Tinos (Cyclades, Greece): implications for U–Pb zircon geochronology: Chemical Geology, v. 175, no. 3-4, p. 581-603, doi: 10.1016/S0009-2541(00)00369-7.

Carlson, W., Patterson, D., Caddick, M., 2015, Beyond the equilibrium paradigm: How consideration of kinetics enhances metamorphic interpretation: American Mineralogist, v. 100, no. 8-9, p. 1659–1667, doi: 10.2138/am-2015-5097.

Chiu, H. Y,, Chung, S., Zarrinkoub, M. H., Mohammadi, S. S., Khatib, M. M., Izuka, Y., 2013, Zircon U–Pb age constraints from Iran on the magmatic evolution related to Neotethyan subduction and Zagros orogeny: Lithos, v. 162-163, p. 70-87. doi: 10.1016/j.lithos.2013.01.006

Cloos, M, 1982, Flow melanges: Numerical modeling and geologic constraints on their origin in the Franciscan subduction complex, California: Geological Society of America Bulletin, doi: 10.1130/0016-7606(1982)93<330:FMNMAG>2.0.CO;2.

Coggon, R., and Holland, T., 2002, Mixing properties of phengitic micas and revised garnet-phengite thermobarometers: Journal of Metamorphic Geology, v. 20, no. 7, p. 683–696, doi: 10.1046/j.1525-1314.2002.00395.x.

Connolly, J.A.D., 2005, Computation of phase equilibria by linear programming: A tool for geodynamic modeling and its application to subduction zone decarbonation: Earth and Planetary Science Letters, v. 236, no. 1-2, doi: 10.1016/j.epsl.2005.04.033.

Deiner, and Powell, 2012, Revised activity–composition models for clinopyroxene and amphibole: Journal of Metamorphic Geology, v. 30, no. 2, p. 131–142, doi: 10.1111/j.1525-1314.2011.00959.x.

Deiner, J., Powell, R., and White, R., 2008, Quantitative phase petrology of cordierite–orthoamphibole gneisses and related rocks: Journal of Metamorphic Geology, v. 26, no. 8, p. 795–814, doi: 10.1111/j.1525-1314.2008.00791.x.

Deiner, J., Powell, R., White, R., and Holland, T., 2007, A new thermodynamic model for clino- and orthoamphiboles in the system Na2O–CaO–FeO–MgO–Al2O3–SiO2–H2O–O: Journal of Metamorphic Geology, v. 25, no. 6, p. 631–656, doi: 10.1111/j.1525-1314.2007.00720.x.

Dixon, JE, Feenstra, A, Jansen, J., Kreulen, R, Ridley, J, Salemink, J, and Schuiling, RD, 1987, Excursion Guide to the Field Trip on Seriphos, Syros, and Naxos: , Chemical Transport in Metasomatic Processes, p. 467–518.

Dragovic, B., Samanta, L., Baxter, E., and Selverstone, J., 2012, Using garnet to constrain the duration and rate of water-releasing metamorphic reactions during subduction: An example from Sifnos, Greece: Chemical Geology, v. 314, p. 9–22, doi: 10.1016/j.chemgeo.2012.04.016.

Dragovic, B., Baxter, E., and Caddick, M., 2015, Pulsed dehydration and garnet growth during subduction revealed by zoned garnet geochronology and thermodynamic modeling, Sifnos, Greece: Earth and Planetary Science Letters, v. 413, p. 111–122, doi: 10.1016/j.epsl.2014.12.024.

Durr, S., Altherr, R., Keller, J., Okrusch, M. & Seidel, E. 1978. The median Aegean crystalline belt: Stratigraphy, structure, metamorphism, magmatism. In: Alps, Appenines, Hellenides (edited by Cloos, H., Roeder, D. & Schmidt, H.). Union Commission on Geodynamics, Scientific Report, 455--477.

Enami, M, Nishiyama, T, and Mineralogist, M.-T., 2007, Laser Raman microspectrometry of metamorphic quartz: A simple method for comparison of metamorphic pressures: American Mineralogist, v. 92, p. 1303-1315, doi: 10.2138/am.2007.2438.

Fuhrman, ML, and Lindsley, DH, 1988, Ternary-feldspar modeling and thermometry: American Mineralogist, v. 73, no. 3-4, p. 201-215.

Funiciello, Moroni, Piromallo, Faccenna, Cenedese, and Bui, 2006, Mapping mantle flow during retreating subduction: Laboratory models analyzed by feature tracking: Journal of Geophysical Research: Solid Earth (1978–2012), v. 111, no. B3, doi: 10.1029/2005JB003792.

Gaidies, F., Capitani, C., Abart, R., Schuster, R., 2008, Prograde garnet growth along complex P–T–t paths: results from numerical experiments on polyphase garnet from the Wo¨lz Complex (Austroalpine basement), Contributions to Mineralogy and Petrology, v. 155, no. 6, p. 673-688, doi: 10.1007/s00410-007-0264-y.

Gerya, T., Stöckhert, B., and Perchuk, A., 2002, Exhumation of high-pressure metamorphic rocks in a subduction channel: A numerical simulation: Tectonics, v. 21, no. 6, p. 6–1–6–19, doi: 10.1029/2002TC001406.

Green, E., Holland, T., and Powell, R., 2007, An order-disorder model for omphacitic pyroxenes in the system jadeite-diopside-hedenbergite-acmite, with applications to eclogitic rocks: American Mineralogist, v. 92, no. 7, p. 1181–1189, doi: 10.2138/am.2007.2401.

Griffin, WL, and Nature, B.-H., 1980, Caledonian Sm–Nd ages and a crustal origin for Norwegian eclogites: Nature, v. 285, p. 319–321, doi: 10.1038/285319a0.

Grimmer, J. C., Ratschbacher, L., McWilliams, M., Franz, L., gaitzsch, I., Tichomirowa, M., Hacker, B., Zhang, Y., 2003, When did the ultrahigh-pressure rocks reach the surface? A 207Pb/206Pb zircon, 40Ar/39Ar white mica, Si-in-white mica, single-grain provenance study of Dabie Shan synorogenic froeland sediments, Chemical Geology, v. 197, no. 1-4, p. 87-110, doi: 10.1016/S0009-2541(02)00321-2.

Harvey, J, Baxter, E. F., 2009, An improved method for TIMS high precision neodymium isotope analysis of very small aliquots (1–10 ng): Chemical Geology, v. 258, no. 3-4, p. 251-257. doi: 10.1016/j.chemgeo.2008.10.024

Holland, T, and Powell, R, 1991, A Compensated-Redlich-Kwong (CORK) equationn for volumes and fugacities of CO2 and H2O in the range 1 bar to 50 kbar and 100–1600 C: Contributions to Mineralogy and Petrology, v. 109, no. 2, p. 265-273, doi: 10.1007/BF00306484.

Holland, T., and Powell, R., 1998, An internally consistent thermodynamic data set for phases of petrological interest: Journal of Metamorphic Geology, v. 16, no. 3, p. 309–343, doi: 10.1111/j.1525-1314.1998.00140.x.

Hollister, L., 1966, Garnet zoning: an interpretation based on the Rayleigh fractionation model: Science, V. 154, No. 3757, p. 1647-1651 doi: 10.1126/science.154.3757.1647.

Hoschek, G., 2013, Garnet zonation in metapelitic schists from the Eclogite Zone, Tauern Window, Austria: comparison of observed and calculated profiles, European Journal of Mineralogy, v. 24, no. 4, p. 615-629, doi: 10.1127/0935-1221/2013/0025-2310.

Kabir, M. F., and Takasu, A., 2010, Evidence for multiple burial–partial exhumation cycles from the Onodani eclogites in the Sambagawa metamorphic belt, central Shikoku, Japan: Journal of Metamorphic Geology, v. 28, no. 8, p. 873-893, doi: 10.1111/j.1525-1314.2010.00898.x.

Keiter, M., Piepjohn, K., Ballhaus, C., Lagos, M., and Bode, M., 2004, Structural development of high-pressure metamorphic rocks on Syros island (Cyclades, Greece): Journal of Structural Geology, v. 26, no. 8, p. 14331445, doi: 10.1016/j.jsg.2003.11.027.

Kohn, M., 2014, “Thermoba-Raman-try”: Calibration of spectroscopic barometers and thermometers for mineral inclusions: Earth and Planetary Science Letters, v. 388, no. p. 187-196, doi: 10.1016/j.epsl.2013.11054

Krohe, A., Mposkos, E., 2002, Multiple generations of extensional detachments in the Rhodope Mountains (northern Greece): evidence of episodic exhumation of high-pressure rocks: Geological Society, London, Special Publcations v. 204, p. 151-178, doi: 10.1144/GSL.SP.2002.204.01.10.

Lagos, M., E. E. Scherer, F. Tomaschek, C. Münker, M. Keiter, J. Berndt, and C. Ballhaus (2007), High precision Lu–Hf geochronology of Eocene eclogite-facies rocks from Syros, Cyclades, Greece, Chem. Geol., 243(1–2), 16–35, doi:10.1016/j.chemgeo.2007.04.008.

Laurent, V., Jolivet, L., Roche, V., Augier, R., Scaillet, S., Cardello, L., 2016, Strain localization in a fossilized subduction channel: Insights from the Cycladic Blueschist Unit (Syros, Greece): Tectonophysics, v. 672-673, p. 150-169, doi: 10.1016/j.tecto.2016.01.036

Lips, A., Whitea, S., H., Wijbransb, J. R., 1998, 40Ar/39Ar laserprobe direct dating of discrete deformational events: a continuous record of early Alpine tectonics in the Pelagonian Zone, NW Aegean area, Greece: Tectonophysics, v. 298, no. 1-3, p. 133-153, doi: 10.1016/S0040-1951(98)00181-4

Lister, G., and Forster, M., 2016, White mica 40Ar/39Ar age spectra and the timing of multiple episodes of high-pressure metamorphic mineral growth in the Cycladic eclogite-blueschist belt, Syros, Aegean Sea, Greece: Journal of Metamorphic Geology, v. 34, no. 5, p. 401-421, doi: 10.1111/jmg.12178.

Lister, G. S., and Raouzaios, A., 1996, The tectonic significance of a porphyroblastic blueschist facies overprint during Alpine orogenesis: Sifnos, Aegean Sea, Greece: Journal of Structural Geology, v. 18, no. 12, p. 1417-1435, doi: 10.1016/S0191-8141(96)00072-7

Long, M., and Silver, P., 2008, The Subduction Zone Flow Field from Seismic Anisotropy: A Global View: Science, v. 319, no. 5861, p. 315–318, doi: 10.1126/science.1150809.

Maluski, H, Bonneau, M, and Kienast, JR, 1987, Dating the metamorphic events in the Cycladic area; 39 Ar/40 Ar data from metamorphic rocks of the Island of Syros (Greece): Bulletin de la Société géologique de France, v. 3, no. 5, p. 833-842, doi: 10.2113/gssgfbull.III.5.833.

Maruyama, Liou, and Terabayashi, 1996, Blueschists and Eclogites of the World and Their Exhumation: International Geology Review, v. 38, no. 6, p. 485–594, doi: 10.1080/00206819709465347.

Milani, S., Nestola, F., Alvaro, M., Pasqual., D., Mazzucchelli, M. L., Domeneghetti, M. C., Geiger, C. A., 2015, Diamond–garnet geobarometry: The role of garnet compressibility and expansivity: Lithos, v. 227, p. 140-147, doi: 10.1016/j.lithos.2015.03.017

Mposkos, E., and Kostopoulos, D., 2001, Diamond, former coesite and supersilicic garnet in metasedimentary rocks from the Greek Rhodope: a new ultrahigh-pressure metamorphic province established: Earth and Planetary Science Letters, v. 192, no. 4, p. 497–506, doi: 10.1016/S0012-821X(01)00478-2.

Okrusch, M,. Broecker, M., 1990, Eclogites associated with high-grade blueschists in the Cyclades archipelago, Greece: A review: European Journal of Mineralogy, v. 2, no. 4, p. 451-478, doi: 10.1127/ejm/2/4/0451

Pollington, A., Baxter, E. F., 2010, High resolution Sm–Nd garnet geochronology reveals the uneven pace of tectonometamorphic processes: Earth and Planetary Science Letters, v. 293, no. 1-2, p. 63-71, doi: 10.1016/j.epsl.2010.02.019

Pollington, A., Baxter, E. F., 2011, High precision microsampling and preparation of zoned garnet porphyroblasts for Sm–Nd geochronology: Chemical Geology, v. 281, no. 3-4, p. 270-282, doi: 10.1016/j.chemgeo.2010.12.014

Peacock, S., 1993, The importance of blueschist→ eclogite dehydration reactions in subducting oceanic crust: Geological Society of America Bulletin, v. 105, p. 684-694, doi: 10.1130/0016-7606(1993)105<0684:TIOBED>2.3.CO;2.

Philippon, Gueydan, Pitra, and Brun, J., 2013, Preservation of subduction-related prograde deformation in lawsonite pseudomorph-bearing rocks: Journal of Metamorphic Geology, v. 31, no. 5, p. 571–583, doi: 10.1111/jmg.12035.

Putlitz, Cosca, M.A., and Schumacher, J.C., 2005, Prograde mica 40Ar/39Ar growth ages recorded in high pressure rocks (Syros, Cyclades, Greece): Chemical Geology, v. 214, no. 1-2, p. 79–98, doi: 10.1016/j.chemgeo.2004.08.056.

Qian J.H., and Wei C.J., 2016, P–T–t evolution of garnet amphibolites in the Wutai–Hengshan area, North China Craton: insights from phase equilibria and geochronology, Journal of Metamorphic Geology, v. 34, no. 5, p. 423-446, doi: 10.1111/jmg.12186

Ribe, N., 1989, Seismic anisotropy and mantle flow: Journal of Geophysical Research: Solid Earth (1978–2012), v. 94, no. B4, p. 4213–4223, doi: 10.1029/JB094iB04p04213.

Ring, U., Glodny, J., Will, T., and Thomson, S., 2010, The Hellenic Subduction System: High-Pressure Metamorphism, Exhumation, Normal Faulting, and Large-Scale Extension: Earth and Planetary Sciences, v. 38, no. 1, p. 45–76, doi: 10.1146/annurev.earth.050708.170910.

Ring, U., and Layer, P., 2003, High-pressure metamorphism in the Aegean, eastern Mediterranean: Underplating and exhumation from the Late Cretaceous until the Miocene to Recent above the retreating Hellenic subduction zone: Tectonics, v. 22, no. 3, p. n/a–n/a, doi: 10.1029/2001TC001350.

Roche, V., Laurent, V,. Cardello, G. L., Jolivet, L., Scaillet, S., Anatomy of the Cycladic Blueschist Unit on Sifnos Island (Cyclades, Greece): Journal of Geophysics, v. 97, p. 62-87, doi: 10.1016/j.jog.2016.03.008

Rosenbaum, G., Avigad, D., and Sánchez-Gómez, M., 2002, Coaxial flattening at deep levels of orogenic belts: evidence from blueschists and eclogites on Syros and Sifnos (Cyclades, Greece): Journal of Structural Geology, v. 24, no. 9, p. 1451–1462, doi: 10.1016/S0191-8141(01)00143-2.

Rosenfeld, J. L. (1969), Stress effects around quartz inclusions in almandine and the piezothermometry of coexisting aluminum silicates, Am. J. Sci., v. 267, p. 317–351, doi: 10.2475/ajs.267.3.317

Rosenfeld, J. L., and A. B. Chase (1961), Pressure and temperature of crystallization from elastic effects around solid inclusions in minerals, Am. J. Sci., v. 259, p. 519–541, doi: 10.2475/ajs.259.7.519

Rubatto, D., Regis, D., Hermann, J., Boston, K., Engi, M., Beltrando, M., McAlphine, S. R. B., 2011, Yo-yo subduction recorded by accessory minerals in the Italian Western Alps: Nature Geosciences, v. 4, p. 338-342, doi: 10.1038/ngeo1124.

Schellart, W., 2004, Quantifying the net slab pull force as a driving mechanism for plate tectonics: Geophysical Research Letters, v. 31, no. 7, doi: 10.1029/2004GL019528.

Schmidt, C., and M. A. Ziemann (2000), In-situ Raman spectroscopy of quartz: A pressure sensor for hydrothermal diamond-anvil cell experiments at elevated temperatures, Am. Mineral., v. 85, no. 11-12, p. 1725–1734, doi: 10.2138/am-2000-11-1216

Schumacher, J., Brady, J., Cheney, J., and Tonnsen, R., 2008, Glaucophane-bearing Marbles on Syros, Greece: Journal of Petrology, v. 49, no. 9, p. 1667–1686, doi: 10.1093/petrology/egn042.

Sherlock, S., Kelley, S., Inger, S., Harris, N., and Okay, A., 1999, 40Ar-39Ar and Rb-Sr geochronology of high-pressure metamorphism and exhumation history of the Tavsanli Zone, NW Turkey: Contributions to Mineralogy and Petrology, v. 137, no. 1-2, p. 46–58, doi: 10.1007/PL00013777.

Smye, A., Greenwood, L., and Holland, T., 2010, Garnet–chloritoid–kyanite assemblages: eclogite facies indicators of subduction constraints in orogenic belts: Journal of Metamorphic Geology, v. 28, no. 7, p. 753–768, doi: 10.1111/j.1525-1314.2010.00889.x.

Spear, F., 2017, Garnet growth after overstepping: Chemical Geology, vol. 466, p. 491-499, doi: 10.1016/j.chemgeo.2017.06.038

Spear, FS, and Patterson, D., 2017, The implications of overstepping for metamorphic assemblage diagrams (MADs): Chemical Geology.

Spear, Thomas, Hallett, B. W., Overstepping the garnet isograd: a comparison of QuiG barometry and thermodynamic modeling: Contributions to Mineralogy and Petrology, v. 168, no. 3, doi: 10.1007/s00410-014-1059-6.

Spence, W, 1987, Slab pull and the seismotectonics of subducting lithosphere: Reviews of Geophysics, v. 25, no, 1, p. 55-69, doi: 10.1029/RG025i001p00055.

Tirone M., and Ganguly J., 2010, Garnet compositions as recorders of P–T–t history of metamorphic rocks, Gondwana Research, v. 18, no. 1, p. 138-146, doi: 10.1016/j.gr.2009.12.010
Torsvik, T., Steinberger, B., Cocks, R., and Burke, K., 2008, Longitude: Linking Earth's ancient surface to its deep interior: Earth and Planetary Science Letters, v. 276, no. 3-4, p. 273–282, doi: 10.1016/j.epsl.2008.09.026.

Trotet, F., Jolivet, L., and Vidal., O., 2001, Tectono-metamorphic evolution of Syros and Sifnos islands (Cyclades, Greece): Tectonophysics, v. 338, no. 2, p. 179–206, doi: 10.1016/S0040-1951(01)00138-X.

Trotet, F., Vidal., O., and Jolivet, L., 2001, Exhumation of Syros and Sifnos metamorphic rocks (Cyclades, Greece). New constraints on the *P-T* paths: European Journal of Mineralogy, v. 13, no. 5, p. 901920, doi: 10.1127/0935-1221/2001/0013-0901.

Viete, D. R., Hermann, J., Lister, G., S., Stenhouse, I. R., 2011, The nature and origin of the Barrovian metamorphism, Scotland: diffusion length scales in garnet and inferred thermal time scales: Journal of the Geological Society, v. 168, no. 1, p. 115-132, doi: 10.1144/0016-76492009-087

Von Quadt, A., Moritz, R., Peytcheva, I., Heinrich, C. A., 2005, Geochronology and geodynamics of Late Cretaceous magmatism and Cu–Au mineralization in the Panagyurishte region of the Apuseni–Banat–Timok–Srednogorie belt, Bulagria: Ore Geology Reviews, v. 27, no. 1-4, p. 95-126, doi: 10.1016/j.oregeorev.2005.07.024

White, R., Pomroy, N., and Powell, R., 2005, An in situ metatexite–diatexite transition in upper amphibolite facies rocks from Broken Hill, Australia: Journal of Metamorphic Geology, v. 23, no. 7, p. 579–602, doi: 10.1111/j.1525-1314.2005.00597.x.

White, R., Powell, R., and Clarke, G., 2002, The interpretation of reaction textures in Fe-rich metapelitic granulites of the Musgrave Block, central Australia: constraints from mineral equilibria calculations in the system K2O–FeO–MgO–Al2O3–SiO2–H2O–TiO2–Fe2O3: Journal of Metamorphic Geology, v. 20, no. 1, p. 41–55, doi: 10.1046/j.0263-4929.2001.00349.x.

Wolfe, Oliver. M., and Spear, F., 2018, Determining the amount of overstepping required to nucleate garnet during Barrovian regional metamorphism: Journal of Metamorphic Geology, v. 36, no. 1, p. 79-94, doi: 10.1111/jmg.12284.

Zhang, Y., 1998, Mechanical and phase equilibria in inclusion–host systems: Earth and Planetary Science Letters, v. 157, no. 3-4, p. 209-222, doi: 10.1016/S0012-821X(98)00036-3

Zhao, D., 2004, Global tomographic images of mantle plumes and subducting slabs: insight into deep Earth dynamics: Physics of the Earth and Planetary Interiors, v. 146, no. 1-2, p. 3–34, doi: 10.1016/j.pepi.2003.07.032.

3.10 FIGURES

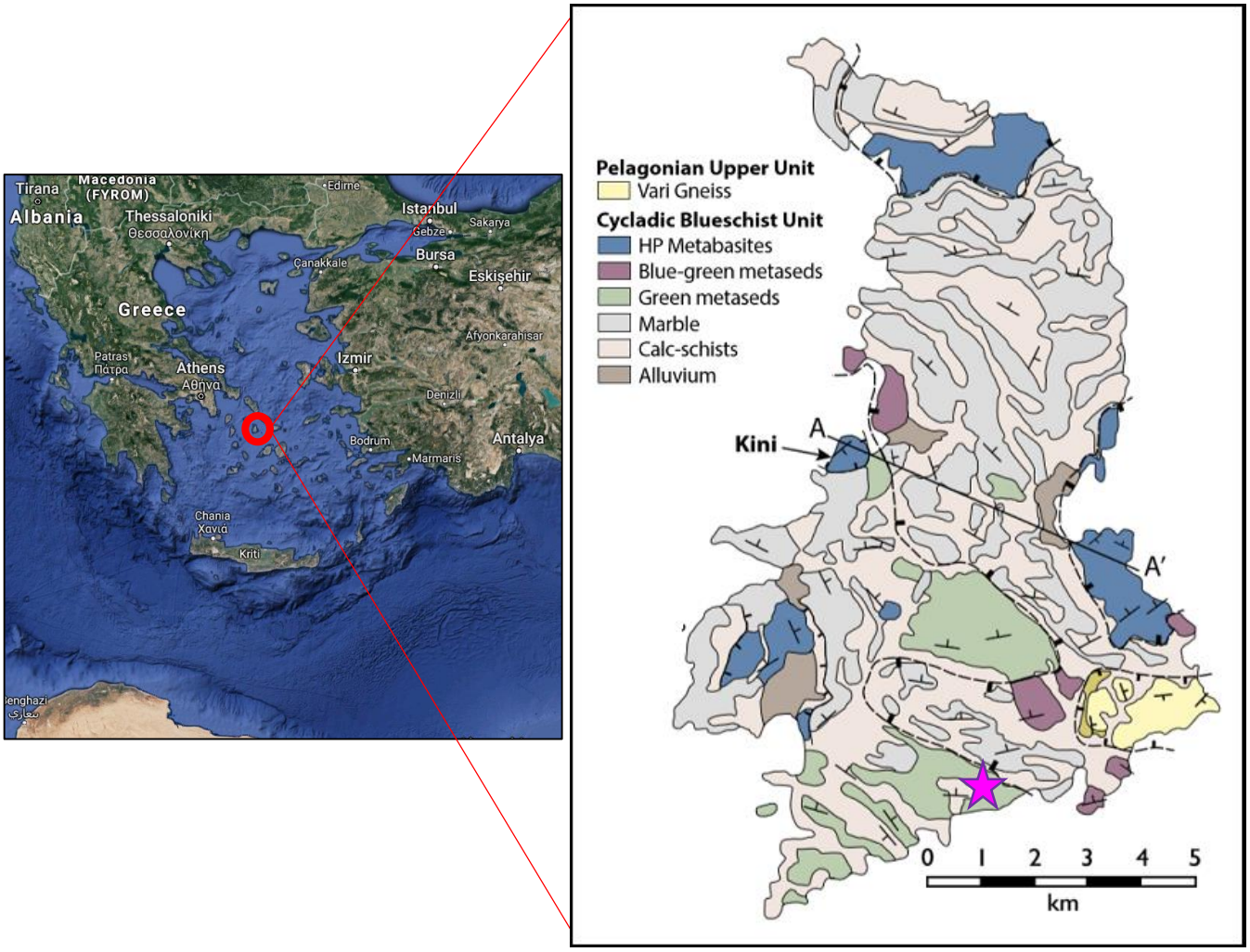

Figure 3.1: Left: Geographic map of the Aegean and surrounding countries. Right: Simplified geologic map of Syros Greece modified after Behr et al., (2018) illustrating the location of HP/LT terrains (Dark colors) and sample site location (pink star).

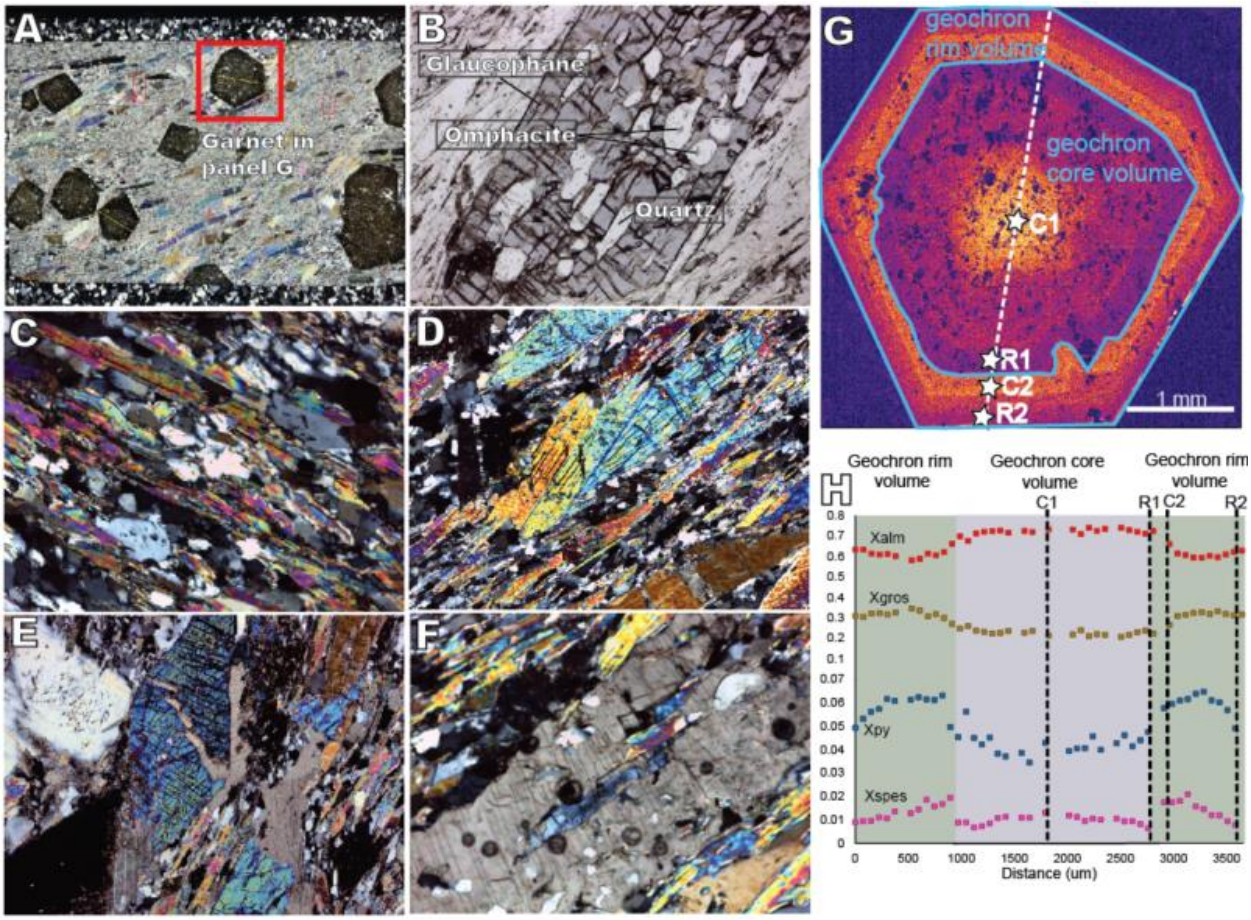

Figure 3.2: Left: Photo micrographs of mineral textures in 14HSY-35E. A. Thin section in CPL. B. Late stage glaucophane overgrown quartz which is included by omphacite (20X). C. Foliated matrix of quartz and phengite (20X). D. Paragonite overgrowing primary foliation (10X) E. Late carbonate growing over glaucophane (10X). F. Late carbonate replacing epidote. Top Right: elemental map of garnet. C1, R1, C2, and R2 indicate the composition of garnet used to constrain pressure-temperature (*P*-*T*) conditions via thermodynamic). The dashed white line indicates the traverse of quantitative microprobe analysis for determining garnet composition (H).

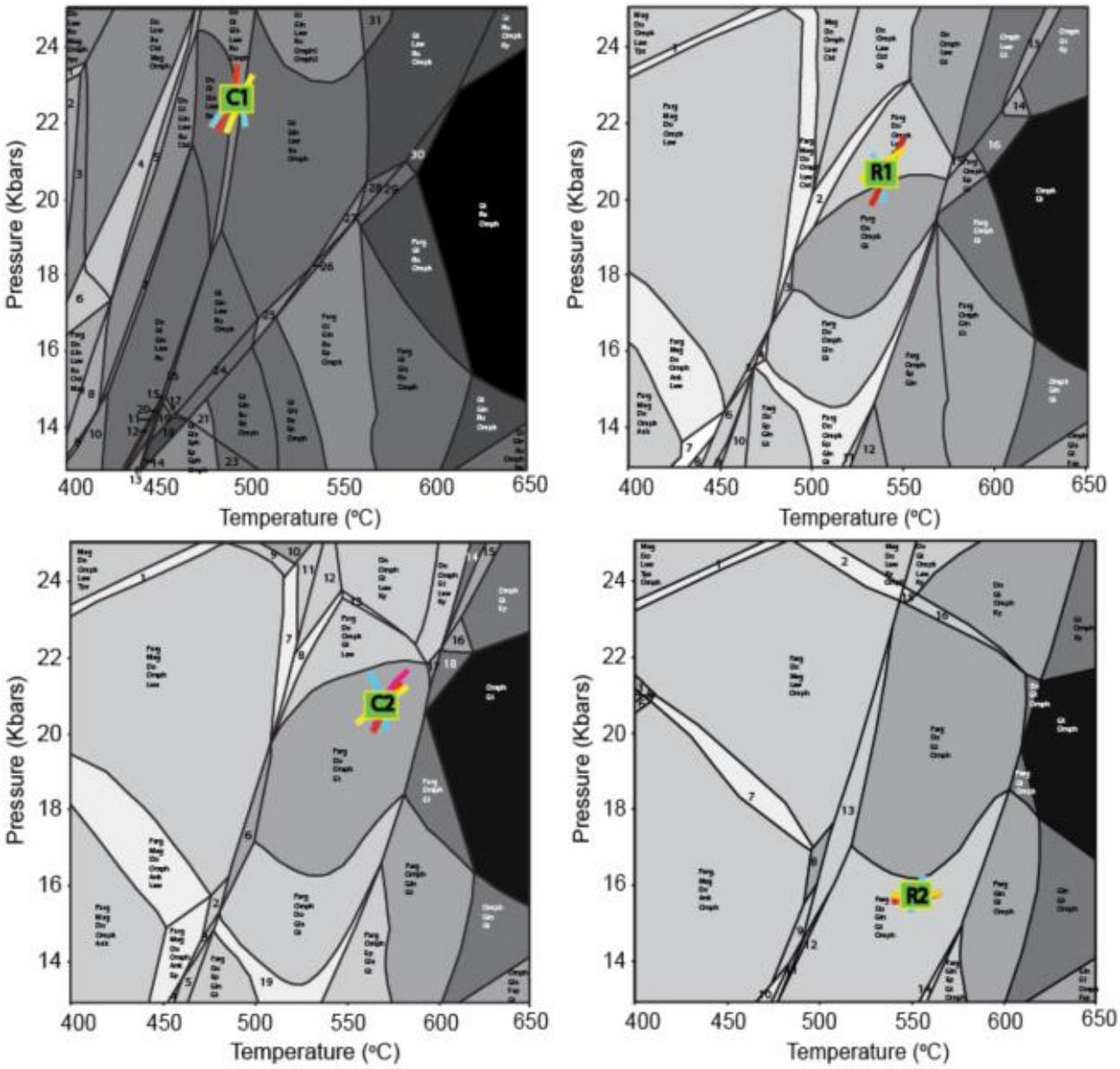

Figure 3.3 Calculated *P-T* conditions for different periods during garnet growth: Garnet core, (C1): edge of the inclusion rich zone, (R1): beginning of the inclusion free zone, (C2): rim of the garnet crystal (R2).

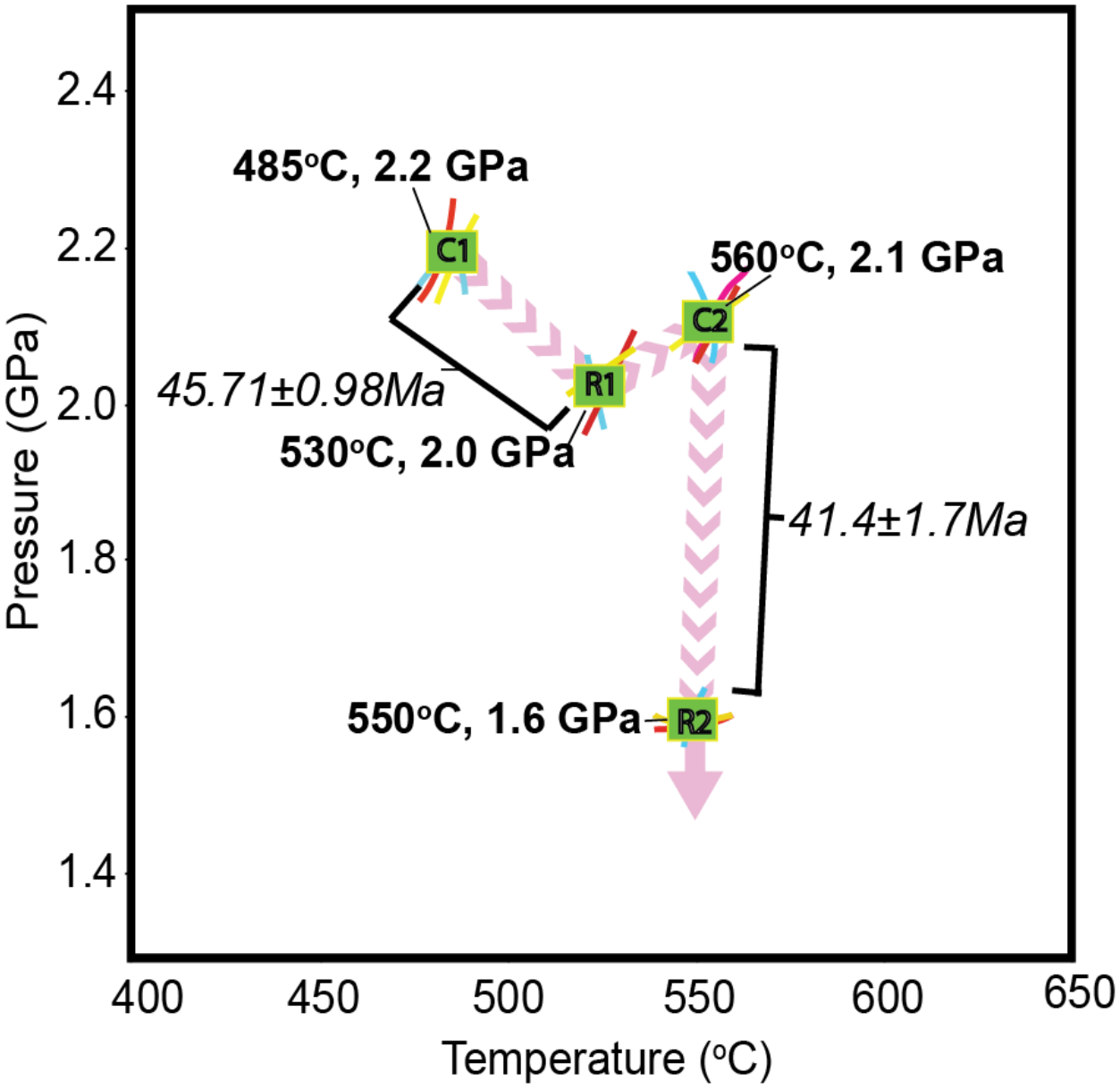

Figure 3.4: Compilation of thermodynamic modeling and geochronology.

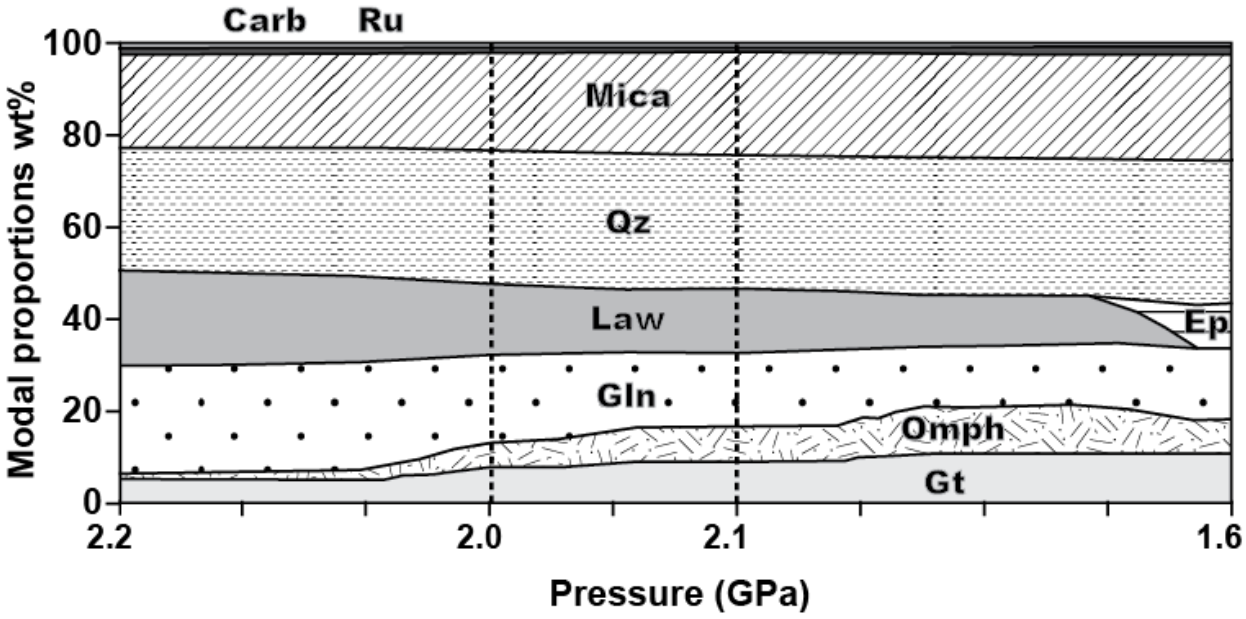

Figure 3.5: Mineralogical evolution of 14HSY-35E, as predicted by thermodynamic phase equilbria along the calculated *P-T* path (Figure 3.4). Dashed lines represent the end of first garnet growth (R1) and the beginning of second garnet growth (C2).

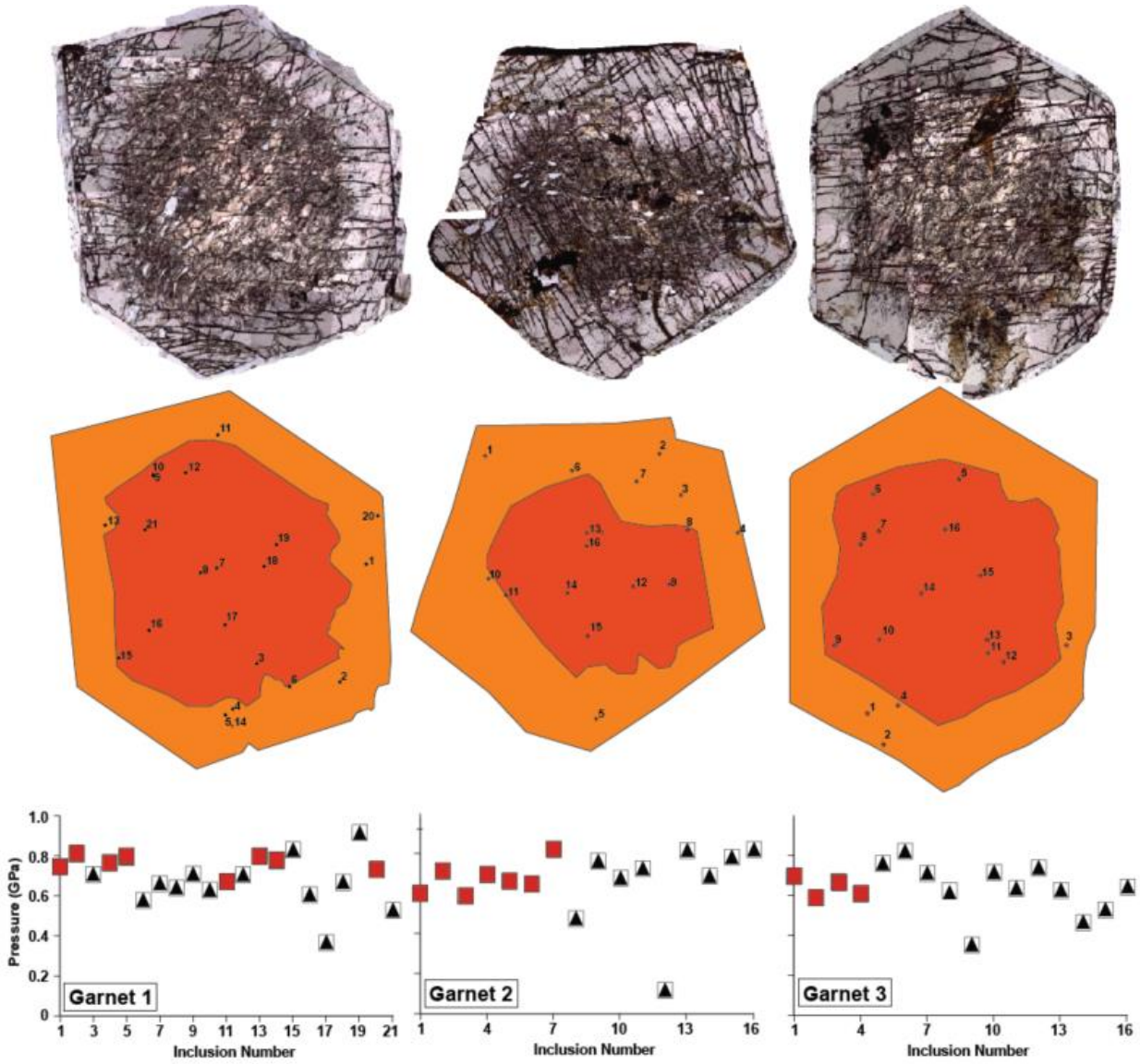

Figure 3.6: Top: Photo micrographs of host garnet crystals used in quartz in garnet geochronology (top) and schematic diagrams of the same crystals showing the location of quartz inclusions used in barometry. The dark orange garnet cores have a high inclusion density of quartz, epidote, clinopyroxene, rutile, apatite, and ± carbonate. The light orange garnet rims have a low inclusion density of quartz and apatite. Bottom: Residual inclusion pressures calculated for each garnet using methods by Ashely et al., (2014) (triangles), and Kohn (2014) (squares). Red squares are inclusions that reside in the cores of garnet.

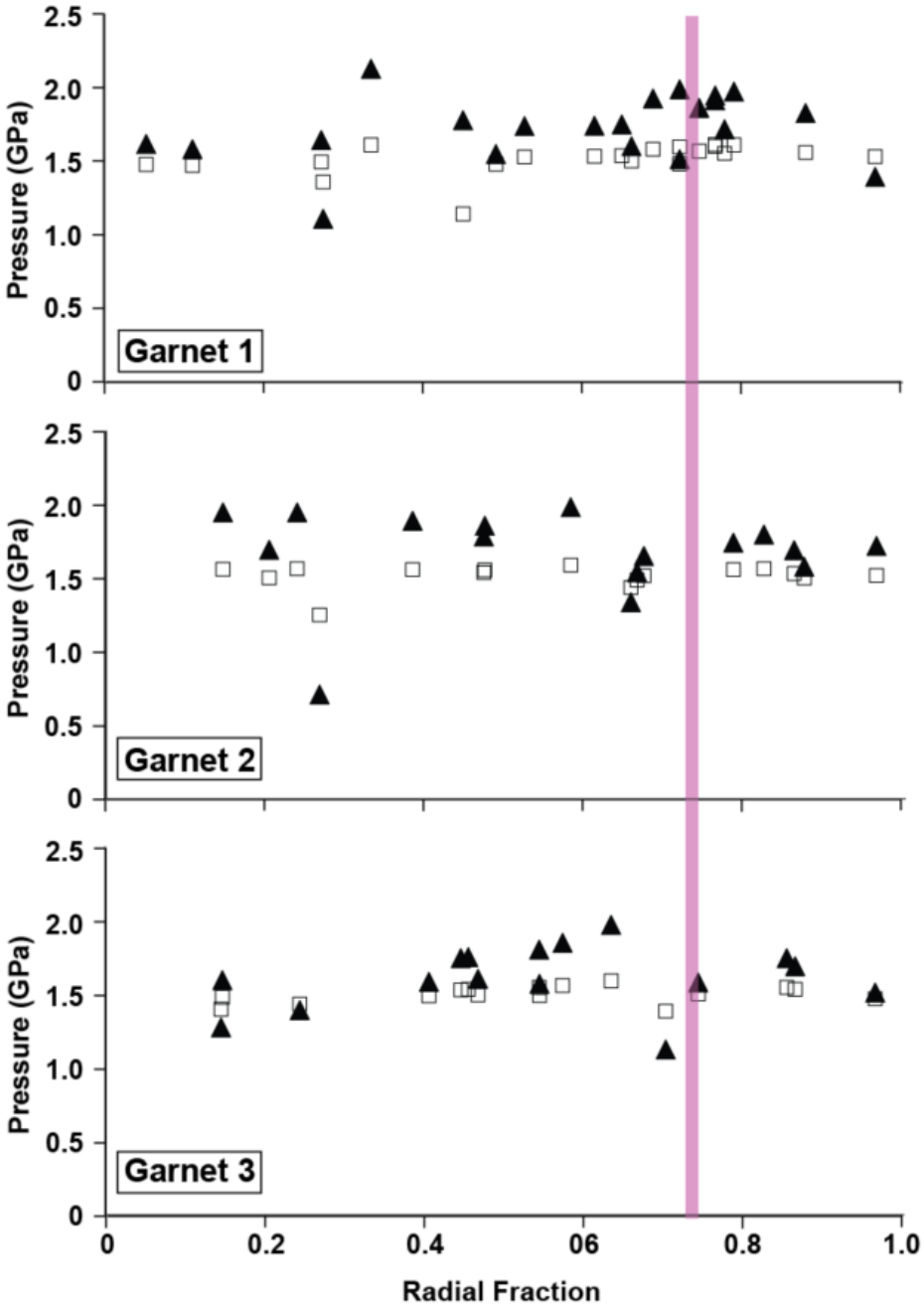

Figure 3.7: Entrapment pressures of quartz inclusions determined using EoSfit-Pinc (Angel et al., 2017) (solid triangles), and methods described in Ashley et al., (2014) (open squares). Inclusions are plotted as a function of radial fraction from the core, with 0 = at the core and 1= at the rim. The transition from an inclusion dense to an inclusion light domain occurs at a radial fraction of approximately 0.75 (pink line). In general EosFit-Pinc yields a wider spread of entrapment pressures and a high average entrapment pressure.

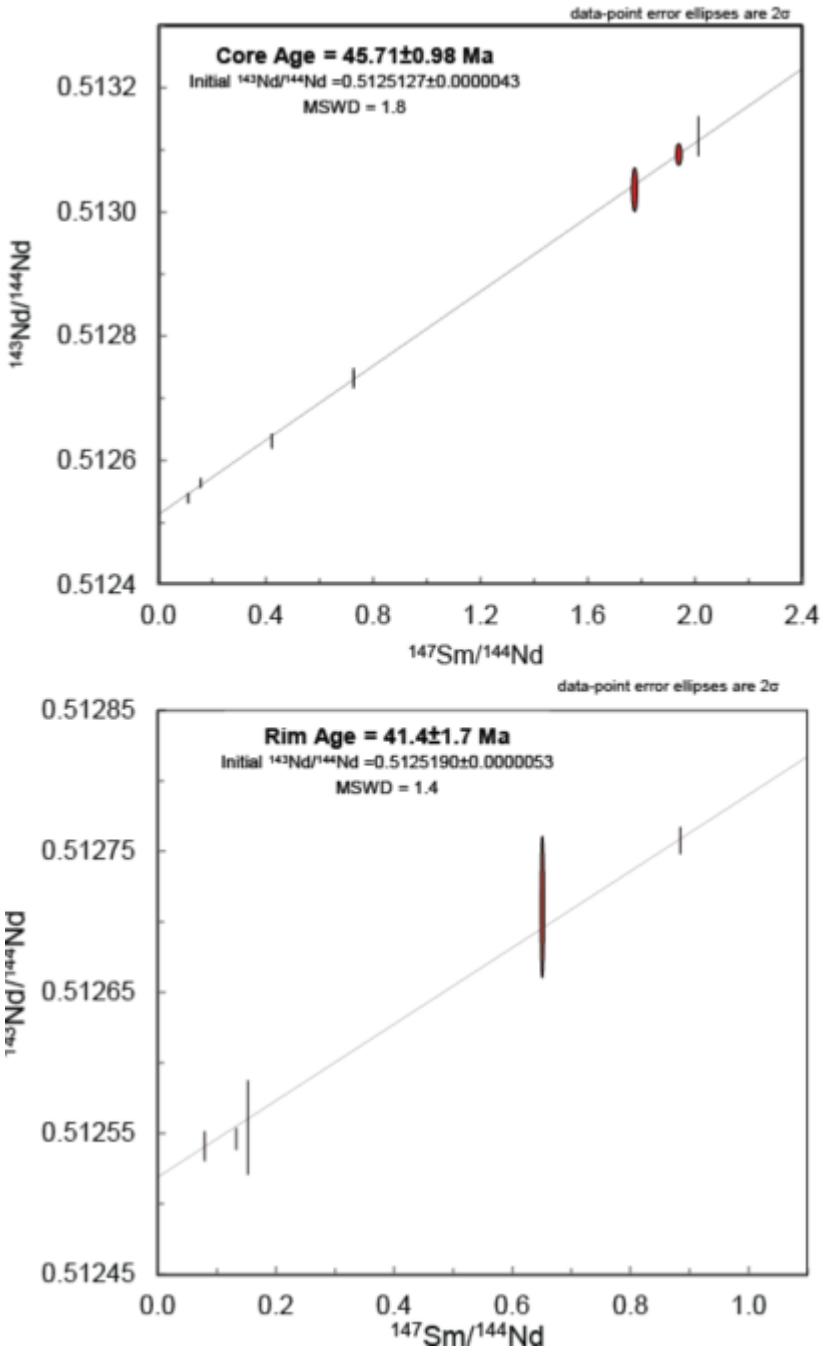

Figure 3.8: Sm/Nd isochrons for garnet core (top) and rim (bottom).

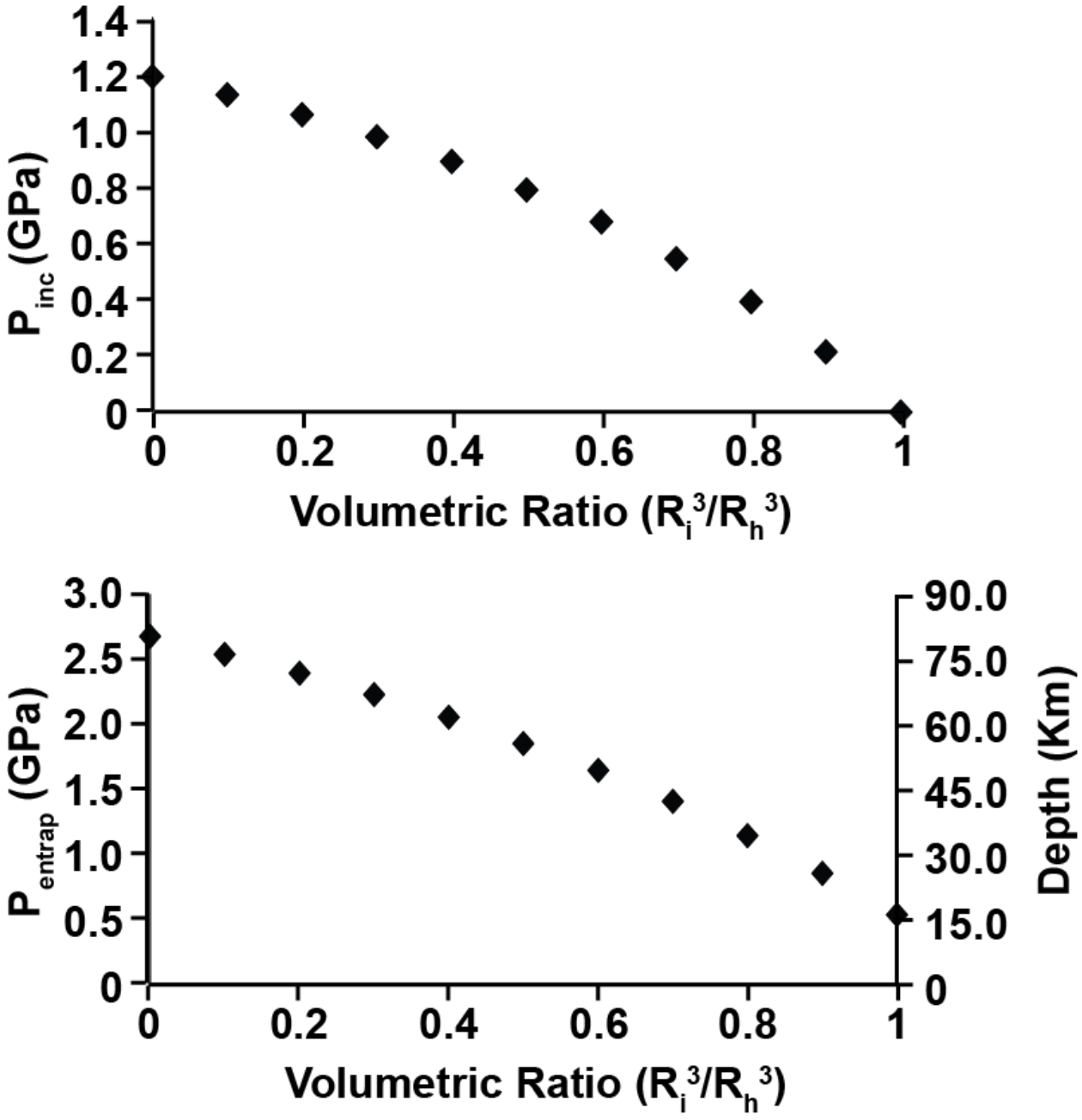

Figure 3.9: Top: Relationship between the residual pressure in the inclusion as a function of volumetric ratio of inclusion to host. Values were calculated using equation 1, from Zhang (1998). Bottom: We used the software EosFit-Pinc by Angel et al., (2017) to calculate an entrapment pressure and corresponding depth.

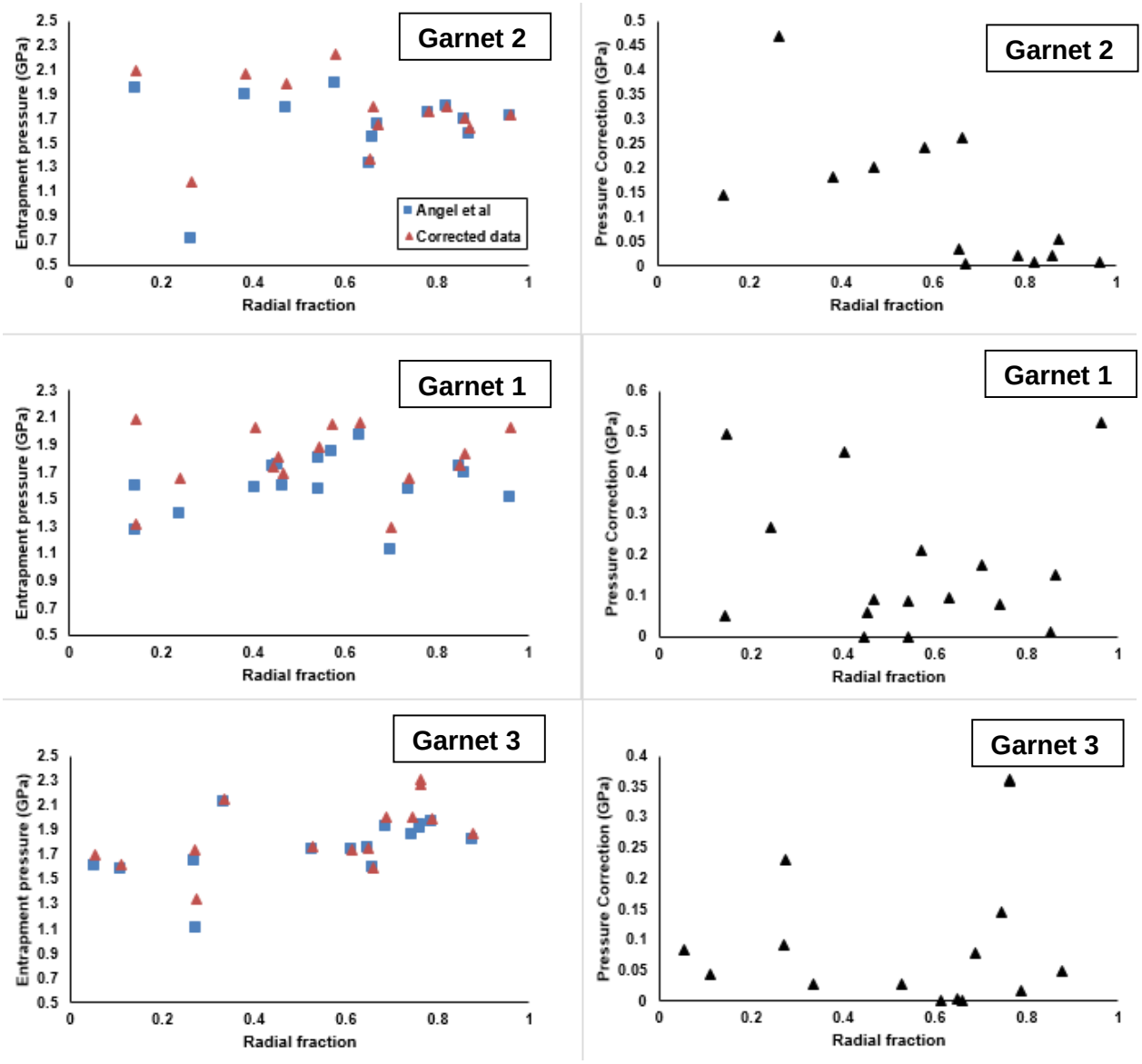

Figure 3.10: Diagrams on the left plot entrapment pressure as a function of radial distance from the garnet core. Blue squares represent pressures calculated using EosFit-Pinc (Angel et al., 2017), and red triangles represent pressures after residual pressures were corrected for inclusion proximity. Diagrams on the right show the magnitude of each correction to entrapment pressure.

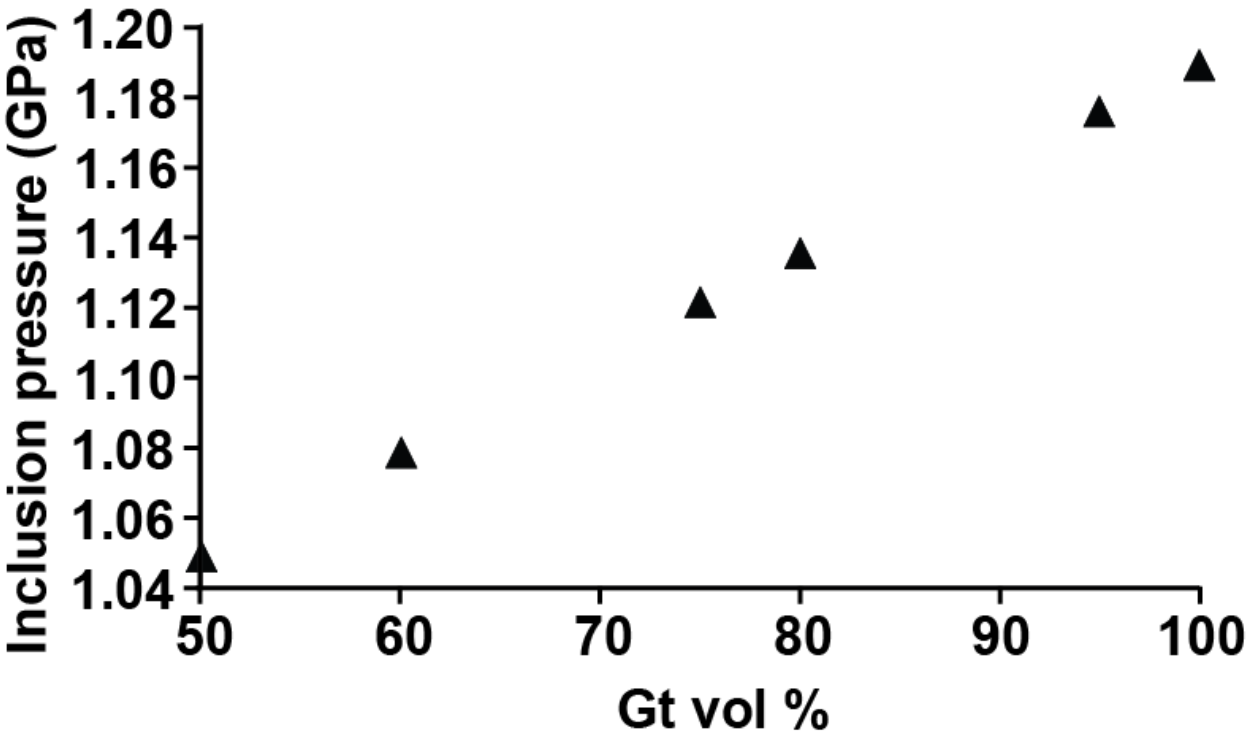

Figure 3.11: Diagram illustrating how residual inclusion pressure is affected if the host phase behaves as garnet+epidote instead of as pure garnet. Though underestimations of inclusion pressure are much less than factors such as distance of host surrounding the inclusion, the presence of other inclusion phases within the host, especially in high population densities can reduce inclusion pressure.

3.11 TABLES

Mineral	SiO2	TiO2	Al2O3	MgO	CaO	MnO	FeO	Na2O	K2O	CO2	Total Wt %
Garnet	37.86	0.06	22.01	1.42	11.06	0.57	29.28	0.03	0.01	0.00	102.30
Glaucophane	58.62	0.01	12.11	8.50	0.61	0.02	12.85	7.26	0.02	0.00	100.00
K-Mica	54.78	0.24	27.21	3.68	0.01	0.00	3.00	0.38	10.71	0.00	100.00
Na-Mica	49.77	0.06	41.33	0.15	0.17	0.01	0.33	7.47	0.71	0.00	100.00
Epidote	40.07	0.11	28.66	0.00	24.16	0.04	0.00	0.02	0.01	0.00	93.07
Titanite	31.95	34.86	2.64	0.00	30.30	0.02	0.20	0.02	0.00	0.00	100.00
Quartz	99.94	0.00	0.00	0.00	0.00	0.01	0.04	0.01	0.00	0.00	100.00
Calcite	0.02	0.00	0.00	0.00	55.75	0.03	0.17	0.02	0.00	44.00	100.00
Omphacite	58.63	0.03	12.06	6.01	11.46	0.03	7.17	7.64	0.01	0.00	103.04

Table 3.1: Representative electron microprobe analyses of minerals found in 14HSY-35E.

	SiO2	TiO2	Al2O3	MgO	CaO	MnO	FeO	Fe2O3	Na2O	K2O
XRF Bulk rock	64.25	0.68	15.38	2.48	4.97	0.15	6.77	1.06	1.82	2.43
Minus 49 vol% gt	66.08	0.73	14.97	2.56	4.58	0.12	5.30	1.13	1.94	2.60
Minus 50 vol% gt	66.11	0.73	14.96	2.56	4.57	0.12	5.28	1.13	1.94	2.60
Minus 99 vol% gt	68.03	0.77	14.53	2.64	4.16	0.09	3.74	1.20	2.07	2.77

Table 3.2: Bulk rock composition and reactive bulk rock compositions used in thermodynamic modeling.

Mineral	Solution model	Source
Cpx	Omph(GHP2)	Green et al (2007), Diener & Powell's (2011)
Opx	Opx(HP)	Holland and Powell (1998)
Epidote	Ep(HP)	Holland and Powell (1998)
Garnet	Gt(WPPH)	White et al (2005)
feldspar	feldspar	fuhrman (1988)
Chlorite	Chl(HP)	Holland and Powell (1998)
Chloritoid	Ctd(HP)	Holland and Powell (1998)
Titanite	Sp(WPC)	White et al (2002)
Amphibole	cAmph(DP2)	Deiner et al (2011)
Ilmenite	IlGkPy	
Mica	Mica(CHA)	Coggon & Holland (2002), Auzanneau et at (2010)
Biotite	Bio(HP)	Holland and Powell (1998)
Carbonate	M(HP), oCcM(HP)	Holland and Powell (1998)

Table 3.3: Mineral solution models used in thermodynamic modeling.

Mole Fraction of Major 2+ Cations in Garnet

	Garnet 1				Garnet 2			
	X_{Fe}	X_{Mn}	X_{Mg}	X_{Ca}	X_{Fe}	X_{Mn}	X_{Mg}	X_{Ca}
C1	0.731	0.013	0.043	0.213	0.733	0.029	0.028	0.210
R1	0.710	0.008	0.044	0.238	0.710	0.007	0.046	0.237
C2	0.660	0.018	0.058	0.265	0.651	0.018	0.048	0.283
R2	0.621	0.009	0.057	0.313	0.637	0.007	0.050	0.306

Table 3.4: Repersentative mole fraction of major cations found in garnet measured in the core (C1), edge of growth zone 1 (R1), beginning of growth zone 2 (C2), and garnet edge (R2).

	Garnet 1		Garnet 2		Garnet 3	
Inclusion Number	464 quartz peak	Wave shift	464 quartz peak	Wave shift	464 quartz peak	Wave shift
1	471.38	6.69	470.18	5.49	470.94	6.25
2	471.92	7.23	471.16	6.47	469.99	5.30
3	471.04	6.35	470.05	5.36	470.70	6.01
4	471.54	6.85	470.99	6.30	470.18	5.49
5	471.76	7.07	470.71	6.02	471.51	6.82
6	469.89	5.20	470.57	5.88	472.05	7.36
7	470.63	5.94	472.12	7.43	471.08	6.39
8	470.45	5.76	469.03	4.34	470.22	5.53
9	471.05	6.36	471.59	6.90	467.89	3.20
10	470.34	5.65	470.84	6.15	471.12	6.43
11	470.72	6.03	471.27	6.58	470.41	5.72
12	471.02	6.33	465.78	1.09	471.32	6.63
13	471.85	7.16	472.07	7.38	470.33	5.64
14	471.62	6.93	470.93	6.24	468.90	4.21
15	472.11	7.42	471.77	7.08	469.46	4.77
16	470.14	5.45	472.11	7.42	470.48	5.79
17	468.01	3.32				
18	470.69	6.00				
19	472.85	8.16				
20	471.26	6.57				
21	469.44	4.75				

Table 3.5: Peak shifts in quartz spectra measured via Raman spectroscopy.

	Garnet 1		Garnet 2		Garnet 3	
Inclusion Number	Ashley	Kohn	Ashley	Kohn	Ashley	Kohn
1	7510	7530	6136	6166	7005	7029
2	8133	8147	7257	7279	5919	5950
3	7120	7142	5987	6018	6730	6756
4	7695	7712	7062	7085	6136	6166
5	7948	7964	6741	6767	7660	7678
6	5805	5837	6581	6608	8283	8295
7	6650	6676	8364	8376	7166	7188
8	6444	6472	4829	4866	6295	6211
9	7131	7154	7752	7769	3545	3583
10	6318	6347	6890	6915	7211	7233
11	6753	6778	7384	7404	6398	6426
12	7097	7120	1198	1219	7441	7461
13	8052	8067	8306	8318	6307	6336
14	7787	7804	6993	7017	4682	4719
15	8353	8364	7960	7975	5316	5351
16	6090	6120	8353	8364	6478	6506
17	3680	3718				
18	6718	6744				
19	9211	9214				
20	7372	7393				
21	5294	5329				

Table 3.6: Calculated residual inclusion pressures of quartz in garnet in bars, comparing the methods of Ashley et al., (2014) and Kohn (2014).

	Garnet 1				Garnet 2				Garnet 3			
Inclusion Number	Radial fraction from core	Temp (°C)	Eosfit-Pinc	Ashley	Radial fraction from core	Temp (°C)	Eosfit-Pinc	Ashley	Radial fraction from core	Temp (°C)	Eosfit-Pinc	Ashley
1	0.88	529	1.83	1.56	0.87	531	1.58	1.50	0.85	535	1.74	1.54
2	0.79	551	1.97	1.61	0.82	543	1.80	1.56	0.96	509	1.51	1.47
3	0.53	517	1.74	1.53	0.66	525	1.54	1.49	0.86	533	1.69	1.53
4	0.75	530	1.86	1.57	0.96	509	1.72	1.52	0.74	530	1.58	1.50
5	0.77	560	1.95	1.61	0.86	534	1.69	1.53	0.57	520	1.85	1.56
6	0.72	529	1.51	1.48	0.67	526	1.65	1.52	0.63	523	1.97	1.59
7	0.05	488	1.62	1.48	0.58	520	1.98	1.59	0.44	512	1.74	1.53
8	0.11	492	1.58	1.47	0.66	525	1.34	1.44	0.54	518	1.57	1.49
9	0.65	524	1.75	1.54	0.47	514	1.85	1.55	0.70	528	1.12	1.38
10	0.66	525	1.60	1.50	0.78	552	1.74	1.56	0.45	513	1.75	1.53
11	0.78	554	1.72	1.55	0.47	514	1.78	1.54	0.47	513	1.60	1.49
12	0.61	522	1.74	1.53	0.27	501	0.71	1.25	0.54	518	1.80	1.54
13	0.69	527	1.93	1.58	0.24	499	1.95	1.56	0.40	510	1.58	1.49
14	0.77	556	1.91	1.60	0.20	497	1.69	1.50	0.14	494	1.27	1.40
15	0.72	529	1.99	1.60	0.38	508	1.89	1.56	0.24	500	1.39	1.43
16	0.49	515	1.55	1.48	0.15	494	1.95	1.56	0.15	494	1.59	1.48
17	0.27	502	1.11	1.36								
18	0.27	502	1.64	1.50								
19	0.33	505	2.13	1.61								
20	0.97	508	1.40	1.53								
21	0.45	512	1.78	1.14								

Table 3.7: Summary of quartz in garnet geobarometry results as calculated using the methods of Ashley et al., (2014) and Angel et al., (2017).

	Sample	Sm^{147}/Nd^{144}	SE (2 sigma)	Nd^{143}/Nd^{144}	SE (2 sigma)	Sm ppm	Nd ppm
Garnet core	35E core A	0.417634	0.000154	0.512631	0.000009	1.352120	1.95840
	35E core B	0.723480	0.000183	0.512732	0.000012	0.914019	0.76421
	35E gt core pdr	0.150305	0.000570	0.512564	0.000006	2.567788	10.33400
	35E core gt pdr 1	1.775309	0.008029	0.513036	0.000028	0.740704	0.25238
	35E core gt pdr 2	1.940317	0.008773	0.513093	0.000014	0.732559	0.22838
	35E core gt pdr 3	2.013777	0.000333	0.513122	0.000026	0.645634	0.19394
Garnet rim	35E rim 120HF	0.575086	0.000301	0.512589	0.000045	0.202623	0.21313
	35E Rim A	0.046380	0.000038	0.512538	0.000008	0.525526	6.85404
	35E gt Rim B	0.871635	0.000102	0.512755	0.000008	0.291728	0.20245
	35E gt rim pdr clear	0.632232	0.002678	0.512708	0.000041	0.297018	0.28418
	35E gt rim pdr dirty	0.120948	0.000023	0.512551	0.000027	1.631544	8.15982
	35E whole rock	0.104451	0.000012	0.512539	0.000006	1.972263	11.42178
	35E matrix	0.101562	0.000017	0.512543	0.000006	2.835282	16.88684

Table 3.8: Isotopic values and their associated error from $^{147}Sm/^{144}Nd$ geochronology.

Sample loss due to time in HF for garnet separates

Sample	Time in HF (mins)	Gt initial (mg)	Gt final (mg)	Sample loss (mg)	percent loss
14HSY-35E gt core 120HF	120	126.30	0	126.30	100
14HSY-35E gt core 150HF	150	124.21	0	124.21	100
14HSY-35E rim 120HF	120	124.94	3.77	121.17	96.9826
14HSY-35E gt rim 150HF	150	126.93	0	126.93	100
14HSY-35E gt core powder	NA	51.34	47.06	4.28	8.33658
14HSY-35E gt rim powder	NA	52.64	51.59	1.05	1.99468
14HSY-35E Rim A	60	84.95	4.16	80.79	95.103
14HSY-35E Core A	55	84.38	21.8	62.58	74.1645
14HSY-35E CoreB	60	83.34	5.29	78.05	93.6525

Sample loss due to amount of HF for garnet separates

Sample	Gt initial (mg)	ul of HF	mg of Gt/ul of HF	Gt Final (Mg)	% sample loss
14HSY-35E rim B	102.44	91	1.13	30.28	70.44123389
14HSY-35E rim pdr clean	95.75	24	3.99	14.73	84.61618799
14HSY-35E core pdr 1	84.72	66	1.28	14.72	82.62511804
14HSY-35E core pdr 2	81.22	81	1.00	23.71	70.80768284
14HSY-35E core pdr 3	86.35	93	0.93	20.02	76.81528662

Table 3.9: Summary of sample loss during partial dissolution of garnet

Chapter 4

Investigating the Compositional Controls on the Blueschist/Eclogite Transition

Jennifer Gorce, Besim Dragovic, Mark Caddick,

1. Department of Geoscience, Virginia Tech, Blacksburg, Virginia, 24060, USA

This work may be submitted to *Chemical Geology* for publication.

4.1 ABSTRACT

The dehydration reactions that occur at the blueschist/eclogite boundary are of critical importance because the fluid produced serves as a transportation mechanism for heat and mass and a catalyst for other reactions in the lower crust and lithospheric mantle. Though dehydration reactions are typically associated with increases in pressure and temperature, here we explore compositional controls on the blueschist/eclogite boundary. We examine the chemical differences between juxtaposed blueschist and eclogite lithologies collected from the Cycladic Blueschist Unit (CBU). Total Alkali Silica (TAS) diagrams for these rocks and a broader suite of published data reveal that eclogites generally have higher alkali contents with respect to their silica contents, compared to blueschists. Eclogites also tend to be more oxidized than blueschists.

To explore how the addition of alkalis and oxygen to a bulk rock composition affect stable mineral assemblages, we construct and contour temperature-composition (*T*-*X*) diagrams appropriate for altered basaltic rocks. We find that the addition of Na and K stabilizes white mica, omphacite, and chlorite at the expense of glaucophane, lawsonite, and garnet Increasing the ratio of ferric to ferrous iron preferentially stabilizes the acmite component of omphacite when $0 < Fe^{3+}/Fe^{2+} < 0.8$, leading to apparent 'eclogitization'. Thermodynamically constrained models predict changes in mineralogy with respect to compositional changes that are in close agreement with measured bulk rock compositions. We suggest that chemical heterogeneities acquired during initial seafloor alteration of the basaltic protolith play an important role in the absolute *P*-*T* conditions of the blueschist eclogite boundary, and could lead to significantly heterogeneous loci of the dehydration of subducting slabs, which has important geodynamic, rheological, and seismic consequences.

4.2 INTRODUCTION

The blueschist/eclogite transition is an important petrological boundary at which the subducting oceanic lithosphere metamorphoses from hydrated, amphibole bearing lithologies (blueschist) to anhydrous, clinopyroxene and garnet bearing lithologies (eclogite) (Peacock, 1993). The dehydration reactions that occur at this boundary are of critical importance because the produced fluid acts as a transportation mechanism for heat and mass and as a catalyst for other reactions in the lower crust and upper mantle. Furthermore, dehydration of subducted lithosphere leads to the densification of oceanic crust and results in the slab-pull phenomenon that drives subduction (Spence, 1987, Schellart, 2004).

While the transition from blueschist to eclogite is typically associated with changes in the Pressure-Temperature (*P*-*T*) conditions of a rock (e.g. Eskola, 1920; Peacock, 1993), studies cite differences in bulk rock composition as an important control on the precise *P*-*T* conditions of this boundary (e.g. Gao and Klemd, 2001). In China, metasomatic fluids catalyzed eclogitization of blueschist lithologies, resulting in the formation of eclogite veins enriched in Na_2O and Li and depleted in all other major and trace elements (John et al., 2008). Palin and White (2016), explored

the sampling bias of relatively young exhumed subduction lithologies, and concluded that subduction during the Archean would have never seen the blueschist/eclogite transition because Archean lithologies would have been much more Mg-rich due to hotter geotherms, thus the bulk rock composition of Archean rocks would not produce blueschist and eclogites. Instead, they would produce greenschist rocks.

Syros, Greece is known for its preservation of blueschist and eclogite lithologies from the Cycladic Blueschist Unit (CBU) which records peak metamorphic conditions at about 2.1 GPa and 550˚C (e.g. Trotet et al., 2001). In the field, blueschist and eclogites are found juxtaposed to each over short length-scales, often as eclogitic boudins in a blueschist host (Figure 4.1). It is hard to construct a tectonic model where eclogite and blueschist did not experience the same *P-T* histories. When *P-T* conditions of blueschists and eclogites from the CBU are superimposed on a metamorphic facies diagram, both plot along the blueschist/eclogite boundary (Figure 4.2).

Here, we examine the chemical differences between blueschist and eclogite lithologies found on Syros, Greece, because eclogite and blueschist can be found juxtaposed to each other, implying that they experienced the sample *P-T* conditions and thus composition must play a role recording blueschist or eclogite metamorphism. We then observe the changes in mineralogy when we subtly change the bulk rock composition of a prograde blueschist. Last, we propose explanations for heterogeneous elemental distribution in subducted basalt and speculate on the geodynamic implication of heterogeneous dehydration reactions during subduction.

4.3 GEOCHEMISTRY OF HIGH PRESSURE LITHOLOGIES ON SYROS, GREECE

4.3.1 TAS diagrams

Six hand samples from the CBU that contain centimeter scale domains of both eclogite and blueschist were selected. Eclogite and blueschist were manually separated using a rock saw and major element chemistry was determined for both domains via X-Ray Fluorescence (XRF) and Fe^{+2}/Fe^{+3} via titration wet chemistry at Franklin and Marshall College. Additional samples of blueschist and eclogite lithologies, whose field relations suggested that they experienced the same metamorphic conditions, were also analyzed for major elements. The total alkali content for each sample was plotted versus silica content on a Total Alkali Silica (TAS) diagram (Figure 4.2). Data compiled from other works (Schliestedt and Matthews, 1987; Seck et al., 1996; Miller et al., 2009;

Dragovic et al., 2012) is also included on the TAS diagram. All bulk rock data can be found in table 4.1.

Figure 4. 3 illustrates that there is a systematic chemical difference between blueschist and eclogites on Syros, Greece; eclogites have higher alkali contents with respect to their silica contents in comparison to blueschists. Most of the blueschists are derived from basalts (K_2O+Na_2O ranges from 2.9-6.5 wt%) with SiO_2 contents ranging from 44 -54 wt %. In contrast, eclogites have higher $K_2O+ Na_2O$ values (3.1-10 wt%) and a broader range (42-65 wt%) of SiO_2, plotting primarily across the trachy-basalt and basaltic trachy-andesite fields.

4.3.2 Exploring other compositional controls

We explore the contribution of additional compositional controls on the blueschist/eclogite boundary by looking for elemental trends in the major element chemistry of our eclogite and blueschist dataset (Figure 4.4). We find that there is no difference in eclogites and blueschists populations in many of the panels, with the exception of Fe_2O_3 vs. FeO (Left, middle row) and Na_2O+K_2O+CaO vs. SiO_2 (Right, top row). Eclogites tend to have higher Fe_2O_3 contents than their blueschist counterparts as well as higher alkaline contents. We explore how changing Fe^{3+}/FeOT affect the thermodynamically stable mineral assemblage in a blueschist from Syros, Greece in the section below.

Samples above are also plotted on a ternary diagram in terms of the relative proportions of alkali, total iron, and MgO content (Figure 4.5). Both blueschist and eclogite lithologies plot in a cloud of data with no discernable chemical differences between sample populations. This implies that the chemical differences that influence the *P-T* conditions of the blueschist/eclogite transition are to be found in the proportion of alkalis to silica and the degree of oxidation.

4.4 THERMODYNAMIC MODELING

4.4.1 Methods

A summary of *P-T* work done by Trotet et al., (2001), Jamie Kendall, and this study (Figure 4.2) demonstrates that on Syros, Greece, lithologies straddle the blueschist eclogite boundary and achieve similar temperatures. We focus on a blueschist sample (14CSY-20A), that has been calculated to reach peak metamorphic conditions of 2.1GPa and 550˚C (Blue arrow, Figure 4.2)

which lies on the blueschist/eclogite boundary. For a more detailed explanation on how *P-T* conditions are calculated for 14CSY-20A, see Appendix B.

Isochemical and isobaric phase diagrams are calculated to 1.) Determine the *P-T* conditions in which a prograde blueschist (Sample 14CSY-20A) reached peak metamorphic conditions (See appendix A) and 2.) To monitor how the addition of Na_2O and K_2O to the bulk rock composition affects stable mineral assemblages along the blueschist/eclogite boundary, respectively. Bulk rock composition is determined via X-Ray Fluorescence (XRF) at Franklin and Marshall College by Stanley Mertzman and associates. Fe^{+3}/Fe^{+2} was determined via titration.

Phase equilibria calculations used the Holland and Powell (1998) data set and the thermodynamic modeling software package, Perple_X, which utilizes a Gibbs free energy minimization approach (Connolly, 2005). Solution models for complex phases such as garnet, pyroxene, amphibole, etc are listed in table 3.3, from chapter 3. Modeling is done in the chemical system K_2O-MnO-MgO-CaO-Al_2O_3-FeO-Fe_2O_3-SiO_2-Na_2O-TiO_2. The sample is assumed to be saturated by an H_2O-CO_2 fluid, whose properties are described by a Compensated Redlich-Kwong (CORK) equation of state (Holland and Powell, 1991).

Two *T-X* diagrams are calculated to explore how subtle changes in bulk rock composition affect stable mineral assemblages. The first diagram (Figures 4.6) shows temperature on the y-axis and additional wt% Na_2O+K_2O added to sample 14CSY-20A on the x-axis. Na and K are added in equal proportions. For example, 1 wt% of additional alkali means that we added 0.5 wt% Na_2O and 0.5 wt% K_2O to the rock. Pressure is fixed at 2.1 GPa, which is the peak pressure calculated in Appendix B from garnet isopleths. We contour *T-X* diagrams for the amount of glaucophane and omphacite predicted to be stable in the rock for a given alkali content, since the breakdown of glaucophane to omphacite and the liberation of fluid is the major reaction controlling the blueschist/eclogite boundary. Next, we calculate the bulk rock composition, wt% SiO_2, and wt% Na_2O+K_2O, and proportions of glaucophane and omphacite per additional wt% Na_2O+K_2O and plot the results on our TAS diagram.

The second *T-X* diagram (Figure 4.7) explores how changing the ratio of ferric to ferrous iron affects the stabilities of glaucophane and omphacite. Once again, the pressure of the system is fixed at 21Kbars, and temperature is on the y-axis and composition is on the x-axis. We look at the evolving mineralogy an isothermal traverse at 550^{o}C.

4.4.2 Results

The amount of alkalis strongly influences the stability field of glaucophane because above approximately 450°C, glaucophane and omphacite isopleths are vertical., implying that the transition from an amphibole rich rock to a pyroxene rich rock is independent of temperature (Figure 4.6). For this sample at 550°C and 2.1GPa (pressure and temperature calculated from *P-T* phase diagrams in appendix B), even the small addition of approximately 3 wt% alkali content breaks down glaucophane and grows omphacite. An isothermal traverse through *T-X* diagrams at 550°C (Figure 4.7a) suggests that adding Na and K stabilizes white mica, omphacite, and chlorite at the expense of glaucophane, lawsonite, and garnet The addition of K and Na extends the stability field of chlorite dramatically. We suggest that the growth of chlorite sequesters both Mg and H_2O previously housed in lawsonite and glaucophane, while the remaining Al., Fe, and additional Na+K are partitioned into white mica and omphacite. Left over Ca from the breakdown of lawsonite goes into garnet, despite the fact that volume of garnet is reduced in the presence of additional alkalis.

Using our thermodynamic calculations, we extract the new equilibrium bulk rock composition of 14CSY-20A per additional wt% alkali (Table 4.2). The initial rock has a SiO_2 content of 48.42 wt %and a total alkali content of 4.07 wt % and is dominated by glaucophane (48 wt% glaucophane and 11 wt % omphacite) and looks like a blueschist in hand sample. With the addition of 1 wt% alkali (0.5 % Na_2O+0.5% K_2O), SiO_2 remains relatively constant, but the rock is predicted to have nearly equal proportions of glaucophane and omphacite: 29 wt % and 32 wt%, respectively. The addition of 2 wt% Na_2O stabilizes more omphacite so that it dominates the rock (56 wt % omphacite, 8% wt% glaucophane) and it looks like an eclogite in hand sample. The addition of 3 wt% Na_2O or greater completely destabilizes glaucophane and the rock only contains omphacite. When we plot the calculated bulk rock compositions on a TAS diagram (Figure 4.9a) we see that the rock compositions predicted to look like a blueschist (addition of <2% alkali) falls into the sample compositional domains as other measured blueschist bulk rock data from the CBU, while rock compositions predicted to look like eclogites (>2% alkali) fall in the same compositional domains as other measured eclogite bulk rock data from the CBU. Sample 14CSY-20A has a SiO_2 content of 48.42 wt % and a total alkali content of 4.07 wt %, and is dominated by glaucophane (it contains 48 wt% glaucophane and 11 wt % omphacite, rendering it a blueschist). Its composition can be re-normalized following addition of alkalis (Table 4.2). Addition of 1 wt% alkali (0.5 % Na_2O+0.5% K_2O) results in little change in SiO_2 content, but calculated phase

equilibria change substantially, resulting in sub-equal proportions of glaucophane and omphacite: 29 wt % and 32 wt%, respectively. The addition of 2 wt% Na_2O stabilizes more omphacite (56 wt % omphacite, 8% wt% glaucophane), forming a rock that would be classified as an eclogite. The addition of 3 wt% Na_2O or greater completely destabilizes glaucophane and the rock only contains omphacite. When the calculated bulk rock compositions are plotted on a TAS diagram (Figure 4.9a) we see that those rock compositions whose phase equilibria 'look like a blueschist' (i.e. are glaucophane dominated, as is the case for addition of <2% additional alkali) fall into the same compositional domains as other measured blueschist bulk rock data from the CBU. Conversely rock compositions whose calculated phase equilibria 'look like eclogites' (i.e. are omphacite dominated, as is the case with >2% additional alkali) fall in the same compositional domains as other measured eclogite bulk rock data from the CBU.

T-X diagrams reveal that the Fe_2O_3/FeO also acts as an important control on the *P-T* conditions of the blueschist/eclogite transition. Between approximately 450-575˚C, contours for the abundance of amphibole in sample 14CYS-20A are generally sub-vertical., implying that the degree of oxidation is a stronger control on the transition from blueschist to eclogite than temperature up to Fe^{3+}/Fe^{2+} values of 0.8. Based on an isothermal traverse at 550˚C, we propose that when $0< Fe^{3+}/Fe^{2+} <0.8$ the presence of ferric iron stabilizes the acmite component of omphacite which sequesters elements that would be used in glaucophane such as Na and Al., However, extremely oxidized conditions ($Fe^{3+}/Fe^{2+}> 0.8$) stabilize the Fe-endmember amphibole riebeckite, and destabilize clinopyroxene, and thus Fe^{3+}/Fe^{2} is not a reliable predictor for the blueschist/eclogite transition in some cases.

We also extracted the thermodynamically calculated bulk rock composition from the isobaric traverse calculated for increasing Fe^{3+}/Fe^{2+} and compared modeling results to bulk rock data compiled from the Cycladic Blueschist Unit. We used the relative abundances of amphibole and clinopyroxene as a proxy for the blueschist/eclogite transition, and colored data points in an Fe_2O_3 vs FeO plot (Figure 4.9b) to reflect what the predicted rock will look like (Blue = blueschist, green = eclogite). We find very good agreement between modeling results and bulk rock data, which suggests that the degree of oxidation of basalt is an important control on the transition from blueschist to eclogite.

4.5 DISCUSSION

4.5.1 Exploring composition

Though a substantial part of the data set demonstrates good correlation between Na_2O+K_2O/SiO_2, Fe_2O_3 and whether a sample equilibrates in the blueschist or eclogite field, there are enough data points that plot outside of this trend that further exploration is required. We propose two explanations: 1.) We have not taken into account all of the chemical differences between prograde and retrograde blueschists, 2.) Post peak metamorphic fluid alteration opened the system to chemical exchange, such as mobility of Na and K in fluid.

While the details of the metamorphic and structural evolution of the CBU has been in contention for decades, most studies will agree that the CBU experienced peak metamorphic conditions to eclogite facies around 50 Ma, retrograde blueschist metamorphism around 45Ma, and variable greenschist overprinting 30-18 Ma. Recent studies (e.g Roche et al., 2016; This work, chapter 3) have proposed that the driving mechanism for blueschist overprinting was slab rollback, which initiated exhumation of the CBU. The consequence of this is that prograde blueschists that formed during burial of the Pintos Oceanic Unit to eclogite facies coexist in the field with retrograde blueschists. Additional petrologic observations made at the thin section and micron scale are needed to differentiate the two populations.

Data from Mocek, (2001) show distinct mineral, major element, and trace element differences between blueschist and eclogites from the CBU. Blueschists, in addition to being dominated by glaucophane, contain higher abundances of garnet and episode. In contrast, eclogites contain more phengite, and more regularly contain titanite. Eclogites are elevated in alkalis while blueschists have lower alkali contents, which agrees with the data trends discussed in section 4.4.2. In terms of trace element chemistry, blueschists are enriched with respect to condrites and slightly depleted in LREE in comparision to HREE, similar to that of N-MORB which is interpreted to represent protolith tholeiitic andesites and high-Fe tholeiites. Eclogites are strongly enriched in LREE in comparison to HREE, which suggests that eclogite protoliths formed via fractional crystallization (Mocek, 2001). In both cases, eclogites and blueschists are interpreted to form during arc magmatism, though via different processes.

4.5.2 Timing of alteration of the igneous protolith

We propose that bulk rock compositional heterogeneities that influence the *P-T* conditions of the blueschist/eclogite boundary occurred during seafloor alteration of the original igneous protolith. Seafloor alteration is a very well-studied phenomenon because large-scaled redistribution of mass has important implications for elemental recycling and mass balance between the deep Earth and Earth's exterior. Studies (e.g. Staudigel et al., 1996) report that an average of 12 wt% material (primarily H_2O, CO_2, and K) is added to the upper oceanic crust during seafloor alteration, though the distribution of these elements varies widely. Bednarz and Schmincke (1989) sought to quantify elemental budgets as a function of the metasomatic regime in which a block of basalt sat. They report that low temperature alteration of basalts leads to an enrichment in alkalis, and that the degree of enrichment is highly variable across the Troodos Extrusive Series. This is consistent with our data (eclogites are enriched in alkalis) and field observations on Syros, where eclogite boudin sit in a matrix of blueschist (e. g. Trotet et al., 2001; Rosenbaum et al., 2002; Lagos et al., 2007; Behr et al.,2018)

Another possibility to consider is that chemical differences between blueschists and eclogites developed due to fluid flow during subduction. Since fluid rises buoyantly, it would be possible for deeper lithologies to dehydrate first, and any fluid released would interact and alter overlying lithologies. A study done by Miller and Cartwright (2000), used δ18O values across unmetamorphosed and metamorphosed basalts to differentiate seafloor alteration from metasomatism via subduction fluids. They concluded that seafloor alteration yields higher δ18O values than what one might expect for basalts, and both unmetamorphosed and metamorphosed pillow basalts preserved these values. However, the rims of the high pressure metamorphosed pillows contained lower δ18O values at their rims than in their cores, which is attribute to fluid/rock interactions occurring during subduction. We currently do not have δ18O values for comparison, but obtaining δ18O values for our samples would be a next logical step for future work.

4.5.3 Implications for subduction zone geodynamics

Many workers have studied the implications of slab dehydration on the geodynamics of the subducting system (e.g. Peacock, 1993; Peacock and Wang, 1999; Hacker et al., 2003; Hacker, 2013). The dehydration reactions that occur at the blueschist/eclogite boundary lead to

densification of the down going slab, which drives slab-pull (Spence, 1987; Schellart, 2004), and promotes dehydration embrittlement through pulsed fluid release, which is thought to be a component in the generation of intermediate-depth earthquakes (Davis, 1999; Hacker et al., 2003; Brown et al., 2005; Viete et al., 2018). A recent publication (Behr et al., 2018) discusses the role of heterogeneous dehydration of the subducting slab on episodic tremor and slow slip associated with the build up to megathrust ruptures. They interpret metabasic outcrops on Syros, Greece as a subduction shear zone, and point out that the difference in rheological behavior of eclogite boudins versus the blueschist matrix in which they sit serves as a major control on the deformation of the subducting slab. They propose that the brittle rupturing of one or more eclogite pods is the source of episodic tremors events. This implies that the subducting slab does not experience a single pulse of eclogitization (and subsequent fluid release) at a fixed depth, but instead dehydrates sporadically across any one slab. A substantially altered section of oceanic crust has the potential to see eclogitization at much shallower depths.

4.6 CONCLUSIONS

We examine the chemical differences between juxtaposed blueschist and eclogite lithologies, collected from the CBU. Compiled bulk rock data from several studies reveal that eclogites have higher alkali contents with respect to their silica contents. Constructed *T-X* diagrams that explore how the addition of Na and K affects mineral phase equilibria along the blueschist/eclogite transition reveal that white mica, omphacite, and chlorite grow at the expense of glaucophane, lawsonite, and garnet Thermodynamic calculations for the XRF compositions of eclogite and blueschist rocks yield omphacite and glaucophane dominated assemblages, respectively, at appropriate *P-T* conditions. Synthetic modification of the bulk composition of blueschist rocks such that they stabilize substantial omphacite results in rock compositions that overlap with eclogites on TAS diagrams.

Our results suggest that chemical heterogeneities acquired during initial seafloor alteration of the basaltic protolith, especially the enrichment of alkalis, play an important role in the absolute *P-T* conditions of the blueschist eclogite boundary, and thus influence the *P-T* conditions in which dehydration reactions occur during subduction of altered oceanic material., Because alteration of MORB is highly variable throughout the oceanic lithosphere, this would imply that dehydration

of the subducted slab is heterogeneous, which has important implications for the geodynamic, rheological., and seismic behavior of the subducting slab.

4.7 REFERENCES

Auzanneau, E., Schmidt, M., Vielzeuf, D., and Connolly, J., 2009, Titanium in phengite: a geobarometer for high temperature eclogites: Contributions to Mineralogy and Petrology, v. 159, no. 1, p. 1–24, doi: 10.1007/s00410-009-0412-7.

Bednarz, U., and Schmincke, H., 1989, Mass transfer during sub-seafloor alteration of the upper Troodos crust (Cyprus): Contributions to Mineralogy and Petrology, v. 102, no. 1, p. 93–101, doi: 10.1007/BF01160193.

Behr, W., Kotowski, A., and Ashley, K. Dehydration-induced rheological heterogeneity and the deep tremor source in warm subduction zones: Geology, doi: 10.1130/G40105.1.

Brown, K., Tryon, M., DeShon, H., Dorman, L., and Schwartz, S., 2005, Correlated transient fluid pulsing and seismic tremor in the Costa Rica subduction zone: Earth and Planetary Science Letters, v. 238, no. 1-2, p. 189–203, doi: 10.1016/j.epsl.2005.06.055.

Coggon, R., and Holland, T., 2002, Mixing properties of phengitic micas and revised garnet-phengite thermobarometers: Journal of Metamorphic Geology, v. 20, no. 7, p. 683–696, doi: 10.1046/j.1525-1314.2002.00395.x.

Connolly, J.A.D., 2005, Computation of phase equilibria by linear programming: A tool for geodynamic modeling and its application to subduction zone decarbonation: Earth and Planetary Science Letters, v. 236, no. 1-2, doi: 10.1016/j.epsl.2005.04.033.

Davies, J., 1999, The role of hydraulic fractures and intermediate-depth earthquakes in generating subduction-zone magmatism: Nature, v. 398, no. 6723, p. 18202, doi: 10.1038/18202.

Deiner, and Powell, 2012, Revised activity–composition models for clinopyroxene and amphibole: Journal of Metamorphic Geology, v. 30, no. 2, p. 131–142, doi: 10.1111/j.1525-1314.2011.00959.x.

Deiner, J., Powell, R., and White, R., 2008, Quantitative phase petrology of cordierite–orthoamphibole gneisses and related rocks: Journal of Metamorphic Geology, v. 26, no. 8, p. 795–814, doi: 10.1111/j.1525-1314.2008.00791.x.

Deiner, J., Powell, R., White, R., and Holland, T., 2007, A new thermodynamic model for clino- and orthoamphiboles in the system Na2O–CaO–FeO–MgO–Al2O3–SiO2–H2O–O: Journal of Metamorphic Geology, v. 25, no. 6, p. 631–656, doi: 10.1111/j.1525-1314.2007.00720.x.

Dragovic, B., Samanta, L., Baxter, E., and Selverstone, J., 2012, Using garnet to constrain the duration and rate of water-releasing metamorphic reactions during subduction: An example from Sifnos, Greece: Chemical Geology, v. 314, p. 9–22, doi: 10.1016/j.chemgeo.2012.04.016.

Eskola, P., 1920, The mineral facies of rocks.

Fuhrman, ML, and Lindsley, DH, 1988, Ternary-feldspar modeling and thermometry: American Mineralogist, v. 73, no. 3-4, p. 201-215.

Green, E., Holland, T., and Powell, R., 2007, An order-disorder model for omphacitic pyroxenes in the system jadeite-diopside-hedenbergite-acmite, with applications to eclogitic rocks: American Mineralogist, v. 92, no. 7, p. 1181–1189, doi: 10.2138/am.2007.2401.

Hacker, B., Abers, G., and Peacock, S., 2003, Subduction factory 1. Theoretical mineralogy, densities, seismic wave speeds, and H2O contents: Journal of Geophysical Research: Solid Earth (1978–2012), v. 108, no. B1, doi: 10.1029/2001JB001127.

Hacker, B., Peacock, S., Abers, G., and Holloway, S., 2013, Subduction factory 2. Are intermediate-depth earthquakes in subducting slabs linked to metamorphic dehydration reactions?: Journal of Geophysical Research: Solid Earth (1978–2012), v. 108, no. B1, doi: 10.1029/2001JB001129.

Holland, T, and Powell, R, 1991, A Compensated-Redlich-Kwong (CORK) equationn for volumes and fugacities of CO2 and H2O in the range 1 bar to 50 kbar and 100–1600 C: Contributions to Mineralogy and Petrology, v. 109, no. 2, p. 265-273, doi: 10.1007/BF00306484.

Holland, T., and Powell, R., 1998, An internally consistent thermodynamic data set for phases of petrological interest: Journal of Metamorphic Geology, v. 16, no. 3, p. 309–343, doi: 10.1111/j.1525-1314.1998.00140.x.

Hollister, L., 1966, Garnet zoning: an interpretation based on the Rayleigh fractionation model: Science, V. 154, No. 3757, p. 1647-1651 doi: 10.1126/science.154.3757.1647.

Gao, J. and Klemd, R. 2001, "Primary fluids entrapped at blueschist to eclogite transition: evidence from the Tianshan meta-subduction complex in northwestern China", Contributions to Mineralogy and Petrology, vol. 142, no. 1, p. 1-14. Doi: 10.1007/s004100100275

John, T., Klemd, R., Gao, J. and Garbe-Schönberg, C. 2008, "Trace-element mobilization in slabs due to non steady-state fluid–rock interaction: Constraints from an eclogite-facies transport vein in blueschist (Tianshan, China)", LITHOS, vol. 103, no. 1, p. 1-24, doi; 10.1016/j.lithos.2007.09.005

Lagos, M., E. E. Scherer, F. Tomaschek, C. Münker, M. Keiter, J. Berndt, and C. Ballhaus (2007), High precision Lu–Hf geochronology of Eocene eclogite-facies rocks from Syros, Cyclades, Greece, Chem. Geol., 243(1–2), 16–35, doi:10.1016/j.chemgeo.2007.04.008.

Miller, M., and Cartwright, C., 2000, Distinguishing between seafloor alteration and fluid flow during subduction using stable isotope geochemistry: examples from Tethyan ophiolites in the Western Alps: Journal of Metamorphic Geology, v. 18, no. 5, p. 467–482, doi: 10.1046/j.1525-1314.2000.00274.x.

Miller, D., Marschall, H., and Schumacher, J., 2009, Metasomatic formation and petrology of blueschist-facies hybrid rocks from Syros (Greece): Implications for reactions at the slab–mantle interface: Lithos, v. 107, no. 1-2, p. 53–67, doi: 10.1016/j.lithos.2008.07.015.

Mocek, B. 2001, "Geochemical evidence for arc-type volcanism in the Aegean Sea: the blueschist unit of Siphnos, Cyclades (Greece)", LITHOS, vol. 57, no. 4, pp. 263-289, doi; 10.1016/S0024-4937(01)00043-3

Palin, R., and White, R., 2015, Emergence of blueschists on Earth linked to secular changes in oceanic crust composition: Nature Geoscience, v. 9, no. 1, p. 60–64, doi: 10.1038/ngeo2605.

Peacock, S., 1993, The importance of blueschist→ eclogite dehydration reactions in subducting oceanic crust: Geological Society of America Bulletin, v. 105, p. 684-694, doi: 10.1130/0016-7606(1993)105<0684:TIOBED>2.3.CO;2.

Peacock, S., and Wang, K., 1999, Seismic Consequences of Warm Versus Cool Subduction Metamorphism: Examples from Southwest and Northeast Japan: Science, v. 286, no. 5441, p. 937–939, doi: 10.1126/science.286.5441.937.

Roche, V., Laurent, V,. Cardello, G. L., Jolivet, L., Scaillet, S., Anatomy of the Cycladic Blueschist Unit on Sifnos Island (Cyclades, Greece): Journal of Geophysics, v. 97, p. 62-87, doi: 10.1016/j.jog.2016.03.008

Rosenbaum, G., Avigad, D., and Sánchez-Gómez, M., 2002, Coaxial flattening at deep levels of orogenic belts: evidence from blueschists and eclogites on Syros and Sifnos (Cyclades, Greece): Journal of Structural Geology, v. 24, no. 9, p. 1451–1462, doi: 10.1016/S0191-8141(01)00143-2.

Schellart, W., 2004, Quantifying the net slab pull force as a driving mechanism for plate tectonics: Geophysical Research Letters, v. 31, no. 7, doi: 10.1029/2004GL019528.

Schliestedt, M. & Matthews, A. 1987, "Transformation of blueschist to greenschist facies rocks as a consequence of fluid infiltration, Sifnos (Cyclades), Greece", Contributions to Mineralogy and Petrology, vol. 97, no. 2, pp. 237-250, doi: 10.1007/BF00371243

Seck, A., H., Kotz, J., Seidel, E., Stosch, H. G., 1996; Geochemistry of a meta-ophiolite suite: An association of metagabbros, eclogites and glaucophanites on the island of Syros, Greece, 1996, European Journal of Mineralogy, v. 8, no. 3, p. 607624, doi: 10.1127/ejm/8/3/0607.

Smye, A., Greenwood, L., and Holland, T., 2010, Garnet–chloritoid–kyanite assemblages: eclogite facies indicators of subduction constraints in orogenic belts: Journal of Metamorphic Geology, v. 28, no. 7, p. 753–768, doi: 10.1111/j.1525-1314.2010.00889.x.

Spence, W, 1987, Slab pull and the seismotectonics of subducting lithosphere: Reviews of Geophysics, v. 25, no, 1, p. 55-69, doi: 10.1029/RG025i001p00055.

Staudigel, H, Plank, T, White, B., Schmincke, H., U., 1996, Geochemical fluxes during seafloor alteration of the basaltic upper oceanic crust: DSDP Sites 417 and 418, Subduction Top to Bottom, p. 19-36

Trotet, F., Jolivet, L., and Vidal, O., 2001, Tectono-metamorphic evolution of Syros and Sifnos islands (Cyclades, Greece): Tectonophysics, v. 338, no. 2, p. 179–206, doi: 10.1016/S0040-1951(01)00138-X.

Trotet, F., Vidal, O., and Jolivet, L., 2001, Exhumation of Syros and Sifnos metamorphic rocks (Cyclades, Greece). New constraints on the *P-T* paths: European Journal of Mineralogy, v. 13, no. 5, p. 901920, doi: 10.1127/0935-1221/2001/0013-0901.

Viete, D. R., Hermann, J., Lister, G., S., Stenhouse, I. R., 2011, The nature and origin of the Barrovian metamorphism, Scotland: diffusion length scales in garnet and inferred thermal time scales: Journal of the Geological Society, v. 168, no. 1, p. 115-132, doi: 10.1144/0016-76492009-087

White, R., Pomroy, N., and Powell, R., 2005, An in situ metatexite–diatexite transition in upper amphibolite facies rocks from Broken Hill, Australia: Journal of Metamorphic Geology, v. 23, no. 7, p. 579–602, doi: 10.1111/j.1525-1314.2005.00597.x.

White, R., Powell, R., and Clarke, G., 2002, The interpretation of reaction textures in Fe-rich metapelitic granulites of the Musgrave Block, central Australia: constraints from mineral equilibria calculations in the system K2O–FeO–MgO–Al2O3–SiO2–H2O–TiO2–Fe2O3: Journal of Metamorphic Geology, v. 20, no. 1, p. 41–55, doi: 10.1046/j.0263-4929.2001.00349.x.

4.8 FIGURES

Figure 4.1: Eclogite boudin sitting in a blueschist host on the island of Syros, Greece.

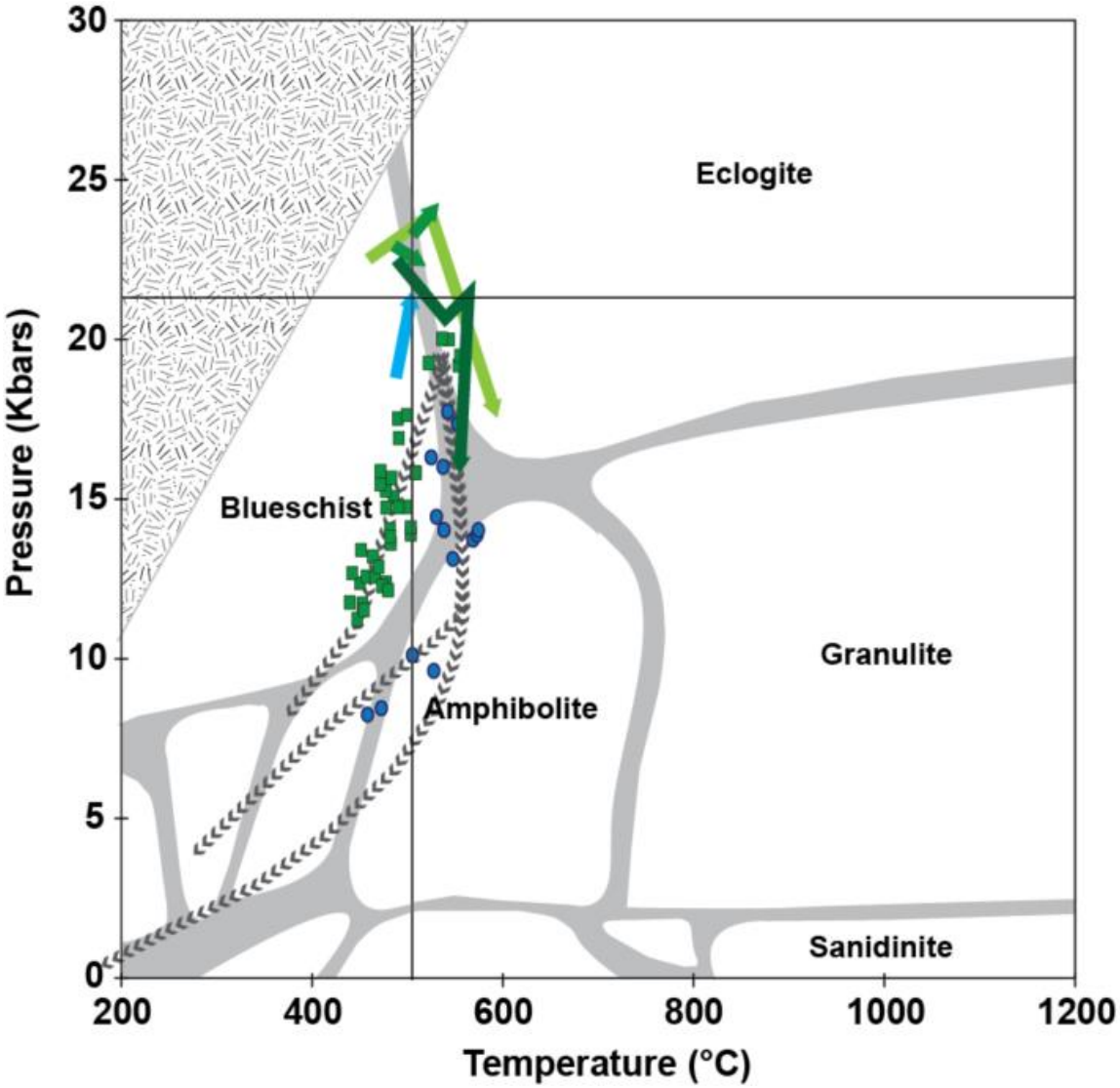

Figure 4.2: *P-T* condition of eclogite (green) and blueschist (blue) from Syros, Greece,that have been superimposed on a metamorphic facies diagram. Data is taken from Trotet et al., (2001b), work done by Jamie Kendall in her thesis, and this study.

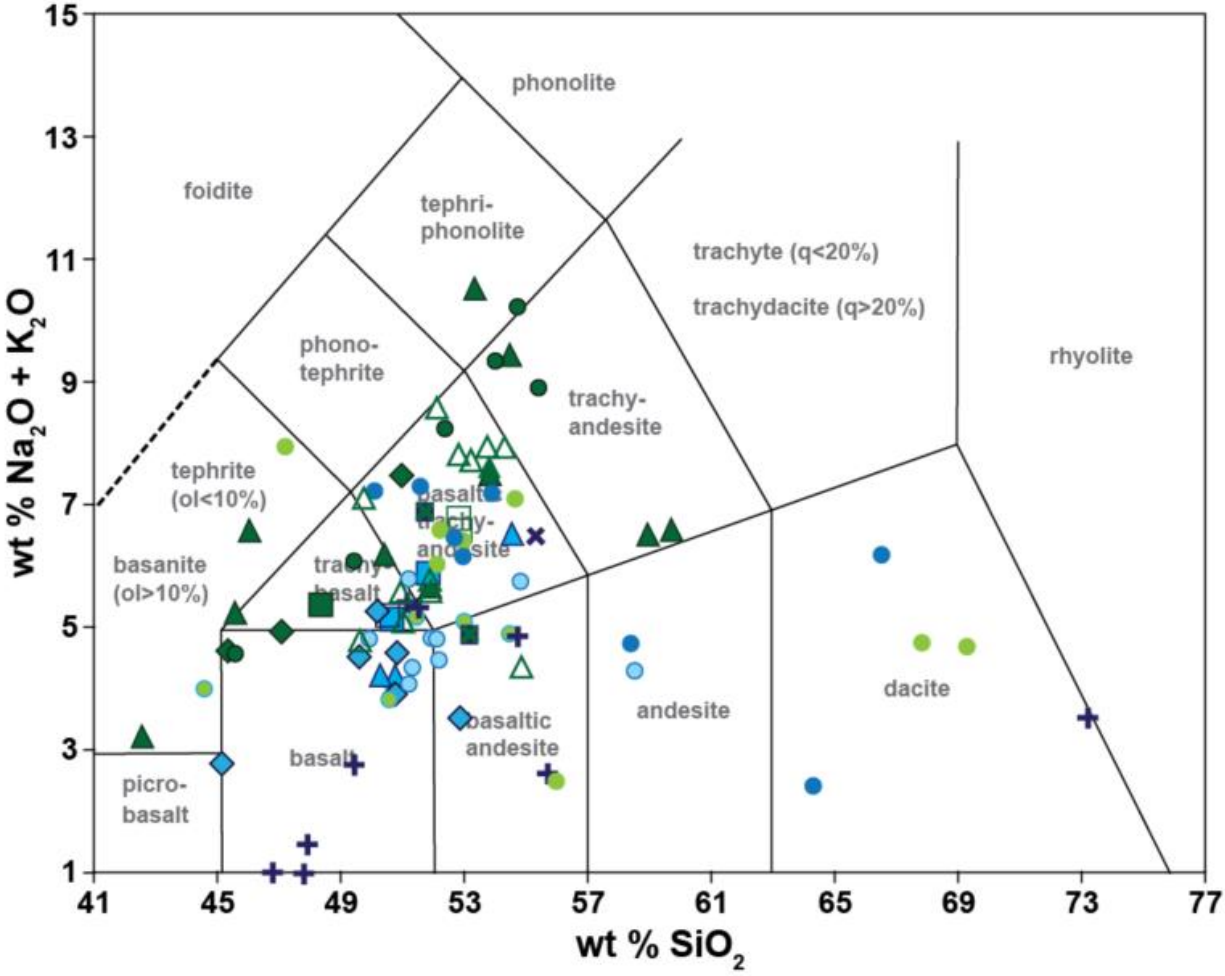

Figure 4.3: Total Alkali Silica (TAS) diagram of bulk rock data compiled from the literature on metabasic lithologies from the Cycladic Blueschist Unit. Samples identified as eclogites are in green and samples identified as blueschist are in blue. Symbols represent source material.

● = Brockers and Enders (2001), ■ = Miller et al., (2009), ◆ = Seck et al., (1996) ▲ = This study part I, ● = This study part II, ✖ = Dragovic et al., (2012), ✚ = Schiestedt and Matthews (1987), Δ = Mocek (2001), □ = Besim Dragovic

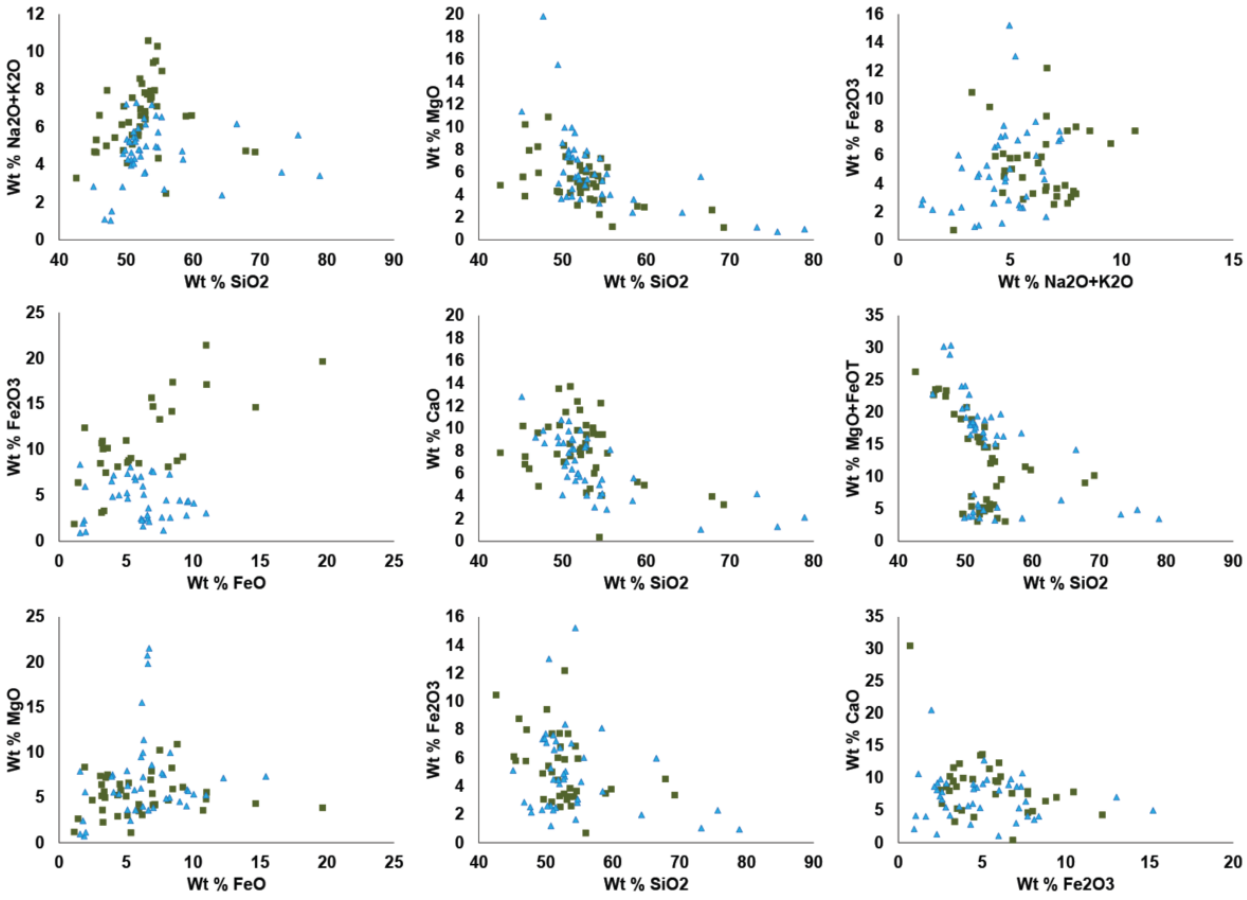

Figure 4.4: Bulk rock data from the same compilation as figure 4.2 plotted to explore potential compositional trends between blueschist (Blue data points) and eclogite (Green data points) populations.

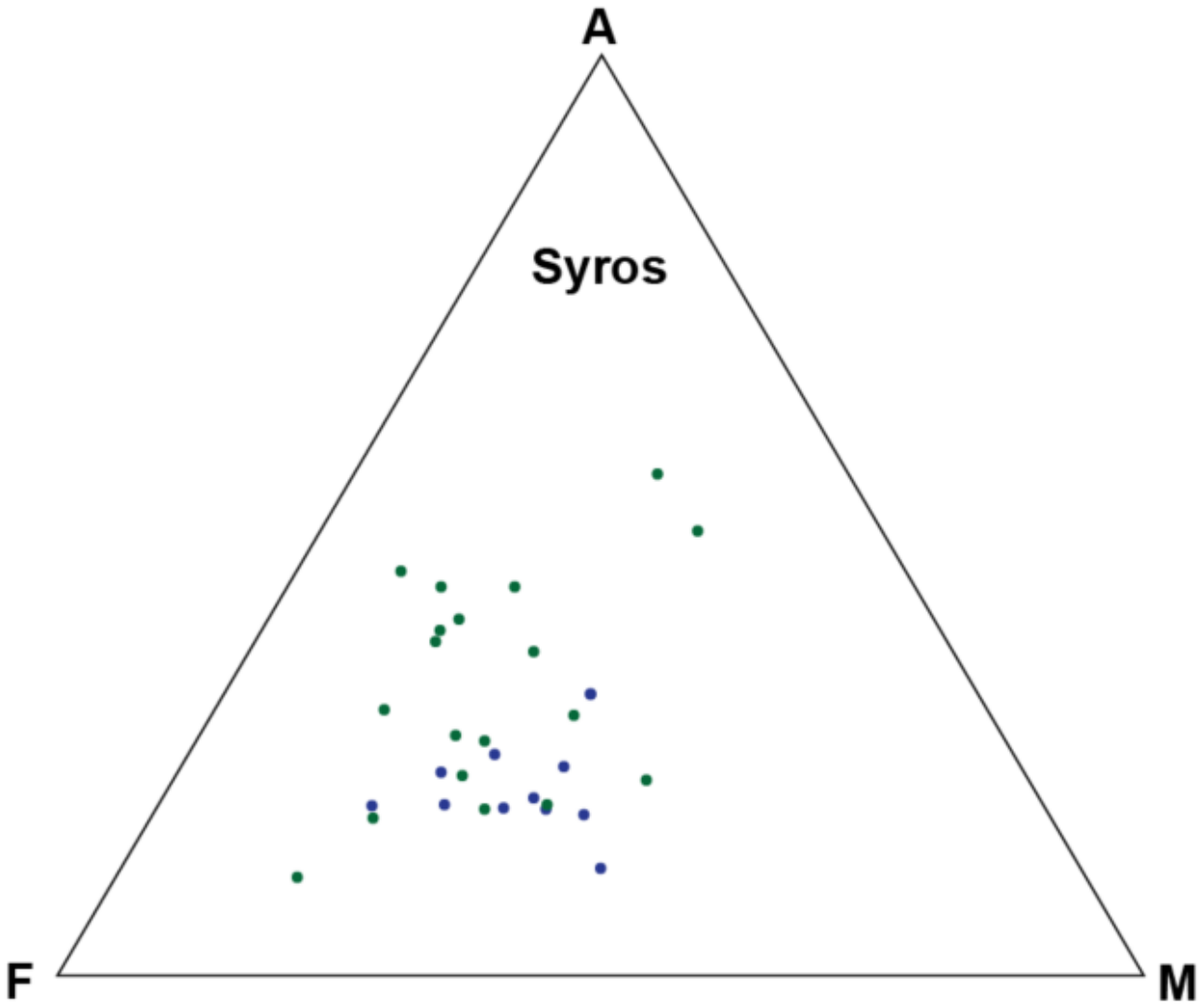

Figure 4.5: Bulk rock data from the same compilation as figure 4.2 plotted in terms of the alkali, total iron, and MgO content. Blueschists are in blue, eclogites are in green.

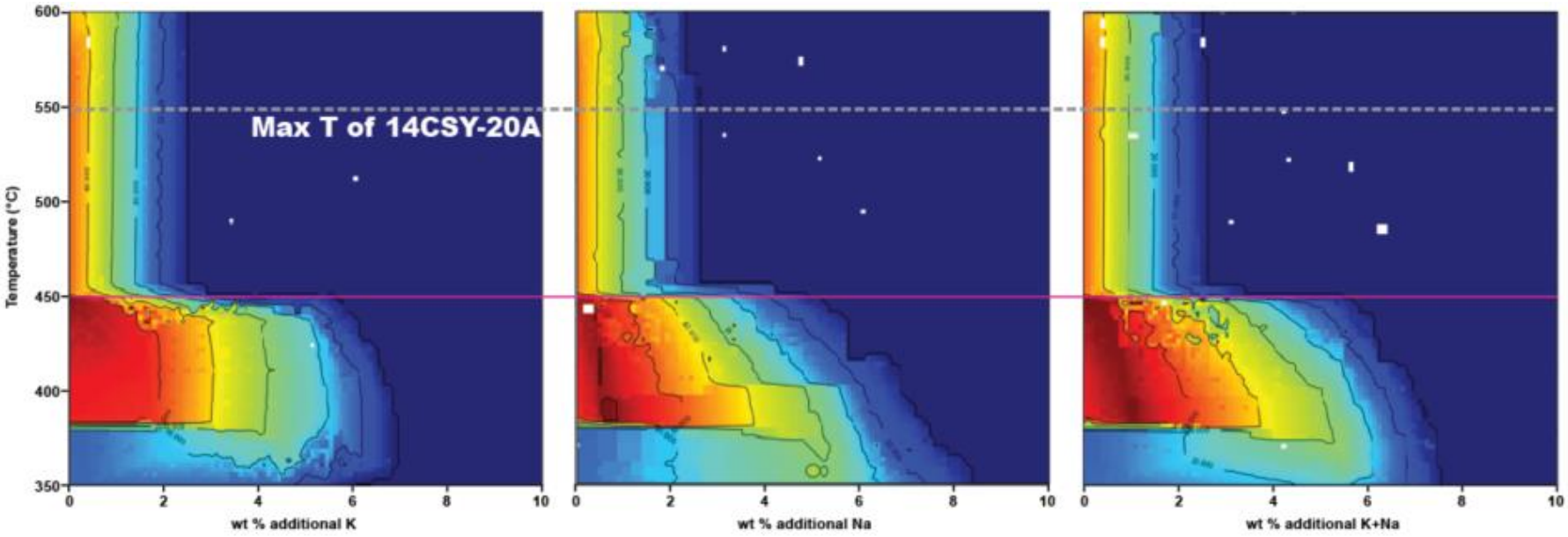

Figure 4.6.: *T-X* diagrams contours for the amount of glaucophane calculated to be thermodynamically stable in sample 14CSY-20A as a function of temperature (Y-axis), and addition of alkalis (X-axis) (left = added K, middle = added Na, Right = K+Na). Above 450°C (pink line) the abundance of glaucophane is compositionally controlled. The grey dashed line is th maximum temperature calculated for 14CSY-20A.

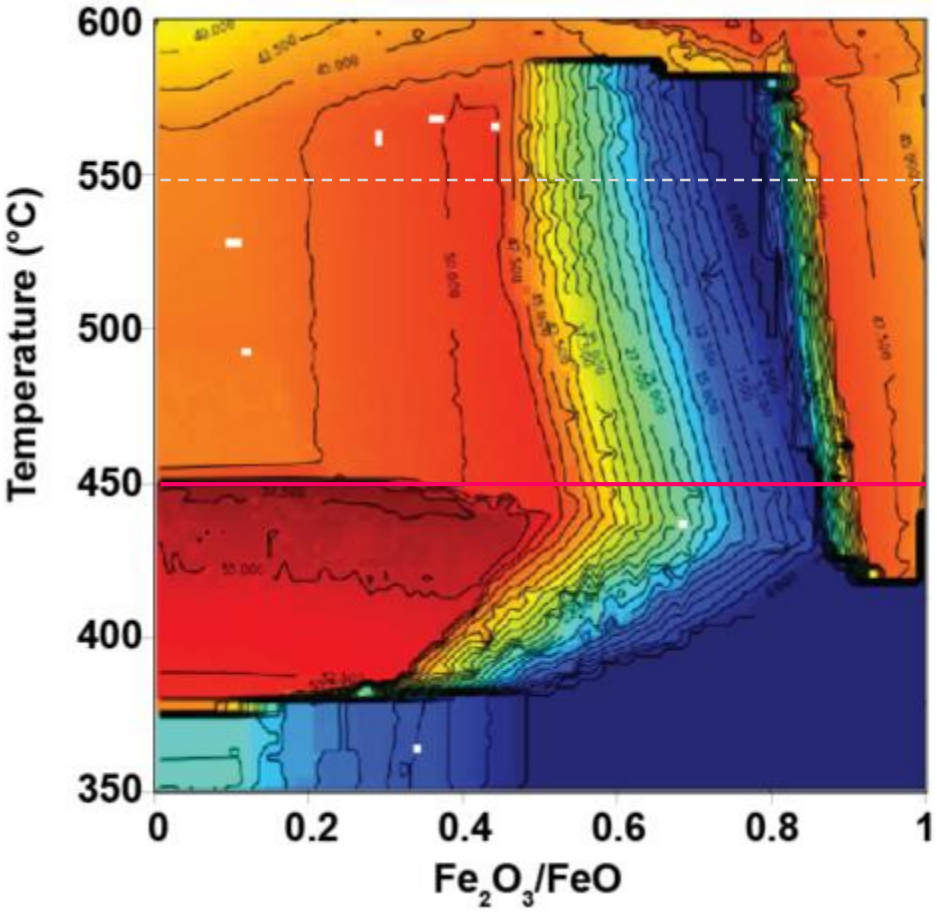

Figure 4.7.: *T-X* diagrams contours for the amount of glaucophane calculated to be thermodynamically stable in sample 14CSY-20A as a function of temperature (Y-axis), and the ratio of ferric to ferrous iron (X-axis). Above 450ºC (pink line) the abundance of glaucophane is compositionally controlled. The grey dashed line is the maximum temperature calculated for 14CSY-20A.

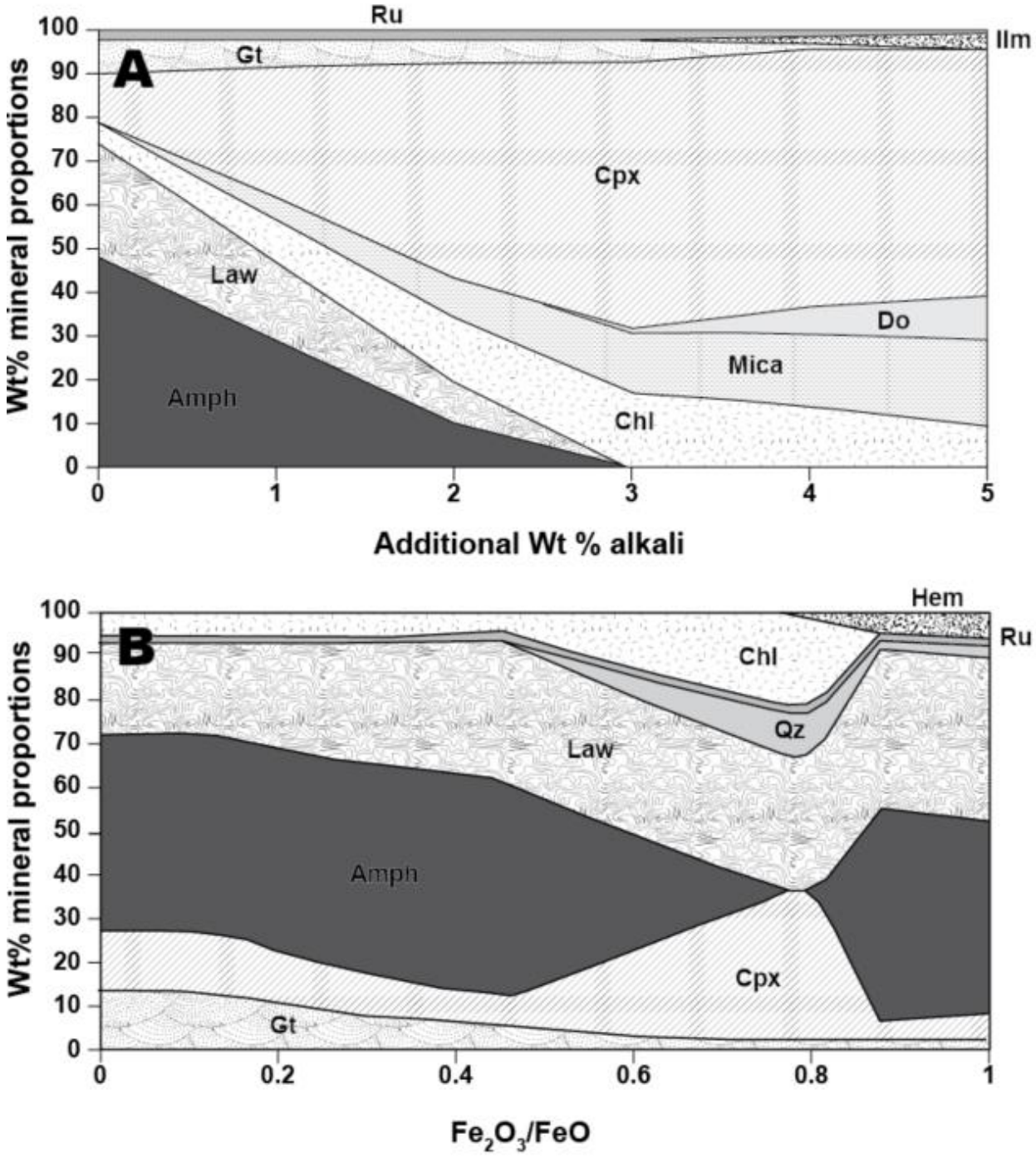

Figure 4.8: A: Diagram illustrating the predicted mineral evolution of a blueschist along an isothermal traverse as a function of additional alkalis added to the rock. B: Diagram illustrating the predicted mineral evolution of a blueschist along an isothermal traverse as a function of increasing the ferric/ferrous ratio.

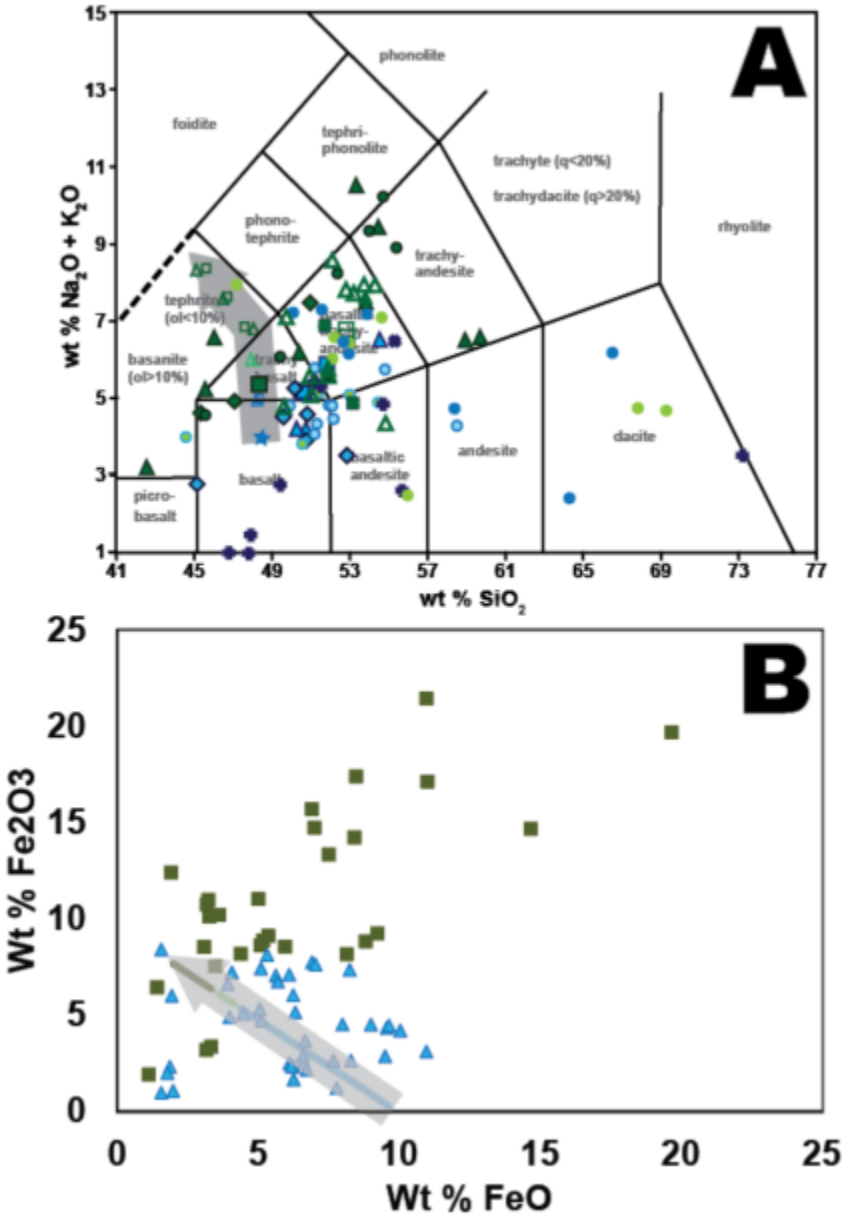

Figure 4.9: A: Comparison of modeling results with measure bulk rock data on a TAS diagram B: Comparison of modeling results with measure bulk rock data as a function of increasing the ferric/ferrous ratio.

Study	Brocker and Enders 2001						Miller et al 2009			Seck et al 1996									This study	
Location	Tinos		Syros				Syros			Syros									Syros	
Rock type	Eclogite	Eclogite	Eclogite	Eclogite	Eclogite	Eclogite	Blueschist	Blueschist	Eclogite	Eclogite	Eclogite	Eclogite	Blueschist	Blueschist	Blueschist	Blueschist	Blueschist	Blueschist	Blueschist	Blueschist
Weight %																				
SiO2	49.39	44.88	54.55	51.75	53.13	53.02	50.17	49.33	46.57	45.07	50.01	46.34	49.64	44.16	51.69	48.12	48.23	48.86	48.9	49.51
TiO2	1.47	2.78	0.71	1.98	1.04	0.27	1.29	1.52	1.4	4.51	0.85	2.38	1.18	1.48	2.2	3.21	2.79	1.36	1.96	1.1
Al2O3	15.73	15.74	17.2	13.34	15.74	21.38	14.87	13.6	14.26	12.28	13.42	12.94	15.54	14.45	16.1	12.7	13.11	15.3	16.28	16.32
FeOT	14.67	19.39	3.12	9.13	8.01	3.24	11.88	15.05	8.5											
Fe2O3										6.08	7.59	5.71	5.17	5.01	4.59	7.12	6.81	1.15	2.52	2.57
FeO										10.96	6.87	8.29	4.95	6.18	5	8.01	5.87	7.49	7.39	8.17
MnO	0.57	0.65	0.07	0.17	0.11	0.07	0.17	0.22	0.15	0.24	0.5	0.3	0.11	0.11	0.17	0.19	0.1	0.1	0.2	0.19
MgO	4.34	3.83	6.35	6.08	4.63	5.08	6.93	7.15	10.52	5.56	4.1	8.15	7.78	11.14	6.18	4.86	5.79	7.25	7.43	9.81
CaO	7.74	6.73	7.68	8.21	6.42	3.92	5.8	5.6	9.77	10.18	7.42	9.45	9.57	12.53	8.36	8.46	8.39	10.25	7.56	6.61
Na2O	6.05	4.56	5.22	6.67	6.44	4.05	4.65	4.82	5.22	4.66	7.1	4.89	3.58	2.57	2.88	4.31	4.61	4.27	4.06	4.15
K2O	0.09	0.03	3.63	1.55	2.84	5.94	1.11	0.25	0.03	0.01	0.33	0.04	0.3	0.21	0.65	0.15	0.54	0.2	0.051	0.08
P2O5	0.01	0.03	0.01	0.01	0.01	0	0.15	0.11	0.03	0.32	0.06	0.1	0.24	0.09	0.18	0.58	0.06	0.22	0.28	0.11
CO2										0.15	0.21	0.17	0.16	0.46	0.07	0.12	0.16	0.87		
H2O										0.4	0.77	1.91	2.63	2.02	2.73	1.99	1.91	2.33		
L.O.I.	0.12	1.16	1.88	1.3	1.82	3.26	2.03	1.69	3.17										3.04	3.89
SUM	100.05	98.59	98.53	98.88	98.36	96.97	96.87	97.54	96.42	99.55	98.19	98.49	97.82	97.84	97.82	97.13	96.24	96.23	96.35	98.51

Study	This study												This study, part II							
Location	Syros												Syros							
Rock type	Blueschist	Blueschist	Eclogite	Eclogite	Eclogite	Eclogite	Eclogite	Eclogite	Eclogite	Eclogite	Eclogite	Eclogite	Eclogite	Eclogite	Eclogite	Eclogite	Eclogite	Eclogite	Eclogite	Eclogite
Weight %																				
SiO2	53.84	52.29	58.59	59.64	52.93	51.28	52.7	41.56	45.43	52.76	44.95	50.19	54.1	51.58	46.15	49.44	52.24	51.85	55.75	67.26
TiO2	1.63	1.66	0.8	0.79	1.02	0.29	1.11	3.44	5.64	1.28	2.85	1.09	0.65	0.61	1.39	1.00	0.98	1.15	0.12	0.91
Al2O3	17.65	15.96	16.59	16.59	19.03	13.13	21.44	15.73	11.15	15.18	14.74	14.6	10.87	14.36	15.35	17.44	12.94	16.91	7.72	13.69
FeOT																				
Fe2O3	1.62	4.99	3.49	3.77	2.56	5.96	6.62	10.22	8.67	7.65	5.73	5.42	3.62	3.27	7.85	9.3	5.84	6.75	0.69	4.47
FeO	6.19	4.41	5.06	4.37	5.86	4.95	3.16	10.71	6.82	3.2	7.41	3.07	3.44	5.13	8.30	1.88	3.58	3.16	1.12	1.40
MnO	0.15	0.16	0.12	0.11	0.14	0.3	0.04	0.36	0.28	0.19	0.25	0.22	0.11	0.06	0.45	0.25	0.16	0.18	0.16	0.12
MgO	7.19	5.32	2.98	2.92	3.48	5.09	2.19	4.73	7.84	3.59	10.11	7.36	7.16	6.56	5.83	8.25	7.44	5.17	1.18	2.63
CaO	4.01	9.01	5.24	4.98	5.94	12.28	0.37	7.66	8.34	4.63	7.42	11.41	12.14	11.53	4.78	6.94	9.33	7.61	30.40	3.93
Na2O	3.85	4.71	3.6	3.61	3.75	5.61	1.29	3.17	6.39	10.49	5.25	5.99	6.29	3.88	7.77	1.31	3.74	5.02	2.37	1.59
K2O	2.69	0.22	2.95	3	3.72	0.1	7.93	0.05	0.16	0.003	0.008	0.25	0.75	2.09	0.02	2.73	2.60	1.55	0.10	3.11
P2O5	0.28	0.28	0.03	0.03	0.42	0.05	0.14	0.04	0.11	0.68	0.02	0.12	0.07	0.22	0.97	0.03	0.10	0.10	0.07	0.40
CO2																				
H2O																				
L.O.I.	3.15	1.57	3.61	3.61	2.60	0.89	3.14	1.49	2.93	0.95	4.08	1.76	1.12	3.08	2.75	3.47	2.23	5.25	18.41	2.52
SUM	98.82	98.73	99.42	99.78	98.43	98.99	96.85	97.63	98.72	98.98	98.72	99.60	99.12692024	99.06589204	97.8829182	98.5444636	98.84972768	99.348401	99.61616988	99.11027444

Table 4.1: Compilation of bulk rock data plotted on TAS diagrams.

Study	This study: Part II											Dragovic et al 2	Schliestedt and Matthews (1987)							
Location	Syros											Sifnos	Sifnos							
Rock type	Eclogite	Ec+Bs	Ec+Bs	Blueschist	Blueschist	Blueschist	Blueschist	Blueschist	Blueschist	Blueschist	Blueschist	Blueschist	Blueschist	Blueschist	Blueschist	Blueschist	Blueschist	Blueschist	Blueschist	Blueschist
Weight %																				
SiO2	68.72	51.22	49.52	53.41	50.66	48.70	52.29	64.13	65.89	57.49	52.05	53.15	74.4	78	71.2	51.7	48.5	47.5	54.6	46.5
TiO2	1.03	1.54	2.26	1.06	1.41	1.56	1.00	0.22	0.37	1.68	1.56	1.07	0.25	0.17	0.23	1.17	0.66	0.65	1.16	0.72
Al2O3	11.68	16.89	15.31	16.2	17.02	13.21	17.59	5.98	12.18	15.14	17.10	13.77	12	11.7	14.1	16.1	16	14.7	15.4	12.7
FeOT																				
Fe2O3	3.34	4.01	6.42	6.98	7.08	7.52	8.29	1.97	5.93	7.99	4.82	4.15	2.26	0.93	1.01	2.68	2.34	2.15	5.9	2.19
FeO	5.32	4.67	4.62	5.58	4.00	6.73	1.55	1.77	1.92	5.24	3.93	9.19	1.84	1.55	1.93	8.98	5.76	5.81	6.12	5.81
MnO	0.17	0.15	0.16	0.04	0.18	0.26	0.20	0.34	0.06	0.34	0.16	0.14	0.08	0.05	0.07	0.15	0.15	0.15	0.32	0.13
MgO	1.10	6.54	5.65	5.79	5.49	8.38	7.81	2.42	5.55	2.40	7.44	5.65	0.72	0.95	1.11	3.84	8.95	9.26	3.94	14.6
CaO	3.23	8.04	9.87	3.01	5.28	4.00	4.03	20.51	1.04	3.54	5.34	2.72	1.28	2.1	4.08	5.19	6.77	7.61	7.96	8.71
Na2O	4.55	4.75	4.59	6.16	3.63	6.98	3.39	2.33	4.07	4.52	4.70	5.3	5.17	0.83	1.32	4.34	4.71	4.72	2.08	1.45
K2O	0.09	1.20	0.64	0.97	3.54	0.05	2.69	0.05	2.05	0.13	1.70	0.99	0.31	2.55	2.18	0.32	0.39	0.36	0.56	1.21
P2O5	0.33	0.19	0.36	0.08	0.53	1.37	0.04	0.13	0.20	0.43	0.19	0.09	0.04	0.02	0.03	0.15	0.17	0.12	0.06	0.26
CO2													0.6	0.1	1.2	2.8	2.6	3.5	0.25	1.2
H2O													0.8	1.7	2.3	2.3	4.1	3.9	2.2	4.6
L.O.I.	1.07	2.36	2.03	2.76	5.50	2.81	3.61	13.74	2.57	1.82	2.89	1.45								
SUM	99.22509768	99.01249452	99.03514584	99.20279096	98.29165616	97.39166304	98.83692508	99.71564444	99.05670636	98.47432948	98.79670264	96.13	98.31	98.83	97.23	94.47	94.23	92.91	98.04	94.02

Study	Schliestedt and Matthews (1987)			Contributed by Besim Dragovic											Mocek 2001				
Location	Sifnos			Sifnos											Sifnos				
Rock type	Blueschist	Blueschist	Blueschist	Blueschist overprint	Blueschist	Blueschist overprint	Blueschist	Blueschist overprint	Blueschist	BS/EC	BS/EC	Eclogite	Eclogite	quartz jadeite gneiss	jadeite gneiss	Blueschist	Blueschist	Blueschist	Blueschist	Blueschist
Weight %																				
SiO2	45	44.9	44.2	49.53	54.57	52.4	50.76	44.61	50.53	53.26	51.54	52.57	53.02	74.31	64.49	50.9	49.8	50.1	50.3	56.9
TiO2	0.65	0.65	0.73	1.12	2.04	0.815	0.77	1.11	1.19	2.09	1.37	0.65	1.15	0.25	0.62	1.93	0.8	2.23	1.84	0.95
Al2O3	11	10	11.1	17.51	14.57	18.43	16.6	15.49	18.84	16.31	15.49	14.31	18	13.11	15.39	15.3	16.2	15.4	14.9	16.1
FeOT				**11.93**	**15.26**	**12.35**	**9.16**	**13.32**	**13.04**	**15.05**	**13.12**	**8.5**	**12.23**	**3.56**	**5.69**					
Fe2O3	2.38	2.02	2.71													4.08	6.4	7.46	4.31	3.54
FeO	6.25	6.3	6.22													9.82	3.81	6.89	9.35	6.48
MnO	0.12	0.16	0.16	0.16	0.27	0.184	0.16	0.18	0.23	0.59	0.06	0.25	0.13	0.10	0.1	0.22	0.12	0.2	0.2	0.18
MgO	18.7	20.2	19.6	4.95	3.26	3.9	7.91	5.2	3.84	3.7	3.61	6.02	4.68	0.42	1.6	5.24	7.11	3.79	5.55	3.5
CaO	9.26	8.16	8.7	8.59	5.01	5.72	8.08	15.86	7.06	4.14	7.61	10.25	4.32	0.7	5.87	5.61	8.72	6.27	5.85	5.45
Na2O	0.87	0.97	0.89	2.78	4.86	3.69	3.99	2.48	4.27	4.72	5.59	4.7	4.53	5.37	3.75	4.55	4.14	5.58	4.31	2.8
K2O	0.11	0.47	0.15	1.05	0.13	1.43	1.19	1.6	0.98	0.25	1.35	2.12	2.15	0.56	0.74	0.13	0.06	0.07	0.35	1.37
P2O5	0.23	0.26	0.27	0.41	0.32	0.019	0.19	0.37	0.11	0.15	0.09	0.15	0.13	0.03	0.18	0.15	0.1	0.21	0.14	0.11
CO2	0.05	0.55	0.15													0.1	0.3	lld	lld	0.05
H2O	5.3	6.1	6													1.7	2.2	1.3	1.9	1.9

Table 4.1 continued : Compilation of bulk rock data plotted on TAS diagrams.

Study	Mocek 2001																	
Location	Sifnos																	
Rock type	Blueschist	Blueschist	Blueschist	Blueschist	Blueschist	Eclogite	Eclogite	Eclogite	Eclogite	Eclogite	Eclogite	Eclogite	Eclogite	Eclogite	Eclogite	Eclogite	Eclogite	Eclogite
Weight %																		
SiO2	53.4	50.1	49.1	51.5	52	49.7	51.7	52.4	53.5	50.2	51.3	49.2	50.1	48.7	54.1	47.2	53.1	50.43
TiO2	1.3	1.55	1.64	1.49	1.19	1.06	1.08	1	0.78	0.94	0.88	0.91	0.7	0.9	0.62	0.93	0.67	0.75
Al2O3	14	15.6	16.4	15.6	16.4	16.5	15.3	15.6	14.9	17.4	16.2	16.8	11.8	14.5	10.2	17.6	13.6	14.98
FeOT																		
Fe2O3	3.01	4.39	7.29	6.64	4.44	2.82	2.96	3.2	3.23	4.3	3.37	2.39	4.94	4.82	5.87	2.93	3.83	7.49
FeO	10.7	8.81	5.02	5.63	7.88	6.68	4.4	3.34	3.32	6.01	4.24	6.74	6.84	7.03	10.6	5.64	4.55	2.39
MnO	0.23	0.14	0.13	0.2	0.2	0.18	0.12	0.14	0.15	0.14	0.08	0.12	0.14	0.14	0.17	0.18	0.17	0.198
MgO	5.14	4.45	3.59	3.58	4.82	6.79	6.31	4.87	5.58	2.99	5.11	3.94	5.34	4.19	3.54	4.03	5.74	4.58
CaO	4.14	8.92	10.6	9.73	8.24	8.45	7.83	9.34	9.33	9.54	8.45	7.69	13.5	13.3	9.35	9.77	9.95	7.72
Na2O	5.48	3.85	4.66	4.36	2.51	2	3.38	4.64	5.27	2.5	3.93	2.37	5	4.38	4.29	2.72	5.22	4.22
K2O	0.11	0.13	0.05	0.04	0.99	3.46	4.14	3.1	2.58	2.88	3.7	4.21	0	0.3	0	4.03	2.18	4.09
P2O5	0.12	0.13	0.11	0.15	0.38	0.28	0.67	0.67	0.33	0.93	0.8	0.96	0.83	0.99	0.22	1.23	0.26	0.93
CO2	lld	lld	lld	lld	lld	0.07	lld	lld	lld	0.2	lld	2.2	0.19	0.1	0.25	2	lld	
H2O	1.5	1.4	1.4	1.1	1.6	2.1	2	1.5	1.2	1.7	1.6	2.3	0.3	0.8	0.4	2.2	0.9	
L.O.I.																		
SUM	97.51	97.94	98.48	98.77	98.67	97.64	97.22	97.63	98.64	96.9	97.26	94.37	98.36	98.26	98.74	95.03	99.01	96.848

Table 4.1 continued: Compilation of bulk rock data plotted on TAS diagrams.

Additional wt % alkali	Orginal XRF composition	1wt % Na	2wt % Na	3wt % Na	4wt % Na	5wt % Na	1wt % K	2wt % K	3wt % K	4wt % K	5wt % K
SiO2	48.42	48.17	47.91	47.47	46.35	44.83	48.19	47.99	47.66	46.23	44.92
TiO2	1.94	1.93	1.92	1.9	1.86	1.8	1.93	1.92	1.91	1.85	1.8
Al2O3	16.12	16.04	15.95	15.8	15.43	14.92	16.04	15.98	15.87	15.39	14.95
Fe2O3	2.5	2.48	2.47	2.45	2.39	2.13	2.48	2.47	2.46	2.38	2.31
FeO	7.32	7.28	7.24	7.17	7	6.77	7.28	7.25	7.2	6.99	6.79
MnO	0.2	0.2	0.2	0.19	0.19	0.18	0.2	0.2	0.19	0.19	0.18
MgO	7.36	7.32	7.28	7.21	7.04	6.81	7.32	7.29	7.24	7.02	6.82
CaO	7.49	7.45	7.41	7.34	7.17	6.93	7.45	7.42	7.37	7.15	6.94
Na2O	4.02	4.98	6.04	6.88	7.59	8.31	4.49	4.97	5.42	5.7	6.03
K2O	0.05	0.05	0.05	0.05	0.05	0.05	0.54	1.03	1.51	1.9	2.34
H2O	4.59	4.09	3.54	2.8	2.1	1.82	4.06	3.47	2.68	2.44	2.08
CO2	0	0	0	0.73	2.83	5.28	0	0	0.49	2.74	4.83
SUM	100.01	99.99	100.01	99.99	100	99.83	99.98	99.99	100	99.98	99.99
K+Na	4.07	5.03	6.09	6.93	7.64	8.36	5.03	6	6.93	7.6	8.37
wt % gl	48.21	29.64	8.94	0	0	0	29.22	10.31	0	0	0
wt% omph	11.13	32.74	56.28	67.2	67.84	68.21	30.06	48.87	60.99	59.32	47.38

Table 4.2: Calculated bulk rock compositions and mineral abundances of glaucophane and omphacite as a function of additional wt% Na and K.

Chapter 5: CONCLUDING REMARKS

5.1 SUMMARY

This dissertation sought to better understand subduction zone processes by studying three main lines of query: 1.) What can *P-T-t* paths tell us about exhumation of high pressure terranes? 2.) How does the cycling of fluid during subduction affect the deep carbon cycle? 3.) What are the compositional controls on the dehydration and subsequent densification of subducting oceanic crust? This work integrated field work, computational thermodynamic modeling, and geochronological techniques in order to answer these questions.

In Chapter 2, I used thermodynamic modeling to explore the feasibility of decarbonation by questioning 1) at subarc conditions, how capable are externally-derived H_2O-rich fluids in driving dissolution of carbonate minerals within the altered basaltic crust of the subducting lithosphere? And 2.) Does the breakdown of serpentine at subarc conditions produce the hydrous fluids required for interacting with carbonate-bearing lithologies at the appropriate depths? To answer these questions, I calculated equilibrium mineral assemblages and fluid compositions for typical basaltic lithologies experiencing a range of subduction zone geotherms, exploring the addition of fluids at various stages. I concluded that while hotter subduction systems have *P-T* conditions that are more favorable to the dissolution of carbonate, the availability of external fluid pays an important role in balancing the global carbon budget and the depth of deserpentinization reactions strongly controls the availability of fluids for slab decarbonation.

Chapter 3 focused on garnet-bearing lithologies that preserve complex chemical zonation and are appropriate for thermodynamic modeling, $^{147}Sm/^{144}Nd$ garnet geochronology, and quartz-in-garnet geobarometry. This enabled me to not only constrain the *P-T-t* history of subducted lithologies, but to also explore the equilibrium assumptions made in conventional thermodynamic modeling and the assumptions made in inclusion-host geobarometry. Results suggested that garnet grew over a span from 45.71±0.98Ma to 41.4±1.7Ma, during initial exhumation of the Cycladic Blueschist Unit. Inferred exhumation rates are a relatively rapid, 0.4–1.7 cm/yr. Because field relationships on Syros suggest the width of the subduction channel along the slab/mantle interface is not adequate to facilitate buoyancy-driven ascension of metabasic blocks, I proposed that the initiation of southward retreat of the Hellenic Subduction Zone and subsequent slab rollback played an important role in the exhumation of subducted lithologies.

In Chapter 4, I examined the chemical differences between juxtaposed blueschist and eclogite lithologies, collected from Syros as well as from previous studies. Multiple juxtaposed samples presumably experienced identical *P-T-t* paths and we hypothesized that their apparent metamorphic differences may be controlled by minor compositional differences. Total Alkali Silica (TAS) diagrams revealed that there is a systematic chemical difference between blueschist and eclogitic; eclogites have higher alkali contents with respect to their silica contents and tend to be more oxidized. While this is still a work in progress, we tentatively suggest that chemical heterogeneities acquired during initial seafloor alteration of the basaltic protolith play an important role in the absolute *P-T* conditions of the blueschist eclogite boundary.

5.2 OUTSTANDING QUESTIONS AND FUTURE RESEARCH DIRECTIONS

The research presented in this dissertation raised new questions about subduction zone processes, the evolution of the Cycladic Blueschist Unit, and the analytical approaches used to interpret the evolution of subduction zone lithologies, a few of which are discussed here.

How can we improve the temporal and analytical precision of radiogenic isotope systems? I would like to undertake projects that seek to more generally improve the quality and precision of radiogenic isotope dating. In particular, I intend to use existing collaborations (e.g. Ethan Baxter, Boston College; Besim Dragovic, Boise State University; Mike Tappa, Boston College) to develop and improve sample preparation for TIMS analysis, including both wet chemistry separation techniques and TIMS methodology, to refine the spatial resolution and length-scales over which we can precisely measure the concentration of radiogenic isotopes in minerals, and to develop mineral separation techniques that eliminate contaminate phases and preserve sample for TIMS analysis

To what extent do kinetics influence mineral growth, metamorphic textures, and our ability to develop P-T-t paths? Observations made during the construction of *P-T* paths from Syros imply that these samples were overstepped significantly. Differences between the location of thermodynamically-predicted garnet-in reactions and the *P-T* of initial garnet growth estimated by their compositions suggest reaction overstepping of 25-50˚C, implying that these samples may have spent a sizable part of their history removed from sample-wide equilibrium. A similar phenomenon was noticed Sifnos, Greece. This neighboring island experienced a similar metamorphic history to Syros and garnets are reported to be overstepped by as much as 1GPa and

80^{o}C (Dragovic et al., 2012). A recent study (Carlson et al., 2015) explored how metamorphic petrology has been approached through equilibrium thermodynamics; the advantages, disadvantages and why considering kinetic factors is important for interpreting geological terranes. The equilibrium model for prograde metamorphism works under the assumption that rocks traveling through *P-T* space do so in a state of equilibrium. Essentially, the rate in which reactions in the rock occur is much faster that the rate of changing *P-T* conditions. Thus, kinetic barriers are insignificant. However, in natural samples, a certain degree of departure from equilibrium is required for mineral reactions to process. This begs two important questions; 1.) How far from equilibrium must rocks depart? 2.) How does this affect how we interpret metamorphic rocks? Both questions are ones that I seek to answer in future work.

What are the implications for subduction zone geodynamics if bulk rock composition contributes significantly to the location of dehydration reactions in the subducting slab? While this question is briefly touch on in chapter 4, I believe that further exploration is necessary. In addition to thinking about the implications of heterogeneous dehydration of the subducting slab on episodic tremor and megathrust ruptures (Behr et al., 2018), considering how the magnitude of dehydration is affected, and subsequent affects, densification, slab pull, buoyancy, and exhumation of high pressure terranes has important geodynamic implications. By coupling geodynamic and thermodynamic models, there is potential to predict how modern seafloor alteration of basaltic crust will influence the nature of subduction in the future. Conversely, it could be possible to use what we currently know about the geodynamics of modern subduction systems and calculated alteration conditions of the ancient seafloor.

APPENDIX A: SUPPLEMENTARY INFORMATION FOR CHAPTER 3

A1: TABLES

	Sample	$^{147}Sm/^{143}Nd$	2σ std error	$^{143}Nd/^{144}Nd$	2σ std error	ppm Sm	ppm Nd
14HSY-35E	core A	0.417634	0.000154	0.512631	0.000009	1.352120	1.958399
	core B	0.723480	0.000183	0.512732	0.000012	0.914019	0.764206
	rim 120HF	0.575086	0.000301	0.512589	0.000045	0.202623	0.213126
	Rim A	0.046380	0.000038	0.512538	0.000008	0.525526	6.854041
	whole rock AQ2	0.104451	0.000012	0.512539	0.000006	1.972263	11.421776
	matrix AQ2	0.101562	0.000017	0.512543	0.000006	2.835282	16.886843
	gt core pdr	0.150305	0.000570	0.512564	0.000006	2.567788	10.333997
	gt Rim B	0.871635	0.000102	0.512755	0.000008	0.291728	0.202453
	gt rim pdr clean	0.632232	0.002678	0.512708	0.000041	0.297018	0.284176
	gt rim pdr dirty	0.120948	0.000023	0.512551	0.000027	1.631544	8.159821
	1 core gt pdr	1.775309	0.008029	0.513036	0.000028	0.740704	0.252379
	2 core gt pdr	1.940317	0.008773	0.513093	0.000014	0.732559	0.228377
	3 core gt pdr	2.013777	0.000333	0.513122	0.000026	0.645634	0.193935
14BSY-3A	gt pdr clean	0.340687	0.000414	0.512280	0.000009	4.738630	8.413551
	gt pdr clean tripoli	0.340883	0.000414	0.512288	0.000009	4.739591	8.410423
	whole rock	0.191532	0.000073	0.512229	0.000009	58.928598	186.108919
	gt 1	0.277296	0.000234	0.512259	0.000005	4.303744	9.388255
	gt 2	0.271004	0.000213	0.512266	0.000006	4.647209	10.372868
14BSY-3F	gt 120 HF	0.788263	0.001344	0.512439	0.000083	0.072558	0.055680
	gt pdr clean	0.123221	0.000088	0.512297	0.000009	0.813102	3.991559
	matrix	0.136423	0.001649	0.512262	0.000035	0.993668	4.405915
	whole rock Aq1	0.132892	0.000070	0.512294	0.000009	0.309926	1.410725
	gt	0.254709	0.000088	0.512317	0.000010	0.079767	0.189435
14CSY-20A	bs gt	0.167940	0.000024	0.512988	0.000006	0.170648	0.614652
	law gt	0.171201	0.000020	0.512991	0.000006	0.157392	0.556109
	bs gt pdr clean	0.167646	0.000131	0.512971	0.000012	0.477480	1.722835
	law gt pdr clean	0.176607	0.000112	0.512992	0.000005	0.082571	0.282815
	bs gt pdr dirty	0.158794	0.000020	0.512941	0.000010	0.654421	2.492905
	law gt pdr dirty	0.164091	0.000035	0.512907	0.000010	3.205274	11.815746
	whole rock	0.166058	0.000277	0.512968	0.000007	37.184988	135.453295

Table A1: Additional isotopic values from Sm/Nd garnet geochronology.

APPENDIX B: SUPPLEMENTARY INFORMATION FOR CHAPTER 4

B1: *P-T* Phase diagrams

The composition of garnet porphyroblasts is used to determine the peak *P-T* conditions of metamorphism for sample 14CSY-20A. Calculated isopleths for the almandine, grossular, pyrope, and spessartine content of measured garnet compositions intersect in *P-T* space, assuming the garnet crystal is in equilibrium with the bulk rock composition at its core and the bulk rock matrix at its rim (Figure A1). A detailed discussion regarding garnet-bulk rock equilibrium assumptions can be found in chapter 3. Garnet compositions were acquired via microprobe analysis using a Camera SX-50 microprobe with the beam set at 20nA and an acceleration voltage of 15kV and representative analyses can be found in table A1.

Garnet in sample 14CSY-20A began to grow at approximately 1.9GPa and 485˚C and reach peak metamorphic conditions at approximately 2.2GPa and 525˚C (Figure A1). These values are similar to garnet growth *P-T* conditions calculated in chapter 3, and are also in agreement with other studies done in high pressure terranes on Syros, Greece (e.g. Trotet et al., 2001). Furthermore, peak *P-T* conditions coincide with the blueschist/eclogite boundary, and overlap *P-T* values calculated for eclogites on Syros (Jamie Kendall thesis). The predicted mineral assemblage at the beginning of garnet growth is dominated by amphibole and lawsonite, with the addition of chlorite, carbonate, and rutile. We propose that the abundant epidote inclusions in garnet were once lawsonite that have since broken down upon additional heating or during exhumation. The rims of garnet are predicted to be in equilibrium with a matrix assemblage of amphibole, lawsonite, pyroxene, rutile, and chlorite. This is generally in agreement with thin section observations, with the exception of lawsonite, which has been psuedomorphically replaced by epidote and white mica post peak metamorphism.

B2. FIGURES

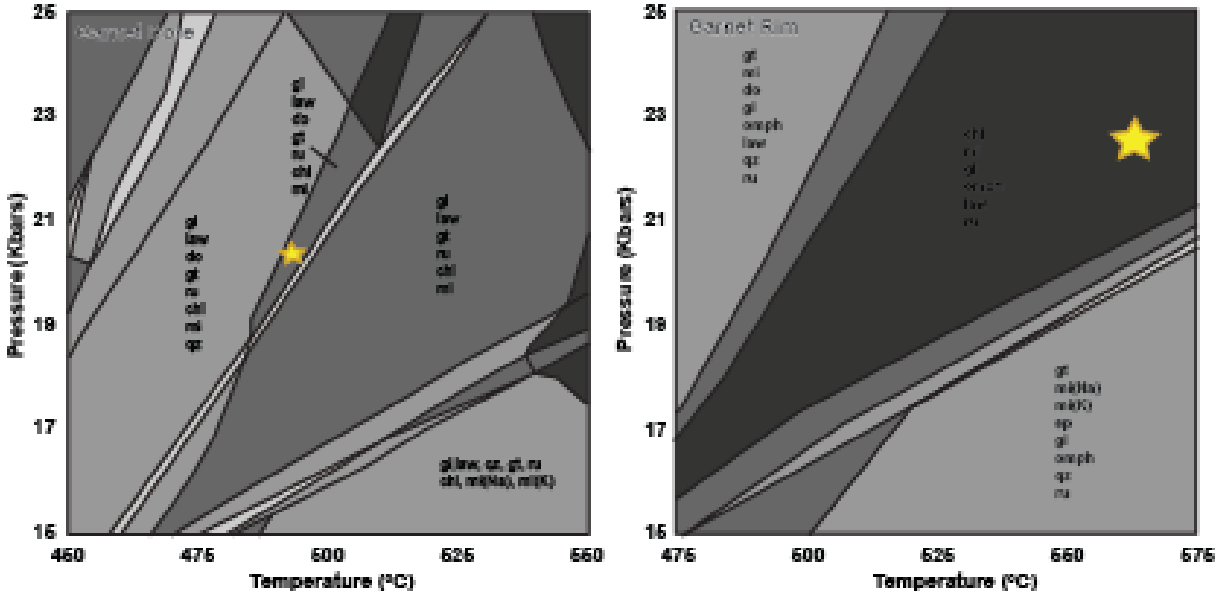

Figure B1: Isochemical phase diagrams used to calculate *P-T* conditions of the beginning of garnet growth (left), and the end of garnet growth (right).

B3: TABLES

	SiO2	TiO2	Al2O3	MgO	CaO	MnO	FeO	Na2O	K2O	Volume %
Garnet	37.93	0.15	21.51	2.50	9.56	2.12	26.22	0.02	0.00	7
Glaucophane	60.13	0.03	12.27	10.80	0.78	0.02	8.98	6.97	0.02	65
Epidote	39.64	0.16	28.32	0.00	23.82	0.20	7.85	0.01	0.00	15
Titanite	30.70	38.63	1.72	0.00	28.65	0.01	0.25	0.03	0.00	3
Plagioclase	49.93	0.09	41.00	0.34	0.17	0.00	0.25	6.89	1.32	2
Rutile	0.02	98.69	0.00	0.02	0.28	0.05	0.90	0.04	0.00	3
Oxides	1.52	0.00	0.16	0.02	0.21	0.12	97.96	0.00	0.01	1
Mica	53.23	0.27	29.49	3.24	0.01	0.02	2.66	0.58	10.51	1

Table B1: Representative electron microprobe analyses of minerals found in 14CSY-20A.

Garnet Cores				Garnet Rims			
Fe	Mn	Mg	Ca	Fe	Mn	Mg	Ca
0.554	0.088	0.088	0.269	0.595	0.013	0.104	0.288
0.561	0.087	0.094	0.257	0.599	0.017	0.103	0.280
0.536	0.101	0.083	0.280	0.597	0.021	0.105	0.277
0.536	0.106	0.081	0.278	0.598	0.039	0.100	0.263
0.570	0.107	0.085	0.238	0.598	0.016	0.108	0.278

Table B2: Representative mole fraction of major cations found in garnet measured in the core garnet rim.